**CREEP AND OXIDATION OF HAFNIUM DIBORIDE-BASED
ULTRA HIGH TEMPERATURE CERAMICS AT 1500°C**

DISSERTATION

Anthony DeGregoria, Lieutenant Colonel, USAF
AFIT-ENY-DS-15-D-040

**DEPARTMENT OF THE AIR FORCE
AIR UNIVERSITY**

AIR FORCE INSTITUTE OF TECHNOLOGY

Wright-Patterson Air Force Base, Ohio

CREEP AND OXIDATION OF HAFNIUM DIBORIDE-BASED
ULTRA HIGH TEMPERATURE CERAMICS AT 1500°C

DISSERTATION

Presented to the Faculty

Department of Aeronautics and Astronautics

Graduate School of Engineering and Management

Air Force Institute of Technology

Air University

Air Education and Training Command

In Partial Fulfillment of the Requirements for the

Degree of Doctor of Philosophy

Anthony DeGregoria, MS

Lieutenant Colonel, USAF

December 2015

AFIT-ENY-DS-15-D-040

CREEP AND OXIDATION OF HAFNIUM DIBORIDE-BASED
ULTRA HIGH TEMPERATURE CERAMICS AT 1500˚C

Anthony DeGregoria, MS
Lieutenant Colonel, USAF

Committee Membership:

Marina B. Ruggles-Wrenn, PhD
Chairman

Randall S. Hay, PhD
Member

Robert L. Hengehold, PhD
Member

Maj Ryan P. O'Hara, PhD
Member

Triplicane A. Parthasarathy, PhD
Member

ADEDJI B. BADIRU, PhD
Dean, Graduate School of Engineering and Management

AFIT-ENY-DS-15-D-040

Abstract

Ultra high temperature ceramics (UHTCs) are leading candidates for aerospace structural applications in high temperature environments, including the leading edges of hypersonic aircraft and thermal protection systems for atmospheric re-entry vehicles. Before UHTCs can be used in such applications, their structural integrity and environmental durability must be assured, which requires a thorough understanding and characterization of their creep and oxidation behavior at relevant service temperatures.

Creep, or the progressive, time-dependent deformation of material under constant load, is a critical criterion in these applications, but not much is known with regard to UHTCs or whether there are interactions with oxidation processes. Thus, a facility for high temperature, mechanical testing in air was augmented for testing in argon. Then, the compressive creep of a popular UHTC, HfB_2, was examined at 1500°C in argon and compared to results in air. HfB_2 specimens with 0, 10, 20, and 30% additions of SiC were tested, which enabled assessments of the effects of grain size and SiC content on creep behavior. Boundary mechanisms accommodated by diffusion through grains dominated the creep rates. The results also suggest that SiC formed a network of point-to-point contacts and increased creep resistance.

A unique stressed oxidation test was devised in order to further investigate the interaction of creep and oxidation. The results indicate that up to 75 MPa of compressive stress, models of creep and oxidation in HfB_2-based UHTCs can be decoupled.

Acknowledgments

Throughout this research, I too have been amazed by God's great design. It's not often in life that we are given the time to stare into a blazing furnace for days at a time… or look at micrographs of burnt ceramics for weeks on end…or spend years pondering what's going on inside one material, at one temperature, while being squashed by an artificial force of man. Honestly, I've gotten lost in it all on more than one occasion… fishing for that next big pearl of wisdom. And yet every time I sang "Where can I run from Your love?" and offered a few pitiful seconds to recognize the wonders of Your creation, You were there, and gave a glimmer of hope for salvation. The truth is You knitted me in my mother's womb. You followed me every morning when I drove off to work. You stayed with me no matter how deep I dove into a lab. You walked with me at night when I went home lost and confused. Thank You, Thank You, Thank You, God, for everything! P.S. For Christmas, I'd really love an XB-70 made of HfB_2-20% SiC.

Dr. Ruggles-Wrenn, I cannot thank you enough for years of professional teaching, mentoring, and guidance. You have truly given me a new capacity for understanding and connecting the experimental and theoretical, and you even worked out some bad habits from my elementary years! To my committee, thank you for your encouragement to put forward research consistent with the needs and expectations of our institution. Many others deserve thanks, throughout AFIT and AFRL, but I'd be remiss not to mention the most influential. Thank you to AFOSR for funding and RX for supporting this research. Specifically, thank you Sheena, Kathleen, Jared, Carmen, Donna, Randy, Bryan, Tom, and Bob. Without your support, this would have been unbearable. Thank you AFIT Fab Shop, especially Dan, and Lab Techs. Without your craftsmanship, this paper would be hollow. Together, all of you make the mission happen and keep our Constitution safe!

In closing, I would like to express my most viscous thanks to my wife and kids. You're my beach and, without you, there'd be no sunshine!

Table of Contents

List of Figures

List of Tables

CREEP AND OXIDATION OF HAFNIUM DIBORIDE-BASED ULTRA HIGH TEMPERATURE CERAMICS AT 1500˚C

I. Introduction

1.1 Problem Statement

Aerospace engineers continue to encounter problems with the application of structural material systems in high temperature, oxidizing environments. For example, structural materials designed to withstand high speed flows through the atmosphere often limit the achievement of sustained hypersonic flight. Also, structural materials for use in the flows of hot engine sections often limit advancements in the power and efficiency of propulsion systems. These two examples embody a whole host of more specific problems that prevent aerospace customers from going farther, faster, and more efficiently. They include structural material systems reaching their limits, melting, reacting, ablating, and deforming. They include aircraft incapable of maintaining the structural integrity of leading edges, thermal protection systems, turbine blades, and engine nozzles. They include customers unable to achieve and sustain improvements in performance and, in some cases, unable to perform entire mission sets.

How Important are These Problems? Contemporary strategists of national defense assign great importance to the pursuit of solutions to these types of problems. The National Defense Authorization Act of 2007 amended the United States Code to establish a Joint Technology Office for Hypersonics, which provides roadmaps and oversight for research and development. The roadmap for basic research calls out six technical areas, one of which is high-temperature materials and structures for the

1

hypersonic environment, and connects these technical areas to the core of the Department of Defense's efforts to deliver hypersonic capabilities for national security [1]. In 2012, the Deputy Assistance Secretary of the Air Force for Science, Technology, and Engineering, Dr. Steven H. Walker, cited high speed and energy efficient platforms as key game changing investments for the Air Force's Science and Technology Strategy [2]. Also, in its issue paper on *Hypersonic Technology and Development: Imperatives Critical to U.S. National Security and Aerospace Superiority,* the Aerospace Industries Association identified materials as one of the critical areas with tough problems to solve [3]. More specifically, the National Hypersonic Science Center, supported by the Air Force Research Laboratory and the National Aeronautics and Space Administration, identifies the discovery and characterization of oxidation-resistant materials at and above 1500˚C as one of its three goals in materials and structures [4]. These sources represent a small, yet convincing, sample of leaders in national defense and the importance that they place in solving problems associated with structural materials for high temperature, oxidizing environments.

How Challenging are These Problems? The problem of finding structural material systems suitable for high temperature, oxidizing environments has challenged professional aerospace engineers for many decades and remains a real problem for even the most advanced designs of today's Air Force. In the 1960's, the X-15 required ablative

Figure 1: X-15 [Photo Courtesy of NASA]

coatings to protect its primary structures at high speeds. Even then, the aircraft suffered such extensive damage after less than 3 minutes of flight, including a brief time at Mach 6.7, that a project engineer commented, "If there had been any question that the airplane was going to come back in that shape, we never would have flown it." [5]   In the 1990's, the National Research Council published an evaluation of the Hypersonic Technology Program, which described the program as insufficient, "because the development of critical enabling technologies for hypersonic air-breathing missiles are not included in the program." Among the five most critical enabling technologies, the committee identified airframe and engine thermostructural systems as the highest priority. Specifically, the report described the lack of an oxidation-resistant material that can survive the very high temperatures associated with an operational air-breathing hypersonic vehicle. In this case, the report considered Mach numbers 4, 6, and 8, including stagnation temperatures of 1100, 2500, and 4200˚F and engine temperatures of 4000, 4400, and 5100˚F, respectively [6]. In 2011, the Defense Advanced Research Projects Agency concluded its decade-long, prompt global strike program with a failed flight test of HTV-2. The failure was attributed to degradation of the structure in a severe aero-thermal environment.

Figure 2: HTV-2 [Image Courtesy of DARPA]

The lessons learned focus on improving the design of load-bearing thermal structures, including their heating, properties, uncertainties, variables, modeling, thermal stresses, and responses. The program manager identified the high-temperature, load-bearing aeroshell as one of the areas of greatest technical risk [7]. Thus, the history of high speed programs in the Air Force demonstrates the need for better structural material systems capable of operating in extreme environments.

Will We See These Problems in the Future? The Air Force's long-term hypersonic plan virtually assures that aerospace engineers will continue to encounter these problems in the future. Plans already include a high speed strike weapon and a hypersonic intelligence, surveillance and reconnaissance (ISR) and strike aircraft. One concept, the SR-72, hopes to cruise at Mach 6 [8]. Additionally, the drive to improve the performance and efficiency of propulsion systems will surely continue to demand better structural material systems that can perform in extreme environments. Not only does this include propulsion systems for hypersonic aircraft, but also propulsion systems in the space and general aviation industries. Undoubtedly, the aerospace industry will continue to challenge structural material systems with high speed flows through the atmosphere and hotter flows inside engines. This makes structural material systems for high temperature, oxidizing environments a research topic worthy of serious consideration.

1.2 Research Focus

Although there are many approaches to solving these problems, recent developments with ultra high temperature ceramics (UHTCs) present new and exciting opportunities that researchers are just beginning to explore. For decades, researchers have suspected that, one day, UHTCs might become the material of choice for structural applications in extreme environments. Unfortunately, no one seemed able to produce UHTCs that could live up to the hopes. Recently, however, developments in material processing and a growing body of knowledge in material systems design sparked a renewed interest in the design, processing, and behavior of UHTCs. The *Literature Review*, which starts on page 12, shows that a lot of recent progress focuses on transition metal diborides, including hafnium diboride (HfB_2) and zirconium diboride (ZrB_2). These materials provide impressive strength, chemical stability, and thermal and electrical conductivities at high temperatures, including resistances to erosion and thermal stress [9]. Silicon carbide (SiC), a popular additive, improves oxidation resistance and densification. Thanks to these recent developments, the potential for UHTCs to perform at high temperatures in oxidizing environments is becoming a reality.

Despite these recent developments, aerospace engineers still need to gain an understanding of the structural performance of UHTCs. The *Literature Review* shows that researchers have been hard at work, improving the processing, densification, and oxidation resistance of UHTCs. However, very little is known about their creep behavior and its relationship with oxidation, which are two important considerations for aerospace structural design applications in high temperature, oxidizing environments. Creep can be simply described as the progressive, time-dependent deformation of material under

5

constant load, with a more thorough description in Section 2.2. Before UHTCs can be used to solve problems like those described in Section 1.1, a thorough understanding of creep and oxidation is required, because these properties could directly affect the safety and operational limits of future aerospace vehicles. Presently, this level of understanding does not exist. Theories have been proposed, models have been developed, and sparse results have been obtained, but nothing brings all of the primary factors together and reliably describes the creep of UHTCs at high temperatures in an oxidizing environment.

Important questions about the creep and oxidation of UHTCs remain unanswered. *What are the creep rates and creep mechanisms associated with a particular UHTC?* Creep tests at various stress levels in an inert environment, along with microstructural investigations, can answer these questions. *How do additives affect creep?* Examining the creep of UHTCs with various additives in an inert environment can elucidate the effects of additives. *Are creep and oxidation independent processes? Does oxidation change creep behavior?* Comparing and contrasting creep results in oxidizing and inert environments can provide insight. Alternatively, *does stress affect oxidation behavior?*

This research focuses on answering these questions and developing a thorough understanding of the creep and oxidation of UHTCs, including the identification of underlying creep mechanisms. Thus, the creep of UHTCs must be examined at the temperature of interest in an inert environment, free from the effects of oxidation. Experimental results in an inert environment could provide a solid foundation for improving material system designs and developing models that can predict creep rates and lifetimes. Once creep in an inert environment is understood, creep in an oxidizing environment can be properly examined and understood. If we can determine whether

stress affects oxidation behavior, for example, by changing pore sizes and the diffusion of oxygen, then we can fully understand whether creep and oxidation are interactive processes. If the processes are found to be independent, a creep model based on experimental results obtained in an inert environment, combined with an oxidation kinetics model, may reliably predict the creep behavior of UHTCs in an oxidizing environment. If the processes are found to be dependent, this research will provide an experimental foundation for the development of a coupled creep-oxidation model. Either outcome would effectively answer the research questions.

Table 1 summarizes the only experiments on the high temperature creep behavior of HfB_2- and ZrB_2-based UHTCs found in the literature. Both material systems are included, because of their similarity, which is further discussed in Section 2.1.

Table 1: Summary of High Temperature Creep Experiments on HfB_2 and ZrB_2

Lead Author	Year	Material	Mechanical Method	Thermal Method	Inert	Oxidizing	Temperatures (°C)	Stresses (MPa)	Additives
Winder	2015	HfB_2	Uniaxial Compression	Furnace	No	Yes	1500	25 to 100	0 and 20% SiC
Gangireddy	2013	ZrB_2	Flexural	Resistance	Yes	Yes	1700 to 2200	20 to 50	30% SiC
Bird	2013	ZrB_2	Flexural	Furnace	Yes	No	1400 to 1820	16 to 97	20% SiC
Guo	2011	ZrB_2	Flexural	Furnace	Yes	No	1500 to 1600	19	30% SiC
Talmy	2008	ZrB_2	Flexural	Furnace	No	Yes	1200 to 1500	30 to 180	0 to 50% SiC
Meléndez-Martínez	2001	ZrB_2	Uniaxial Compression	Furnace	Yes	No	1400 to 1600	47 to 472	0 and 4% Ni
Kats	1981	ZrB_2	Flexural	Furnace	Yes	No	1700 to 2420	5 to 30	0 to 100% ZrC
Spivak	1973	ZrB_2	Flexural	Unknown	Yes	No	2052 to 2291	5 to 196	0 to 100% ZrN
Rhodes	1970	Both	Both	Furnace	Yes	No	800 to 1800	172	0 and 20% SiC

Most of the previous efforts employ flexural setups for mechanical testing, for example, Guo [10], Kats [11], and Spivak [12]. These methods add some assumptions and special considerations when extending the results to other types of loading and make the

determination of the underlying creep mechanisms more difficult. This is because flexural tests bend the materials to test creep resistance, which puts one side of the material in tension and the other in compression. This effectively combines possibly different creep behaviors into one set of results for tension and compression, which have been shown many times in other materials to be different. Additionally, it is widely recognized that strain measurements are challenging above 1400°C, and accurate strains are vital for understanding creep. However, with the exception of Winder [13] and Meléndez-Martínez et al.[14], all of the references in Table 1 use varying methods to measure displacement at the midpoint of a flexural setup and assume various perspectives of elementary beam theory to determine strain. This research seeks to use a method of direct strain measurements, which avoids some of these assumptions, and examine creep in pure compression. This provides a clearer understanding of creep mechanisms, and focusing on compressive creep behavior is important for some of the aerospace structural applications discussed in Section 1.1.

Gangireddy et al. [15] present results from creep experiments in both an inert and oxidizing environment, but use a novel test method and only consider ZrB_2 with 30% SiC by volume. The mechanical method uses an Electro Magnetic Mechanical Apparatus, known as EMMA, to apply loading via the Lorentz force. The creep tests typically last 20 to 300 seconds, which are shown to provide useful information, but arguably might not provide the steady state creep information that is typically desired in an analysis of creep mechanisms. This research aims to test for longer durations, sufficient to assess steady state creep, using an objective methodology described in Appendix F. Results obtained by Bird et al. [16] and Talmy et al.[17] offer the potential for a comparison

between creep in inert and oxidizing environments, but these comparisons would be limited to ZrB_2 with 20% SiC by volume. Working through differences in experiments would make comparisons between their results unclear. Overall, varying methodologies, assumptions, and sometimes unspecified parameters, found among all of the works presented in Table 1, make comparisons difficult and any broader conclusions suspect.

Winder's work [13] at the Air Force Institute of Technology offers results pertaining to the creep of HfB_2 at 1500°C in air. However, there are no comparable results available on the creep behavior of this material in an inert environment, not confounded with the effects of oxidation. The investigation by Rhodes et al. [18] was cursory and, arguably, conducted with a historic material that might not represent the behavior of present day materials. Thus, no work provides a clean foundation for the creep behavior of HfB_2 or the effects of SiC additives in an inert environment. With the facility and material sources used in the experiments by Winder still available, focusing this research on the compressive creep of HfB_2 in an inert environment presents a unique opportunity to thoroughly understand and characterize the creep behavior of HfB_2 as well as the interactions of the creep and oxidation processes. Since building off of Winder's work provides clear benefits, including a proven experimental setup and some creep results in air, Section 1.3 will present research objectives in a way that maintains as much similarity as possible to Winder's work. Thus, by focusing on similar materials, mechanical methods, and temperature, but in an inert environment, important new information will add to our understanding of the creep and oxidation behavior of UHTCs, while maintaining the advantage of being able to make direct comparisons to Winder's results in air.

1.3 Research Objectives

The objectives of this research align with the Air Force Institute of Technology's mission to "Advance air, space, and cyberspace power for the Nation, its partners, and our armed forces by providing relevant defense-focused technical graduate and continuing education, research, and consultation." Specifically, the following research objectives seek to answer the questions posed in the *Research Focus*, which directly contribute to advancing air and space power by helping to address the issues discussed in the *Problem Statement*.

Consistent with the *Research Focus*, the research objectives target the creep and oxidation of HfB_2 at $1500°C$. Experimentation includes compressive creep tests in an inert environment and stressed oxidation tests in air. Both pure HfB_2 and HfB_2 with additives of 10, 20, and 30% SiC by volume will be considered. Modifications to the experimental facility and procedures will be made to permit mechanical testing in an inert environment. Please refer to the *Methodology* section for specific information. The following list summarizes the research objectives.

1. Design, setup, and demonstrate an experimental facility for performing compressive creep tests at $1500°C$ in argon
   a. Modify the existing facility and procedures to permit testing in argon
   b. Calibrate the equipment and instrumentation
   c. Perform tests to verify and validate the experimental setup

2. Investigate the creep behavior of hafnium diboride-based UHTCs at 1500°C

    a. Examine the compressive creep behavior of hafnium diboride-based UHTCs at different stress levels at 1500°C in argon

    b. Examine the effect of SiC additives on the compressive creep behavior of hafnium diboride-based UHTCs at 1500°C in argon

    c. Examine the effect of grain size on the compressive creep behavior of hafnium diboride-based UHTCs at 1500°C in argon

    d. Identify creep mechanisms and characterize post-test microstructures

3. Investigate the interaction of creep and oxidation processes in hafnium diboride-based UHTCs at 1500°C

    a. Examine the effect of oxidation on the compressive creep behavior of hafnium diboride-based UHTCs by comparing results at 1500°C in argon and air

    b. Examine the effect of compressive stress on the oxidation behavior of hafnium diboride-based UHTCs at 1500°C in air

II. Literature Review

2.1 Ultra High Temperature Ceramics

Ceramics: Ceramics include a large number and diversity of materials. The word *ceramic* comes from the Greek word *keramos*, meaning pottery, but now refers to many classes of materials, including clays, abrasives, refractories, glasses, cements, and engineering ceramics. Thus, it is not surprising that ceramic materials encompass many useful properties and serve many types of applications, including mechanical, thermal, nuclear, optical, electrical, magnetic, biological, and chemical. Ceramics are also grouped by chemical composition, some of which include borides, carbides, nitrides, and oxides [19]. Davidge points out that the atomic bonding in ceramics can be ionic or covalent, but typically a hybrid, with larger differences in electronegativity driving more ionic behavior [20]. This large number and diversity of materials also makes ceramics difficult to define.

Academics struggle to find a precise and universal definition for ceramics, even though it is generally recognized that humans have been working with ceramics for thousands of years. One of the most widely accepted definitions simply describes ceramics as non-metallic, inorganic solids [21], [22]. Others give more precise definitions like "any of various hard, brittle, heat- and corrosion-resistant materials made by firing clay or other minerals and consisting of one or more metals in combination with one or more nonmetals, usually including oxygen" [19]. While this definition includes property, processing, and compositional components, some simply define ceramics in terms of general properties. A cursory review of the literature confirms Davidge's

observation, "There is no completely satisfactory and universally accepted definition of ceramics." [20]

In terms of mechanical properties, ceramics primarily distinguish themselves from other materials by their brittleness. Cannon and Langdon highlight susceptibility to thermal shock, along with brittleness, as the historical disadvantages of ceramics in structural applications [23]. Compared to metals, ceramics contain fewer free electrons, so they generally have lower electrical conductivities at room temperature [24]. Ashby adds that ceramics feature corrosion resistance, high stiffness, high hardness, and high temperature strength [21]. For the aerospace and other industries, high temperature strength stands out as a very useful property. In fact, this property is so useful that such materials are distinctively referred to as refractory. Groups of refractory ceramics include borides, carbides, nitrides, and oxides [24].

Ultra High Temperature Ceramics: When the melting temperature of a ceramic exceeds 3000˚C, it might also have the privilege of being referred to as an ultra high temperature ceramic (UHTC). Sometimes UHTCs are identified by an ability to continuously operate above 1600˚C [25]. Ideally, for high temperature, structural applications, a material would be highly refractory and have a high melting temperature. From this perspective of performance, Figure 3 presents some of the most refractory materials with high melting temperatures, divided into five classes. The borides, carbides, and nitrides with melting temperatures above 3000˚C are generally recognized as UHTCs [9].
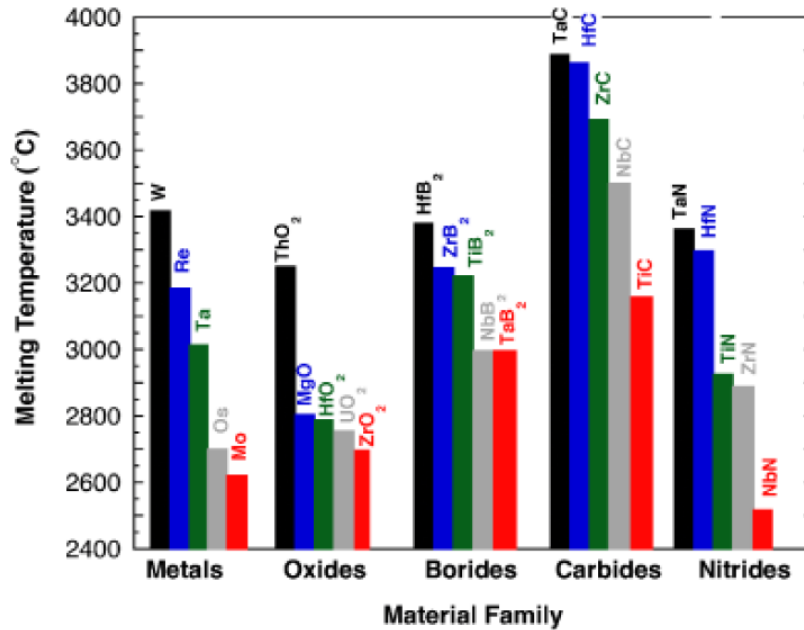
Figure 3: Melting Points of Some Refractory Metals & Ceramics
Copyright © 2007, John Wiley and Sons,
Journal of the American Ceramic Society, Used with Permission [9]

Among the refractory UHTCs, even fewer materials perform well in an oxidizing environment. Carbides generally have poor oxidization resistance and require protection at high temperatures. Specifically, for hafnium and zirconium carbides, Parthasarathy et al. note that the partial pressure of carbon monoxide makes the oxide scale porous and non-protective above 1730°C [26]. Similar phenomena occur for hafnium and zirconium nitrides in high temperature, oxidizing environments, where bubbles disrupt the protective abilities of the oxide scales [27]. Fortunately, some of the UHTC transition metal diborides seem to do a better job of retaining their oxidation resistance at higher temperatures.

Transition Metal Diborides: The advantages of transition metal diborides include high temperature strength and good oxidation resistance. Thus, the diborides with melting temperatures above 3000˚C might easily be described as refractory UHTCs with good oxidation resistance. Their crystal structure is hexagonal close packed, and they also exhibit high modulus, high hardness, and good electrical conductivity [28]. However, they also exhibit difficult sinterability, poor toughness, and low thermal stability in high temperature, oxidizing environments [29].

In a study of five transition metal diborides (i.e. TiB_2, ZrB_2, HfB_2, NbB_2, and TaB_2), Kaufman and Clougherty identified HfB_2 and ZrB_2 as the most oxidation resistant for high temperature applications and suggested that SiC additives might further improve oxidation resistance [30]. When diborides oxidize, B_2O_3 forms, but generally does not disrupt the oxide scales [26] and even provides some additional protection from oxidation. Unfortunately, the oxidation resistance of these materials, at least in a pure condition, is still not sufficient for the applications described in the *Problem Statement*. However, additives, such as SiC and $MoSi_2$, show great promise for improving oxidation resistance and sinterability, so a later section of this literature review is dedicated to additives.

The sinterability of transition metal diborides has proven difficult, so many fabrication methods have been, and continue to be, employed. In order to improve material performance, typical goals in the fabrication processes include reduced porosity, increased density, decreased impurities, smaller grain sizes, stronger grain boundaries, uniform distribution of additives, and all sorts of other factors, not to mention typical material performance factors like strength, toughness, machinability, and cost. Some of

15

the methods presented in the literature include hot pressing, reactive hot pressing, pressureless sintering, reactive and non-reactive spark plasma sintering, induction zone melting, plasma enhanced chemical vapor deposition, reactive ion plating, self-propagating high-temperature synthesis, sol-gel synthesis, and reactions between hafnium and boride-containing compounds [9], [31]–[39]. With so many materials and fabrication methods available, with great effects on material performance, serious consideration should be given to the selection of a specific material and fabrication process for research into the creep behavior of UHTCs. The following section briefly reviews *Hafnium Diboride* and spark plasma sintering, the material and fabrication method selected for this research effort.

Hafnium Diboride: As previously described, HfB_2 and ZrB_2 have been historically identified as the UHTCs with the most potential for application in high temperature, oxidizing environments. It is no coincidence that these two UHTCs are often mentioned in the same context, because hafnium and zirconium have very similar chemical properties. In fact, hafnium and zirconium are so similar that they are almost always found together in nature, although hafnium is less abundant and thus more expensive. They share the same group and ground state level on the periodic table of elements and, despite being in different periods, they share very similar atomic radii, thanks to the effects of lanthanide contraction on hafnium. This effect gives them an almost identical ionic radius. However, since hafnium has more atomic mass in a similar volume, it is much denser [40], and the theoretical density of HfB_2 is much higher than ZrB_2, 11.212 versus 6.119 g/cm^3 [9]. While higher densities are an inherent detractor for

16

weight-conscious aerospace applications, other factors demand consideration in high temperature, oxidizing environments. HfB_2 has a higher melting temperature than ZrB_2 (i.e. 3380 versus 3245˚C [25]), and HfB_2's first and second ionization energies are slightly higher 7.0 and 14.9 eV versus 6.8 and 13.1 eV, respectively [40]. Also, HfO_2 has a higher melting temperature than ZrO_2, 2800 versus 2700˚C [41]. Most importantly, experience has shown that HfB_2-based material systems are more oxidation resistant than ZrB_2 [42]–[44].

Spark plasma sintering has been successfully utilized to produce HfB_2-based materials with nearly full densities and low porosities [42], [45]–[48]. This method simultaneously compresses and heats powders in order to achieve densification. Direct or pulsed electric current quickly heats the powders, which shortens the duration of the process and minimizes grain growth, compared with other fabrication methods. Additionally, it is suspected that the electrical discharges reduce oxide impurities and improve high temperature strength [9]. When synthesis and densification of the powders occur in a single step, it is referred to as reactive spark plasma sintering. However, if the powders are synthesized via a different method, such as self-propagating high-temperature synthesis, then spark plasma sintering is only used for densification. Orru and Cao concluded that reactive spark plasma sintering was more effective for pure materials, while self-propagating high-temperature synthesis, followed by spark plasma sintering, was more effective for binary material systems [47]. Overall, spark plasma sintering has been shown to require lower heating, shorter times, and fewer additives, compared to hot pressing, thus yielding denser and stronger materials [45].

17

Table 2 presents some commonly useful properties of HfB_2.

Table 2: Some Common Properties of HfB_2

Property	Value	Units	Reference
Crystal System	Hexagonal		[49]
Structural Type	AlB_2		[49]
a (Unit Cell Parameter)	3.139	Å	[50]
c (Unit Cell Parameter)	3.473	Å	[50]
Theoretical Density	11.12	g/cm^3	[51]
Poisson's Ratio	0.12		[52]
Young's Modulus	480	GPa	[53]
Bulk Modulus	212	GPa	[9]
Hardness	28	GPa	[49]
Fracture Toughness	4.0	MPa√m	[36]
Brittle to Ductile Transition Temperature	1100	˚C	[54]
Melting Temperature	3380	˚C	[55]
Heat Capacity (Room Temperature)	49.5	J/(K mol)	[56]
Coefficient of Thermal Expansion	6.30E-06	K^{-1}	[49]
Thermal Conductivity (Room Temperature)	100	W/(K m)	[57]
Electrical Conductivity (Room Temperature)	9.10E+06	S/m	[49]

Strength especially depends on factors like density, grain size, and additives [48], which reemphasizes some of the benefits of spark plasma sintering. Zapata-Solvas demonstrated that SiC and $MoSi_2$ additives can increase flexural strength [48]. Rezaie et al. also showed that the critical flaw size of a UHTC closely relates to the additive's grain size. This highlights the effect of mismatches in the thermal expansion coefficients of the parent and additive materials, as evidenced by microcracks at the interface [58].

Monteverde showed that electrical discharge machining reduced flexural strength about

26% compared to diamond cutting, oxidized some of the surface material, and left traces

of copper and zinc from the machining process [59]. Alternatively, Ramirez-Rico

showed that polishing can improve the compressive strength of UHTCs, although the

difference decreased at higher temperatures as the effects of oxidation became more

dominant [60]. As expected, HfB_2's strength decreases as temperature increases, but

takes a sharper drop past 1100˚C, where plastic deformation before failure becomes

apparent. Surprisingly, HfB_2's thermal conductivity decreases as temperature increases,

leveling off around 70 W/(K m) by 800˚C [54]. However, Gasch shows that there are

large differences in thermal conductivities depending on grain size and processing [57].

Although some good, yet limited, information has been recently published in the

literature about the common properties of UHTCs, even less is known about their creep

behavior. Thus, it is important to review some of the basic concepts of creep and what

little is known with regards to UHTCs.

2.2 Creep Behavior

Concepts: Creep generally refers to the time-dependent strain that occurs in a stressed material. In practical terms, it's the continual deformation of a material, even though it might be under a constant load and temperature. Observation of creep often occurs over long periods of time and can include both viscoelastic and viscoplastic behaviors. Figure 4 depicts a typical creep curve, divided into three distinct regions: primary, secondary, and tertiary creep. These three regions can be distinguished by their respective strain rates: decreasing, constant, and increasing. Creep is important in the design of material systems, because it causes deformation and leads to failure, also known as creep rupture, at stresses well below the expected ultimate stress. Creep can include recoverable and non-recoverable strains, which can be determined by allowing adequate time for the material to fully recover and observing the permanent plastic strain. The dashed line in the following figure illustrates this concept by showing a strain response that might occur if a material was unloaded in the middle of a creep test [61].
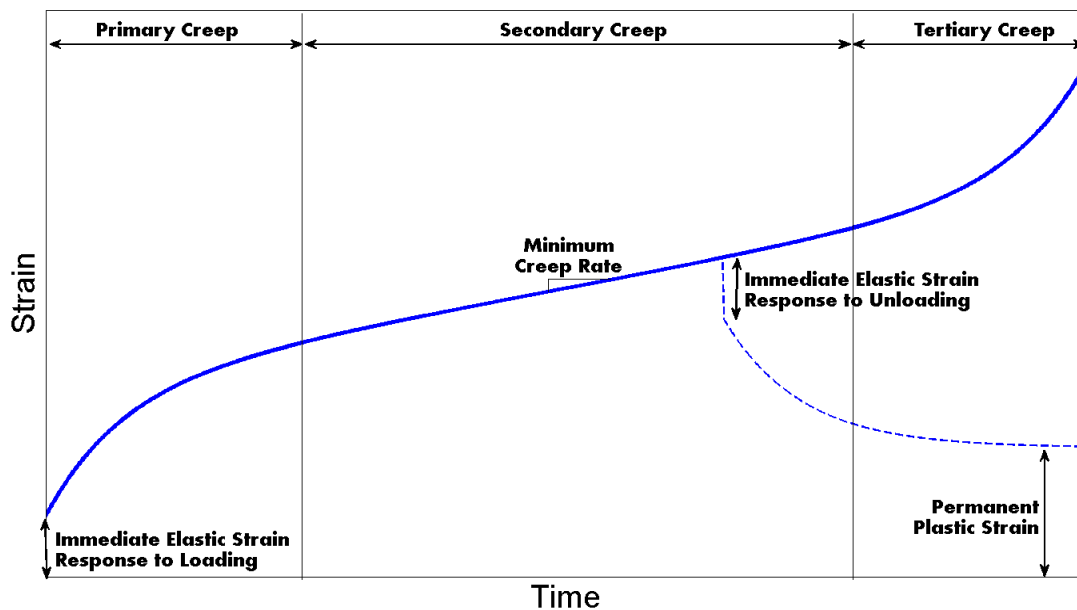
Figure 4: Creep Strain vs Time Based on Burgers Model

20

Unfortunately, creep is anything but typical. Creep curves can transition directly from primary to tertiary creep [61], consist of only primary creep [62], or lead to failure during secondary creep [20]. It should be noted from Andrade's work with metals under constant true stress, in the early 20th Century, that tertiary creep can be an artifact of creep tests under constant loading as the cross sectional area changes. Cannon and Langdon [23] also point out that grain growth can give the appearance of primary creep or make it tougher to recognize secondary creep. Sometimes, primary creep might exhibit an increasing strain rate, when the number of dislocations in the material multiplies. Creep curves, including the minimum creep rate, change with temperature and stress level, especially when different creep mechanisms are activated. For example, metals and ceramics only appear to creep significantly at temperatures above 30 to 60 percent of their melting temperatures, while some polymers and concrete creep at room temperature. The glass transition temperatures can have a large effect on creep in polymers. Creep also depends on chemical reactivity, including oxidation, and characteristics of the material's microstructure, such as grain size, additives, impurities, and other factors [63]. Sometimes, those other factors can make a big difference, such as shear modulus and porosity, which are discussed in the next section on *Models*. Ashby points out that creep strength at high temperatures is dependent on so many different factors that computer-aided methods become very helpful in material selection and design [21]. Given the importance of creep in aerospace design and the complex nature of creep behaviors, a brief review of creep mechanisms and models will provide a better understanding.

Mechanisms: Creep mechanisms are often categorized by those that involve dislocation motion, diffusion, and grain boundary sliding. Sometimes, creep mechanisms are categorized by those that occur within the lattice (i.e. intragranular) and those that involve grain boundaries (i.e. intergranular). Several popular texts serve as examples and provide further discussion, including Cannon [23], [64], Carter and Norton [65], Davidge [20], Dowling [63], Green[62], and Shames [61], which are the references for this section on creep *Mechanisms*, unless otherwise noted. Multiple mechanisms can be active in a creeping material at any given time, and those mechanisms can change with stress, temperature, grain size, additives, and other factors. Secondary creep is sometimes described as a balancing of hardening and softening mechanisms [62]. Consequently, primary and tertiary creep might be described as when creep mechanisms are not in balance, with primary creep indicating more strain hardening. Tertiary creep indicates more softening, typically when the formation of cracks and voids initiates failure in the material, especially along grain boundaries. The following paragraphs describe some of the creep mechanisms in each category that are well-established in the literature.

Dislocations, sometimes described as line defects in a lattice, include edge, screw, and combinations thereof, which might even produce dislocation curves or loops. Dislocation motion occurs when stress causes a dislocation to move from one location in a crystal lattice to another. When dislocations move along the slip planes of a lattice, it is called dislocation glide. When dislocations move to other slip planes, it is called dislocation climb. Often, glide and climb both occur, and the motion of dislocations is influenced by obstacles, such as impurities and other dislocations. These obstacles can cause pile ups, in which case the creep mechanism would be described as climb

controlled, since dislocations are not climbing around pile ups as fast as they are gliding to them. Alternatively, a lack of pile ups indicates a glide controlled process. Dislocations effectively vanish when they reach the surface of a material, possibly leaving a ledge, but new dislocations can also be created within the material (e.g. Frank-Read sources). Some phenomena, such as Bardeen-Herring sources, have even been attributed to simultaneously creating dislocations and causing climb [66]–[68], which Cannon described as supported by experimental creep data with ceramics [64]. With so many diverse mechanisms, dislocation motion becomes dependent on many variables, especially stress, and can play important roles in primary, secondary, and tertiary creep.

Diffusion refers to creep mechanisms that involve the movement of vacancies in a material. Vacancies tend to move toward areas of compression within the material, while atoms or ions tend to move toward areas of tension. Nabarro-Herring creep describes when vacancies move through the lattice, and Coble creep describes when vacancies move along grain boundaries. Of course, both creep mechanisms could occur at the same time, but often one will dominate over the other, especially because they are diffusing through different mediums and have different dependencies on grain boundary size. Diffusion in ceramics is sometimes complicated by the diffusing of both anions and cations, often referred to as ambipolar diffusion [64]. In this situation, the different species might have significantly different diffusivities, not only through the lattice, but also along grain boundaries. Assuming stoichiometry, the creep rate would then be driven by the slower species along the faster path. However, exceptions occur, so much so that Cannon and Langdon often used the diffusivity of the faster species through the lattice, usually the cation, to obtain the best fits of diffusion creep data for ceramics.

Ambipolar diffusion is suspected as a cause for higher creep rates in ceramics, compared to metals [64]. Ashby suggests that diffusional creep mechanisms can also be controlled by reactions at grain boundaries [21], which is also described as a situation where the grain boundaries, or interfaces, are not acting as perfect sources and sinks for vacancies[69]. Arzt provides a thorough description of interface-reaction controlled creep; a creep mechanism that simultaneously involves dislocations, diffusion, and grain boundaries…the diffusion of dislocations at grain boundaries [70]!

Grain boundary sliding occurs when grain boundaries are weaker than the crystalline lattice, which enables the grains to slide relative to one another, accommodated by other mechanisms. Alternatively, stress concentrations near grain boundaries could also cause grain boundary sliding to occur. If the grain boundaries have different compositions that soften at lower temperatures than the grains, activation of grain boundary sliding might occur well before other creep mechanisms. Ceramics display this behavior, when sintering aids cause the grain boundaries to take on a glassy phase, which could lead to even more variations in the creep mechanisms. For example, glass can be squeezed and flow from areas of compression to areas of tension. Also, grains could dissolve into the grain boundaries at locations of high stress, diffuse through the grain boundaries, and re-precipitate at locations of lower stress. Finally, Nabarro and de Villiers use the ideas of Ball, Hutchison, and Langdon to propose a grain boundary sliding mechanism, where dislocations pile up at grain boundaries and are annihilated as vacancies from the front of the pile up flow along the grain boundaries to other pile ups [71]. In these situations, the viscosity of the grain boundary becomes an important factor for the creep rate.

When grain elongation accompanies grain boundary sliding, it is referred to as Lifshitz sliding. This type of sliding requires vacancy diffusion along grain boundaries (Coble creep) or across entire grains (Nabarro-Herring creep). Lifshitz sliding might also occur if plastic flow occurs on either side of a grain, between the triple points. Other creep mechanisms that occur at grain boundaries include various mechanisms for cavity growth and crack propagation [23]. Cavity nucleation, growth, and coalescence along grain boundaries appear to be important mechanisms in the creep rupture of polycrystalline ceramics at high temperatures. The process might be nucleation- or growth-controlled, with increases in the grain boundary diffusivity increasing cavity growth rates and decreasing cavity nucleation rates. Higher applied stresses and higher applied strain rates are expected to increase both cavity nucleation and cavity growth rates [72]. Although, in creep rupture experiments with polycrystalline alumina, Dalgleish et al. [73] observed, below a crack blunting threshold (i.e. low stress and/or small flaw sizes), that strain at rupture was simply proportional to the inverse of the stress level. Under these conditions, creep rupture occurred due to the coalescence of creep damage. However, above the crack blunting threshold (i.e. high stress and/or large flaw sizes), creep rupture occurred due to the slow growth of flaws, which led to statistical variability in the failure strains. This enormous complex of creep mechanisms calls for a powerful and yet efficient model for researchers and engineers.

Models: Literature includes the development of well-established equations to model the physics of most of the creep mechanisms discussed in the previous section. For the most part, the models have been favorably compared with experimental data, although some inconsistencies occur. Despite the large number of creep mechanisms, Equation 1 generally models the strain rate for most creep mechanisms fairly well,

$$\dot{\varepsilon} = \frac{A\,D\,\mu\,b}{k\,T} \left(\frac{b}{d}\right)^m \left(\frac{\sigma}{\mu}\right)^n \tag{1}$$

where the terms include diffusivity (D), shear modulus (μ), the magnitude of the Burger's vector (b), temperature (T), grain size (d), and stress (σ). The parameter, A, brings together constants specific to the creep mechanism under consideration and sometimes grain boundary widths, while k represents Boltzmann's constant. The exponents, m and n, are often referred to as the grain size exponent and stress exponent, respectively. Cannon and Langdon suggest that A, m, n, and the activation energy of the diffusion process uniquely identify creep mechanisms, although A is usually not helpful, because it depends on the other parameters [23]. Table 3 appears to represent the consensus in contemporary literature for the exponents of well-established creep mechanisms. However, as previously mentioned, some inconsistencies occur and experimental results vary [20], [62], [74]. Bernard-Granger et al. provide a more detailed summary of creep mechanisms and exponents for fine grained polycrystalline ceramics at high temperatures [75].

Table 3: General Creep Equation Exponents for Some Creep Mechanisms

Creep Mechanism	m	n
Lattice Mechanisms		
dislocation climb (without glide)	0	3
dislocation climb & glide (glide controlled)	0	3
dissolution of dislocation loops	0	4
dislocation climb & glide (climb controlled)	0	4-5
dislocation climb by pipe diffusion	0	5
Boundary Mechanisms		
interface reaction control	1	2
vacancy flow through grains (Nabarro-Herring)	2	1
grain boundary sliding (without liquid phase)	2-3	1
vacancy flow along boundaries (Coble)	3	1
grain boundary sliding (with liquid phase)	3	1

Cannon and Langdon [23] note that ceramics often behave in two general categories: those associated with lattice mechanisms (m=0, n~3 to 5) and those associated with boundary mechanisms (m~2 to 3, n~1). When the grain size exponent is 0, creep behavior is independent of grain size and, thus, focuses on the diffusion of dislocations within the grains. Ceramics with higher stresses and/or larger grain sizes are often associated with stress exponents of 3 and 5 and have been shown to develop subgrain structures. Subgrains are characterized by small angles of lattice misorientation and a density of dislocations proportional to the square of the stress. When the stress exponent is 1, creep often depends on grain size and is associated with lower stresses and smaller grain sizes. Harper-Dorn creep is an exception (m=0, n=1), but is only important when grain sizes are large. The exponents m and n, along with the relative value of activation energies, provide good indicators of the conditions where certain mechanisms

will dominate creep behavior. For example, activation energies in grain boundaries are often less than in the lattice, so Coble creep becomes more favorable with lower temperatures, compared with Nabarro-Herring creep. Coble creep also becomes more favorable with smaller grain sizes, because its grain size exponent is larger than Nabarro-Herring creep [64]. As sources and sinks become less perfect for vacancies, creep rates decrease relative to the Coble and Nabarro-Herring models. This leads to interface control of creep rates becoming more important at smaller grain sizes and lower stresses [69].

Many thermally activated creep mechanisms follow the Arrhenius equation, presented as Equation 2. Assuming a viscous relationship between strain rate and stress (i.e. stress exponent of 1) leads to a convenient model relating strain rate to temperature,

$$\dot{\varepsilon} = A_1 \, \sigma \, e^{-\frac{Q}{RT}} \qquad (2)$$

where A_1 behaves primarily as a material property, Q represents the activation energy of the creep mechanism, and R is the gas constant [63]. Assuming power law creep behavior with stress exponent, n, characteristic minimum creep rate, $\dot{\varepsilon}_o$, and creep stress, σ_o, Equation 2 can be written as Equation 3 [21].

$$\dot{\varepsilon} = \dot{\varepsilon}_o \left(\frac{\sigma}{\sigma_o}\right)^n e^{-\frac{Q}{RT}} \qquad (3)$$

In Equations 2 and 3, $\dot{\varepsilon}$ typically corresponds to the minimum creep rate identified in Figure 4 on page 20. Equations 2 and 3 apply to thermally activated creep mechanisms, including diffusion, but Carter and Norton [65] note that they are only applicable over a small range of temperatures. Thus, it is practical to incorporate the Arrhenius equation into the general creep equation (Equation 1) through the diffusivity, D.

$$D = D_o \, e^{-\frac{Q}{RT}} \qquad (4)$$

In the general creep equation, D refers to the diffusivity of the relevant species through the lattice or grain boundary, depending on the creep mechanism, and is often defined as shown in Equation 4. Cannon and Langdon [23] note that many experimenters determine activation energy, Q, from the slope of a log $\dot{\varepsilon}$ versus $\frac{1}{T}$ plot. Such plots often fail to control for other parameters, especially the shear modulus, and leave out the $\frac{1}{kT}$ term, thus representing an apparent activation energy as opposed to the true activation energy. Additionally, Chokshi argues that experimental creep data cannot be used to determine diffusivities, when the experimental stress and grain size exponents do not match theoretical assumptions [76].

In the absence of reliable information at certain conditions, some parameters in the general creep equation, like shear modulus, might be estimated to improve modeling. For example, Equation 5 estimates the shear modulus (G) at high temperature (T),

29

$$G = G_o - (\Delta G)\, T \qquad\qquad (5)$$

where ΔG and G_o respectively represent the slope and intercept at zero Kelvin of a linear extrapolation of known, high-temperature shear moduli [64]. Porosity could also affect the shear modulus and, therefore, the modeling of creep. Equation 6 offers a means to adjust the shear modulus,

$$G = G_1 \left[1 + \frac{P\,\beta}{1 - P\,(\beta + 1)} \right] \qquad\qquad (6)$$

based on the full porosity shear modulus (G_1), volume fraction of porosity (P) and a constant (β) [77]. Additionally, it is recognized that porosity increases the effective stress on the material. Thus, Equation 7, known as the McClelland approximation,

$$\sigma_{eff} = \frac{\sigma_{app}}{1 - P^{2/3}} \qquad\qquad (7)$$

estimates the effective stress (σ_{eff}), based on the applied stress (σ_{app}) and porosity (P) [77]. Langdon also notes that porosity might affect the A parameter in the general creep equation, but such situations would be more complex to analyze. When incorporating these models of shear modulus and stress into the general creep equation, Langdon shows that porosity becomes much more important as the stress exponent increases. For

30

example, given a porosity of 7.5% and a β value determined from alumina, the creep rate increases less than 25% for a stress exponent of 1. However, if the stress exponent is 5, the creep rate increases by more than an order of magnitude [77].

Grain boundary sliding typically assumes Newtonian viscous flow (i.e. a stress exponent of 1). However, Nabarro and de Villiers [71] suggest this might be an oversimplification. Stress exponents for grain boundary sliding always appear less than stress exponents for lattice mechanisms, but Langdon and Vastava [78] commonly observed stress exponents for grain boundary sliding between 2.5 and 3.5. Examples of more complex grain boundary sliding mechanisms include those previously discussed by Nabarro and Ashby. Grain boundary sliding has been shown to account for a constant fraction of total creep strain over a range of stress levels [71]. However, in general, the fraction is expected to increase as stress level and grain size decrease [64], [79].

At high temperatures, grain boundary sliding can become the dominant mechanism, which means smaller grain sizes should increase the creep rate. However, at low temperatures, the Hall-Petch relationship could dominate, which means smaller grain sizes should decrease the creep rate. This suggests that there is a certain grain size that minimizes the creep rate for a given condition. Also, higher grain aspect ratios can reduce grain boundary sliding. Finally, as grain sizes approach the size of a specimen, grain boundary sliding can be expected to increase, because grains have fewer neighbors to constrict their movement. This effect has been shown with specimens that are 50 to 100 grain diameters in size [71].

Bird et al. [16] use the phenomenological approach in Equation 8 to determine

steady state creep rates, which involves pairing strains (ε) and strain rates ($\dot{\varepsilon}$) from data.

$$\dot{\varepsilon} = \dot{\varepsilon}_\delta + \dot{\varepsilon}_p \left[exp\left(\frac{-\varepsilon}{\varepsilon_o}\right)\right] \qquad (8)$$

This approach uses a best fit regression to determine the steady state strain rate ($\dot{\varepsilon}_\delta$),

primary strain rate ($\dot{\varepsilon}_p$), and initial strain (ε_o) [16].

While the previous models focused on strain rate, the Larsen-Miller parameter

focuses on creep rupture or the time to reach an arbitrary strain. The basic assumption of

the Larsen-Miller parameter ($P_{Larsen\text{-}Miller}$) is that, for a given stress level (σ),

$$P_{Larsen-Miller} = T\left[\log t_r + C\right] \qquad (9)$$

the time to rupture (t_r) and temperature (T) are consistently related. The constant (C) is

usually around 20. The Larsen-Miller model provides remarkably good fits, but might

not be valid across phase changes [80]. In general, all of the models discussed in this

section could deviate from experimental data at times, especially when applying the

models to new materials systems at high temperatures. Thus, it is prudent to specifically

discuss the creep behaviors that have been experienced with UHTCs.

Experiences with UHTCs: Very little work has been performed on the creep of UHTCs. A few creep experiments looked at the creep of ZrB_2, but only one enables a comparison between creep performance in an inert environment and air. All of the experiments with ZrB_2, except two, utilize a flexural creep testing configuration. Also, with the exception of the historic work by Rhodes et al. [18], Winder [13] represents the only known creep results for HfB_2 at high temperatures. Winder's experiments were all conducted in air and, thus, coupled with oxidation effects. Finally, only Rhodes et al. provide a look at how creep behavior might vary with SiC content in an inert environment. Additional discussions on the effect of oxidation on creep may be found in the section on *Oxidation Behavior.* The following paragraphs discuss these issues, including all of the UHTC creep experiments found in the literature.

Winder's work represents the only contemporary creep results for HfB_2 at high temperatures [13]. It focuses on the creep testing of HfB_2, both 0 and 20% SiC by volume, between 25 and 100 MPa in compression, at 1500°C in air. These experiments identified grain boundary sliding accommodated by diffusion as the dominant creep mechanisms, with stress exponents between 1.7 and 2.3. Since all of the experiments were conducted in air, they are coupled with oxidation effects. This provides great information regarding creep behavior in an oxidizing environment, plus a unique look at the effects of stress on oxidation. However, it will be difficult to decouple the effects of oxidation from the results. Similar experiments in an inert environment should provide insightful comparisons to Winder's results and a solid foundation for understanding and modeling the creep of UHTCs at other conditions and with different compositions.

Gangireddy et al. published a work that enables comparisons between results in an inert environment and air. The experiments looked at the flexural creep of ZrB_2 with 30% SiC by volume, 20 to 50 MPa, at temperatures between 1700 and 2000˚C. A novel, electromagnetic mechanical apparatus (EMMA) was employed. The method relied on conductivity of the specimen, heating it resistively with direct current, and mechanically loading it with no-contact, Lorentz force. The experiments occurred in a N_2 atmosphere with 0.25% O_2. The creep rates in air were slightly higher than in the inert environment, attributed to the geometric effects of oxidation. After applying corrections in Equations 10 and 11, the results in the inert environment and air closely matched.

$$\sigma_{true} = \sigma_{nominal} \frac{t^2}{(t - 2\, t_{oxide})^2} \tag{10}$$

$$\dot{\varepsilon}_{corrected} = \dot{\varepsilon} \left(\frac{\sigma_{nominal}}{\sigma_{true}}\right)^2 \tag{11}$$

The creep tests ran for a maximum of 300 seconds and achieved strains around 0.5%. The authors observed no gross changes in the microstructure or cavitation, arguing symmetric creep and steady strain rates. Gangireddy et al. concluded that the stress exponent was 1.4±0.4 and, through extrapolation, the results were comparable to lower temperature results published by Talmy et al., discussed in the following paragraph [15].

Talmy et al. performed flexural creep experiments with ZrB_2 in an oxidizing environment. The experiments included temperatures of 1200 to 1500˚C, stress levels of 30 to 180 MPa, additives of SiC from 0 to 50% by volume, and two different SiC particle sizes (2 and 10 μm). All of these variables strongly affected creep behavior. The effect of grain size on creep was not discussed, although grain size decreased noticeably above the phase percolation limit (i.e. at and above 25% SiC by volume). All the experiments exhibited primary and secondary creep, but tertiary creep was only exhibited at 1450 and 1500˚C. The authors reported stress exponents from 0.7 to 1 for SiC content 0 to 25% by volume and 2.2 to 2.3 for SiC content 50% by volume. For ZrB_2 with 50% SiC by volume, the stress exponent increased with temperature, from 1.3 at 1300˚C to 2.5 at 1500˚C. The increases in stress exponent are explained as diffusion contributing less and grain boundary sliding contributing more to creep deformation, while activation energy remains unchanged. Activation energy increased linearly with SiC content [17].

Bird et al. showed similar trends in flexural creep experiments with ZrB_2 in an inert environment. The experiments included temperatures of 1400 to 1820˚C, stress levels of 16 to 97 MPa, and only specimens with a SiC content of 20% by volume. As expected, steady state creep rates increased with temperature and stress. The authors observed primary and secondary creep, but not tertiary. The stress exponent was 1 at low temperatures (i.e. ≤ 1500˚C) and 1.7 to 2.2 at high temperatures (i.e. > 1500˚C). Up to 1600˚C, the authors suggest that non-sequential creep mechanisms are at work, where the contribution of grain boundary sliding increases with stress and diffusion decreases. However, above 1600˚C, a drop in the activation energy indicates sequential creep mechanisms, where grain and interphase boundary sliding dominate creep behavior [16].

35

Guo et al. also performed flexural creep experiments with ZrB_2 in an inert environment. The experiments included temperatures of 1500 and 1600°C, only one stress level (19 MPa), and specimens with a SiC content of 30% by volume. The steady state creep rate increased with temperature. The authors observed primary and secondary creep, but not tertiary. Creep mechanisms could not be determined, but cavity nucleation and growth was observed at 1600°C, especially at triples points involving SiC grains [10].

Meléndez-Martínez et al. performed uniaxial creep experiments in compression with ZrB_2 in an inert environment. The experiments included temperatures of 1400 to 1600°C, stress levels of 47 to 472 MPa, and specimens of pure ZrB_2 and ZrB_2 with 4% Ni by weight as a sintering aid. As with Talmy et al., the pure ZrB_2 was more porous. As expected, steady state creep rates increased with temperature and stress. The authors reported a stress exponent of 1.7 at 1500°C for the pure ZrB_2. At 1600°C, a stress exponent of 0.6 was reported at lower stresses and appears to be near 2 at similar stresses. The authors do not discuss the apparent transition of creep behaviors around 220 MPa in the 1600°C experiments. The pure ZrB_2 had lower creep rates, which were consistent with the authors' argument that the Ni-doped ZrB_2 resulted in a softer phase at the grain boundaries. The Ni-doped ZrB_2 exhibited a stress exponent of 1.5, but had to be determined at stress levels between 10 and 20 MPa due to catastrophic failures of the specimens at higher stresses [14].

Bernard-Granger et al. provide an interesting look at grain size and density in the course of compressive creep experiments on polycrystalline α-alumina in air. The experiments included temperatures of 1175 to 1225°C, stress levels of 40 to 200 MPa,

36

and average grain sizes around 0.42 µm. Stress jumps during the creep experiments

ensured that grain growth did not affect calculations of the stress exponents, which had

an average value of 2. Temperature jumps were also used to determine instantaneous

activation energies. The authors recognized that grain growth in polycrystalline materials

cannot be controlled during creep experiments and often prevent the creep rate from

achieving steady state. To ensure the effects of grain growth were appropriately

considered, they used a general form of the creep equation to show the expected

relationship between strain rate and grain size at constant temperature and stress,

assuming one controlling creep mechanism and activation energy.

$$\ln(\dot{\varepsilon}_{qs}) = K - m \ln(d) \qquad (12)$$

Equation 12 includes the pseudo steady state strain rate ($\dot{\varepsilon}_{qs}$), a constant (K), the grain

size exponent (m), and the grain size (d). The authors then made a correlation between

grain size and strain in order to make calculations of the grain size exponent. Although

the calculated grain size exponents were non-conventional, they demonstrated that the

grain size exponent starts out relatively high and then transitions, at a critical grain size,

to a value close to 1. The authors also suggest that the grain size exponent can be

determined from measurements of the strain rates and grain sizes at the beginning and

end of a creep experiment, once again under constant temperature and stress. They offer

Equation 13, where subscripts 1 and 2 represent the beginning and end of the creep

experiments, respectively. Considering the material might go through a period of

37

primary creep, subscripts 1 and 2 might better refer to two points in time, a sufficient distance apart, but both occurring during the period of pseudo steady state creep.

$$m = -\left[\frac{\ln\left(\frac{\dot{\varepsilon}_2}{\dot{\varepsilon}_1}\right)}{\ln\left(\frac{d_2}{d_1}\right)}\right]_{\sigma,T} \tag{13}$$

Bernard-Granger et al. also observed that high temperature creep tests at low stresses could lead to densification of the material, while higher stresses would decrease the density due to cavity growth. Comparison with a heated, but not loaded, specimen showed that as-sintered cavities have a polygonal geometry and are mostly found at triple points, while creep induced cavities have a penny shape and are mostly found at grain boundaries. Differences in the grain sizes of the crept and uncrept specimens indicated that creep accelerates grain growth, referred to as dynamic grain growth. Above the critical grain size, Bernard-Granger et al. concluded that creep occurs due to grain boundary sliding, where an in-series interface reaction mechanism is controlling at low temperatures and/or stresses, and the relocation and growth of pre-existing cavities is controlling at high temperatures and/or stresses. Both controlling mechanisms are suspected of being limited by the diffusion of aluminum cations [75].

Many other works have been published about the high temperature creep performance of polycrystalline ceramics, including some older experiments with UHTCs. For example, Rhodes et al. [18] provide a cursory look at the uniaxial, compressive creep performance of HfB_2 and ZrB_2 in a vacuum with additions of SiC and C, from 800 to

1800˚C, at a stress level of about 172 MPa [18]. The discussion focuses on the

observation that these materials are capable of exhibiting creep, including primary,

secondary, and tertiary creep. They calculate activation energies from 52 to 139

Kcal/mol and use information from high-temperature bending strength tests to estimate a

stress exponent of about 2.5 and a grain size exponent between 1 and 2. From these

observations, the authors suggest diffusion and grain boundary sliding as controlling

creep mechanisms. Spivak et al. [12] investigate the flexural creep of TiB_2-TiC and

ZrB_2-ZrN in helium with about 4 to 6% porosity, 2052 and 2291˚C, and 5 to 196 MPa.

The focus of the discussion is on the ideal composition for super-plasticity. Grain size is

identified as a strong factor, and creep mechanisms are not discussed. Kats et al. [11]

take a look at the flexural creep of TiB_2 and ZrB_2 in helium with varying additions of TiC

and ZrC, respectively, with data in a temperature range from 1700 to 2420˚C and stress

levels from 5 to 30 MPa. These works should be recognized for their early and

motivational investigations into the creep performance of UHTCs. However, they do not

provide further insight with respect to the questions posed in the *Research Focus*. None

of the other works pertaining to the creep behavior of UHTCs include HfB_2 or ZrB_2 as a

primary alloy. Several works consider the creep of transition metal carbides, but these

materials generally do not possess the desired oxidation resistance [81]–[95]. Since

oxidation is one of the key concerns in these works and in the *Problem Statement*, some

review of the topic is warranted.

2.3 Oxidation Behavior

Concepts: Oxidation generally refers to an increase in the oxidation number of an atom, although in this work it often specifically refers to forming an oxide from a non-oxide material, such as converting hafnium diboride and silicon carbide into hafnia, silica, and/or boria. The oxidation number is determined by treating the atom as a quasi ion, assigning shared electrons to the more electronegative atom, and determining the charge of the quasi ion. In simple terms, oxidation is sometimes described as an atom losing one or more electrons in a reaction, such as when oxygen reacts with and takes electrons away from metals. Alternatively, reduction is sometimes described as an atom gaining one or more electrons. To determine whether a given oxidation-reduction reaction will proceed, Van't Hoff's equation, Equation 14, provides a thermodynamic calculation for Gibb's free energy at non-equilibrium conditions and constant temperature.

$$\Delta G = R\ T\ \ln\frac{Q}{K} \qquad\qquad (\ 14\ )$$

In this formulation, considering standard methods for calculating the equilibrium constant, K, a negative value of Gibb's free energy, ΔG, indicates that equilibrium would be approached by the formation of more products. R represents the gas constant, T represents the temperature, and Q represents the activity quotient, which is similar to the equilibrium constant, but with values for the initial state [40].

The kinetics of oxidation often affect the design and life of material systems. Oxidation rates are typically measured in weight gained per unit of area. When chemical reaction rates limit oxidation, the relationship between the oxidation rate and time is often linear (Equation 15). When ion diffusion limits oxidation, the relationship is parabolic (Equation 16). Sometimes, materials oxidize logarithmically (Equation 17), quickly at first and slowing down to a very low rate.

$$W = k_L \, t \qquad\qquad\qquad (15)$$

$$W = \sqrt{k_P \, t} + C \qquad\qquad\qquad (16)$$

$$W = k_e \, \log{(C \, t + A)} \qquad\qquad\qquad (17)$$

Equations 15, 16, and 17 include the weight gain per unit area (W), the rate constant (k), time (t), and constants A and C. Exposing a flat, metal plate to air represents a common oxidation situation. If cations from the metal diffuse toward the air to cause oxidation, the oxide will form on the surface. If anions from the air diffuse toward the metal to cause oxidation, the oxide will form under the surface at the metal-oxide interface [96].

Mechanisms: Only those oxidation mechanisms that are applicable to the present research effort will be reviewed, because an exhaustive review of oxidation mechanisms

would be lengthy. In light of Van't Hoff's equation, it is generally recognized that changes in temperature, stoichiometry, and the initial state, frequently in terms of the partial pressures of reactants and products, drive oxidation. For ceramics, ionic conductivity and diffusion could play an important role. Diffusion along grain boundaries and dislocations often proceeds faster than through the bulk material [65].

With respect to the *Research Focus*, the stoichiometric reaction in Equation 18 describes the oxidation of crystalline HfB$_2$ when reacted with gaseous oxygen.

$$HfB_{2(C)} + \frac{5}{2} O_{2(g)} \rightarrow HfO_{2(c)} + B_2O_{3(l)} \qquad (\,18\,)$$
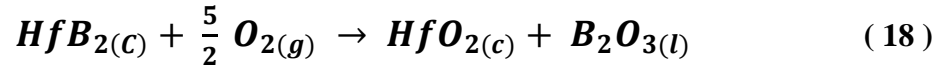
The Gibb's free energy, ΔG_{rxn}^o, for this reaction is given by Equation 19,

$$\Delta G_{rxn}^o = -2003 + 0.374\,T\,(kJ) \qquad (\,19\,)$$

where T represents temperature [9]. Thus, the oxidation of HfB$_2$ in air is expected to proceed at all temperatures considered in this research by the action of oxygen diffusing from the air, through the oxide scale, and reacting with HfB$_2$ at the substrate-oxide interface. Obviously, this is a simplified description of the oxidation of HfB$_2$. Li et al. provide detailed chemical equations, models, and volatility diagrams for the oxidation of HfB$_2$ as a function of temperature and O$_2$ partial pressures. It is interesting to note that as the partial pressure of O$_2$ decreases towards an equilibrium oxygen partial pressure,

which is very low, there is an expected increase in the partial pressures of the following gases: BO, B_2O_2, B_2O, B, HfO, Hf, and B_2. Below the equilibrium oxygen partial pressure, which is 9.8×10^{-16} Pascals at 1227°C, the partial pressures of all the B-O and hafnium vapor species decreases [97]. At 1500°C, the equilibrium oxygen partial pressure would be 1×10^{-10} Pa.

When B_2O_3 melts around 450°C [41], it fills the pores of the HfO_2, and a layer of B_2O_3 might also sit on top of the HfO_2. B_2O_3 evaporates around 1000°C [33], removing the top layer of B_2O_3. As the temperature rises from approximately 1000°C to 1800°C, the B_2O_3 recedes within the pores of the HfO_2. Above 1800°C, all of the B_2O_3 evaporates. Around 1400°C, the mechanism that limits the HfB_2 oxidation rate transitions from oxygen diffusion through the liquid B_2O_3 to Knudson diffusion of oxygen through the HfO_2 pores. This assumes that mechanisms acting through the HfO_2 are negligible [26]. HfO_2 melts at 2800°C [41].

Silicon additives, such as SiC or $MoSi_2$, can improve the oxidation resistance of HfB_2 by the formation of SiO_2 at temperatures beyond 1100°C. The SiO_2 reacts with B_2O_3 to form a protective top layer of borosilicate glass. SiO_2 melts at 1725°C [41] and has been completely removed from the surface of HfB_2 specimens by arc jets at temperatures above 2200°C. The SiO_2 top layer protects the underlying material from oxidation [42].

Models: Parthasarathy et al. published a model for the oxidation of metal diborides with [98] and without [26] SiC additives. The model for metal diborides without SiC additives, published in 2007, considered the oxidation of HfB_2, TiB_2, and

ZrB$_2$ from 1000 to 1800°C, which compared well with the limited experimental results found in literature. The model predicts scale thickness (L), recession (R), and weight change (ΔW) by assuming an isothermal process, slow gas flow conditions, and the stoichiometric form of the oxidation reaction presented in Equation 18. The model also assumes the air is only composed of N$_2$ and O$_2$, the surface is a perfect sink for the evaporation of liquid B$_2$O$_3$, and that the transport of oxygen through the metal oxide is negligible compared to the transport of oxygen through the pores of the metal oxide, where the turtuosity of the pores is neglected. Although Equations 20, 21, and 22 indicate the oxidation of ZrB$_2$, they may be generally applied to other metal diborides, when using the appropriate pore fraction, pore radius, thermodynamic data, and physical properties. Equation 20 gives the scale thickness (L). Equation 21 gives the recession of the oxidized metal diboride (R). Equation 22 gives the weight change of the oxidized metal diboride (ΔW).

$$L = \sqrt{\frac{4}{5} t D_{O_2} \left(\frac{M_{ZrO_2}}{\rho_{ZrO_2}}\right) \left(\frac{f}{1-f}\right) \left(\frac{C_{O_2}^a - C_{O_2}^i}{1-q}\right)} \qquad (20)$$

$$R = L (1 - f) \left(\frac{M_{ZrB_2}}{M_{ZrO_2}}\right) \left(\frac{\rho_{ZrO_2}}{\rho_{ZrB_2}}\right) \qquad (21)$$

$$\Delta W = \frac{L \rho_{ZrO_2} (1-f) + h f \rho_{B_2O_3} - R \rho_{ZrB_2}}{A} \qquad (22)$$

44

Equation 20, 21, and 22 use variables for time (t), diffusivity (D), molar volume (M), density (ρ), the fraction of the metal oxide that provides a porous and continuous pathway for gaseous diffusion (f), the concentration at the oxide scale/ambient air interface (C^a), the concentration at the B_2O_3 liquid/gas interface (C^i), and surface area (A). The variable q is given by Equation 23,

$$q = \frac{\Pi_{O_2-B_2O_3}\left(P_{O_2}^i - P_{O_2}^s\right)}{D_{O_2}\left(C_{O_2}^a - C_{O_2}^i\right) + \Pi_{O_2-B_2O_3}\left(P_{O_2}^i - P_{O_2}^s\right)} \tag{23}$$

which contains variables for the oxygen permeability coefficient (Π) and partial pressure (P). Equation 24 shows the scale thickness and q can then be used to calculate the thickness of the B_2O_3 layer (h).

$$h = q\,L \tag{24}$$

The Parthasarathy et al. model for metal diborides with SiC additives [98], published in 2012, considered the oxidation of HfB_2 and ZrB_2 from 1200 to 2200°C, which compared well with the limited experimental results found in literature for furnace conditions, but not for arc jet conditions. With more reactions and layers of oxidation scale to consider, this SiC-containing model becomes more complicated than the previous model. Thus, Figure 5, used with permission, conveniently illustrates the model, along with some of its defined variables and chemical reactions.
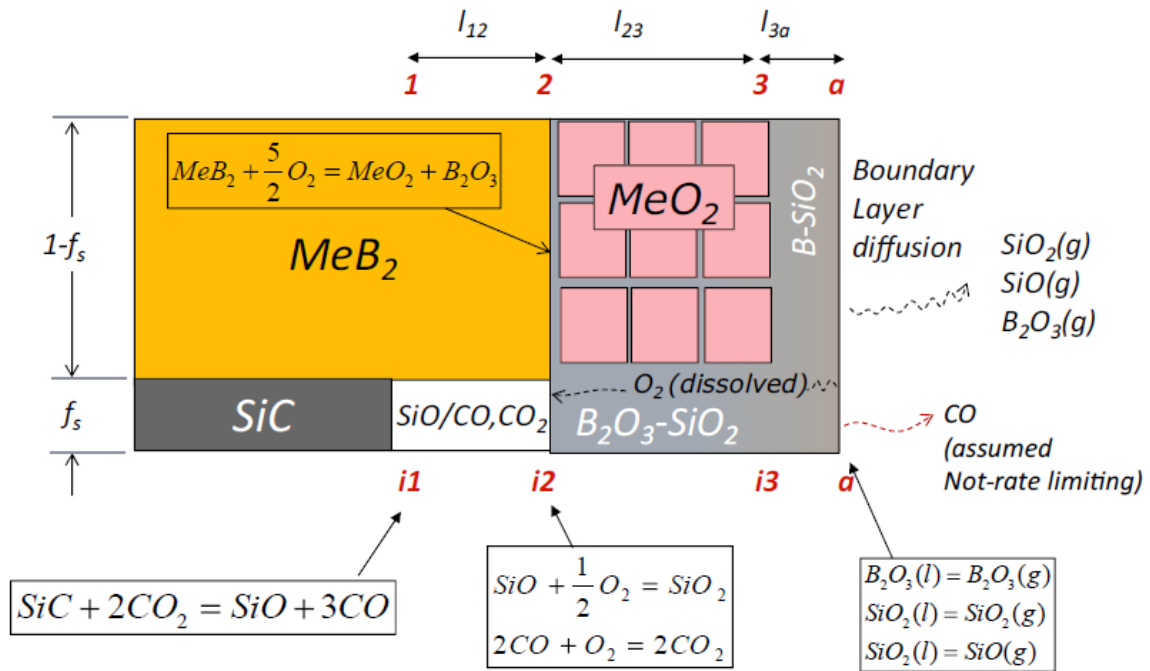
Figure 5: Model of an Oxidized Metal Diboride with SiC
Copyright © 2011, The American Ceramic Society,
Journal of the American Ceramic Society, Used with Permission [98]

Equations 25 through 30 model recession (R), depletion layer thickness (l_{12}), oxide scale thickness (l_{23}), external glassy layer thickness (l_{3a}), and net weight gain (W) by using many of the same assumptions as the previously described model. However, the addition of SiC requires additional assumptions with regard to the chemical reactions and transport of products depicted in Figure 5, including the treatment of borosilicate glass instead of strictly B_2O_3.

$$\frac{dR_{SiC}}{dt} = |J_{SiO-12}| \frac{V_{SiC}}{f_s} \tag{25}$$

$$\frac{dR_{MeB_2}}{dt} = \frac{dl_{23}}{dt} \frac{V_{MeB_2} f_{MeO_2}}{V_{MeO_2} (1-f_s)} \tag{26}$$

$$l_{12} = R_{SiC} - R_{MeB_2} \tag{27}$$

$$\frac{dl_{23}}{dt} = V_{MeO_2} \left(|J_{O_2-32}| - \frac{3}{2}|J_{SiO-12}|\right) \frac{2}{5} \frac{1}{f_{MeO_2}} \tag{28}$$

$$\frac{dl_{3a}}{dt} = \left(\frac{dl_{23}}{dt} \frac{f_{MeO_2}}{V_{MeO_2}} - |J_{B_2O_3-vap}|\right) + (|J_{SiO-12}| - |J_{SiO_2-vap}| - |J_{SiO-vap}|) - \frac{dl_{23}}{dt} f_g \tag{29}$$

$$W = l_{23} \left(f_{MeO_2} \rho_{MeO_2} + f_g \rho_g\right) + l_{3a} \rho_g - R_{SiC} f_s \rho_{SiC} - R_{MeB_2} (1-f_s) \rho_{MeB_2} \tag{30}$$

Equations 25 through 30 use variables for time (t), the flux of moles per unit area per unit time (J), molar volume (V), the volume fraction of SiC in the substrate (f_S), the volume fraction of MeO_2 in the 2-3 region (f_{MeO2}), the volume fraction of borosilicate glass in the scale (f_g), and density (ρ). Numbers in the subscripts refer to locations in the previous figure of the model, while the "vap" and "Me" subscripts refer to evaporation and metal, respectively. The Parthasarathy et al. publications contain additional formulas to assist in modeling many of the variables presented in these equations.

Experiences with UHTCs: Experiences with the oxidation of UHTCs have been well documented in the literature, dating at least as far back as Kaufman et al. in the early 1960s [30]. Based on these experiences, Parthasarathy et al. provide excellent narratives on the oxidation behavior of metal diborides, with and without SiC additives [26], [98], including comparisons to the previously presented oxidation models. The following paragraphs provide some additional insights and perspectives on the oxidation behavior of UHTCs.

Talmy et al. observed varying thickness of the oxidation layer in different regions (i.e. compressive, neutral, and tensile) of their flexural creep test specimens, which led to the conclusion that both compressive and tensile stresses enhance oxidation [17]. Bird et al. support the claim that oxidation might affect creep rates and pursued experimentation in an inert environment [16]. On the other hand, Meléndez-Martínez et al. used creep tests in an inert environment to support the position that the effect of grain boundary softening on creep rates is more important than oxidation [14]. Additionally, as described in the *Creep Behavior* section, Gangireddy et al. argued that differences in the creep rates between inert and air environments could simply be attributed to the geometric effects of oxidation [15]. However, Tian et al. showed through furnace testing of ZrB_2 with 20% SiC by volume, at 1500˚C, that the oxidation mechanism changes between an oxygen partial pressure of 1 and 1.5 kPa. Above 1.5 kPa, the authors observed parabolic, diffusion rate controlled kinetics and the same four layers modeled by Parthasarathy et al. However, below 1 kPa, the authors observed linear, reaction rate controlled kinetics and only two distinct layers (i.e. the zirconia-rich layer and the unaffected layer). The absence of the SiC depleted layer was attributed to the lack of a

protective surface layer, which kept oxygen partial pressures high enough under the zirconia-rich layer to minimize the active oxidation of SiC [99].

Nguyen et al. investigated the oxidation performance of three popular UHTCs between 1200 and 1400˚C in an environment composed of 90% water vapor and 10% oxygen at 1 atm. The UHTCs included HfB_2 with 20% SiC, ZrB_2 with 20% SiC, and ZrB_2 with 30% C and 14% SiC, all percentages by volume. Low velocity water vapor did not significantly affect oxidation rates. However, higher gas velocities accelerated recession of the materials and led the authors to the conclusion that these UHTCs are not appropriate for long-term use in aeropropulsion applications [100].

Regarding another issue, care should be taken when correlating weight changes to oxidation. Thermogravimetric analysis (TGA) and differential thermal analysis (DTA) of nanocrystalline HfB_2 showed an initial weight decrease from room temperature to about 400˚C, significant weight increase from 400 to 723˚C, and then slowing of the weight increase to nearly zero at 1000˚C [33]. These observations are consistent with the melting and evaporation temperatures of B_2O_3, but the initial weight decrease was attributed to the removal of water from the sample.

The parabolic oxidation rate constants of Si are about 4 orders of magnitude lower than Hf at 1250°C. However, SiO_2 melts at 1725˚C [41]. Carney reports that the flow of SiO_2 is a critical factor affecting oxidation up to 2000˚C, as well as increases in the porosity of HfO_2. Experiments with HfB_2 containing 20% SiC by volume showed that SiO_2 provides a complete protective layer around 1600˚C, reaches maximum thickness around 1900˚C, and then decreases at higher temperatures. Increases in the porosity of HfO_2 correlate with an expected tetragonal phase transition around 1700˚C, which results

49

in an approximate 3.5% volume reduction. Thus, improvements in oxidation

performance above 1800˚C should focus on additives to increase the viscosity or melting

point of the protective SiO_2 layer or to stabilize the HfO_2 crystal structure [42].

Levine et al. do not look favorably on the potential performance of UHTCs with

SiC additives for hypersonic flight in the upper atmosphere, because the protective B_2O_3

and SiO_2 layer would be lost. They suggest HfO_2 would be a good oxidation barrier, if

perfect. Unfortunately, HfO_2 is identified as a bad choice, because of a tendency to form

porous scales, develop oxygen lattice vacancies, and change phases and volumes at high

temperatures [101], although it is not expected to melt until around 2800˚C [41]. This,

however, did not rule out improving UHTC performance with composite designs [101].

From both Levine et al. and Carney's perspectives, it is apparent that attention should be

given to different additives and their effects on oxidation and creep.

2.4 Additives that Affect Creep and Oxidation Behavior

Concepts: Although additives serve many purposes in the development of material systems, this research focuses on creep behavior and oxidation resistance. Thus, for example, additives that improve toughness and machinability might be ignored in this literature review, unless they are suspected of affecting the analysis and conclusions of this research with respect to the creep and/or oxidation resistance of UHTCs. Most of the additives discussed in the literature focus on improving the densification, high temperature strength, and oxidation resistance of UHTCs. The effects of SiC additives will not be covered in this section, because they were covered in the previous sections on *Creep Behavior* and *Oxidation Behavior*.

Creep: Additives that commonly affect the creep of UHTCs include sintering aids. Sintering aids are often added in the sintering process to reduce the porosity and improve the densification of the material. Sintering aids are also used to reduce the temperatures and/or heating times of the fabrication process, resulting in smaller grain sizes. These effects of sintering aids have been shown to improve the high temperature strength of UHTCs. Sintering aids can not only affect creep rates, but entirely change the controlling creep mechanisms. Sintering aids have been shown to affect the composition and properties of the grain boundaries within UHTCs. Thus, different sintering aids could affect the contribution of grain boundary sliding to the overall strain rate. In general, different grain boundary compositions could change the activation energy for grain boundary sliding, the thickness of the grain boundary, and the viscosity of the grain boundary. This could change the grain sizes, temperatures, and stresses at which grain

boundary sliding controls the creep rate [65]. The previous sections on *Creep Behavior*

and *Hafnium Diboride* include some of the more general effects that additives can have

on the creep and mechanical performance of UHTCs, primarily through discussions of

experiments that used SiC as an additive.

When additives form discrete particles in the matrix, creep can be affected.

Wilkinson [102] provides a thorough review of experimental data and models that relate

to the creep of multiphase ceramics. Wilkinson also presents a classification system that

eloquently describes how harder phases can percolate networks of point-to-point and

facet-to-facet contacts. These networks can greatly increase creep resistance, with

volume fraction and morphology of the reinforcing particles being important factors.

Oxidation: As exemplified in the previous discussions of SiC, additives can have

a significant effect on the oxidation of UHTCs. Most notably, additives can change the

properties of the surface layer that protects the UHTC. Changes can occur to the

viscosity and/or melting point of the protective layer. Consequently, additives can affect

the ability of the protective layer to maintain its protective capabilities during off-gassing

and the rate that oxygen diffuses through the protective layer. Not only can additives

affect the ability of a glassy phase to fill in the pores of the UHTC's oxide, but additives

can also affect the microstructure of the oxide [103]. Ideally, the additive would reduce

the porosity of the oxide and decrease the rate that oxygen diffuses through the oxide

layer and oxidizes the substrate. The following section reviews some of the effects that

additives have been shown to have on the oxidation resistance and mechanical

performance of UHTCs.

Experiences with UHTCs: Some suspect that other silicides might perform better than SiC in terms of improving oxidation resistance, because carbon-based gases would not be a byproduct of the additive's oxidation. At high temperatures, UHTCs with SiC additives sometimes experience a breakdown of their protective surface layer as carbon monoxide and/or carbon dioxide break through the surface. Sciti et al. studied the oxidation resistance of HfB_2 with 15% by volume additions of $MoSi_2$ and $TaSi_2$. $MoSi_2$ showed good performance up to 1900°C, but $TaSi_2$ showed signs of destabilizing the HfO_2 scale and a protective surface layer that detaches from the rest of the material [104]. Di Maso et al. showed similar results, where the $TaSi_2$ additive appeared to improve the performance of the protective surface layer, but might have negatively affected the HfO_2 scale [105]. In a separate experiment, Sciti et al. also showed that HfB_2 with 20% $MoSi_2$ by volume appears to change the oxidation kinetics from parabolic to logarithmic [43]. In terms of mechanical properties, results showed that the additives enabled the HfB_2 to be brought to full density through spark plasma sintering and with smaller grain sizes. $MoSi_2$ resulted in higher strength at room temperature and 1500°C, but $TaSi_2$ resulted in higher toughness [43], [106]. In some cases, dark pockets of SiO_2 formed and reduced high temperature strength [107].

Opeka et al. looked at the oxidation effects of several transition metal additives to ZrB_2 with 25% SiC by volume. The additives were all 10% by molar ratio, yielding the corresponding oxides in the protective surface layer, and improving overall oxidation resistance up to at least 1600°C. From most effective to least effective, the additives were TaB_2, VB_2, NbB_2, TiB_2, and CrB_2. The authors note that this trend corresponds to the cation's charge and conclude that the additives improve oxidation resistance by

53

promoting immiscibility in the protective surface layer [41]. Peng and Speyer also studied the effect on oxidation of several different additives to ZrB_2. The experiments included SiC in 11 of the 13 compositions tested and also varied the ratios of B_4C, TaB_2 and $TaSi_2$. TaB_2 and $TaSi_2$ additions to ZrB_2 with SiC and B_4C were shown to improve oxidation resistance through about 1550˚C [108]. At 1800˚C , Hu et al. found that additions of AlN, LaB_6, La_2O_3,$TaSi_2$, TaB_2, and TiB_2 all negatively affected the oxidation resistance of ZrB_2 with 20% SiC by volume [109].

Carney et al. showed that 3% by volume additions of tungsten boride (WB) and tungsten carbide (WC) improved sintering and reduced the grain size of a HfB_2 material system with 15% SiC by volume. Most notably, these additives appeared to reduce the oxide scale thickness by 30%, but only at 2000˚C. The authors concluded that the additives increased the viscosity of the protective surface layer and the density of the oxide layer, thus decreasing the rate of oxidation of the UHTC [103]. Zhang et al. showed similar effects with the addition of WC to ZrB_2 [110].

Weng et al. showed that a 6% by volume addition of Si_3N_4, as a sintering aid, to HfB_2 with 20% by volume of SiC generally improved mechanical properties and oxidation resistance. The additive was shown to eliminate oxygen impurities, improve densification, and limit grain growth, thus greatly improving flexural strength. Fracture toughness also improved, attributed to an effect of the additive on the grain boundaries. Oxidation resistance was provided by the protective surface layer, which also contained hafnium, carbon, and nitrogen [111]. Fahrenholtz et al. emphasized that the removal of oxygen-based impurities is a critical factor in the densification of UHTCs, in this case using B_4C additives in ZrB_2 [112].

III. Methodology

The *Research Objectives* were primarily investigated through experimentation. Although the *Literature Review* showed that some theories and models have been developed based on extensive experimental results obtained for other materials, and a few data points have been collected for UHTCs, at present, no single model reliably predicts the creep of UHTCs at high temperatures in an inert or oxidizing environment. These are critical design parameters in the application of UHTCs to address the *Problem Statement*. At this point, it would be difficult to assess the value of further theoretical and modeling developments with respect to the research objectives, unless these modeling developments were validated by experimental results. Thus, the following sections of the methodology describe the experiments that were conducted in order to make tangible gains in the understanding and characterization of the creep and oxidation of UHTCs in extreme environments.

3.1 Research Materials

The following sections describe the materials used in this research effort (HfB_2-0%, -10%, -20%, and -30% SiC by volume), as well as the processes used to produce and characterize the materials.

Powders: The materials used in this research were produced from commercially available HfB_2 and SiC powders. The HfB_2 powders came from two sources at 325-mesh and 99.5% reported purity. The HfB_2 powder for the HfB_2-0% SiC material came from

ABCR, GmbH, while the HfB_2 powder for the SiC-containing materials came from Materion, Corp. The SiC powder was α-phase, 99.9% pure, with particle sizes between 0.03 and 3 μm.

Sintering: The HfB_2 and HfB_2-SiC materials were processed into bulk materials by the Materials and Manufacturing Directorate of the Air Force Research Laboratory. A SiC grinding media in isopropanol was used to pre-mill the HfB_2 powder for 60 hours, resulting in an average particle size of 1.3 μm. Then, the appropriate amount of SiC powder by volume was added, and the mixture milled for 18 hours, followed by stirring, drying at room temperature, and dry milling for another 18 hours. The mixture was sifted through an 80-mesh screen, and 100 g of the mixture loaded into a 40-mm diameter, graphite die coated with boron nitride (BN) and lined with graphite foil. The material was then sintered in a spark plasma sintering unit manufactured by FCT Systeme, GmbH. The heating and cooling rates were 50˚C/min, with a maximum temperature of 2100˚C. Hold times at the maximum temperature were 30 minutes for the HfB_2-0% SiC material and 10 minutes for the SiC-containing materials. A pressure of 40 MPa was held for the duration of heating and sintering, but reduced to 4 MPa for cooling down to 450˚C.

Cutting: Electric discharge machining was used to cut the pucks of sintered material into rectangular parallelepiped test specimens, with two grooves machined on one side for placement of extensometer rods. The nominal dimensions of the specimens (6.5 x 6.5 x 19 mm) were limited by the size of the sintered pucks, which in turn made compressive testing more practical. The dimensions, illustrated in Figure 6, ensured that

the test specimens fit comfortably within the furnace chamber, and that the specimen height suited the gauge length of the extensometer. Specimen edges were not beveled, and post-test observations confirmed that this was acceptable.
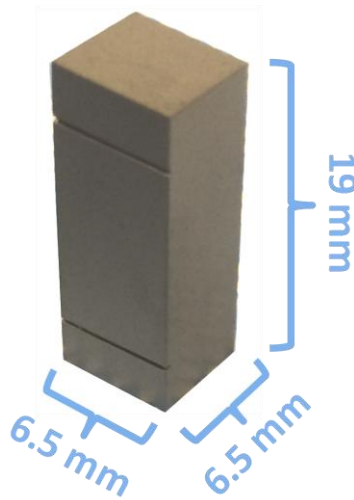
Figure 6: Test Specimen Geometry

Polishing: To remove the surface damage caused by electric discharge machining and establish a consistent finish with minimal surface flaws, all surfaces were polished with diamond slurry to a 45-µm finish. The depth of polishing was determined by sectioning and analyzing two representative, as-machined scraps of material (HfB_2-0% and -20% SiC). Then, scanning electron microscopy (SEM) and energy dispersive x-ray spectroscopy (EDS) were used to determine depths of damage and contamination. In general, cracks near the surfaces of both materials were observed, as well as deposits of copper and zinc, which were assumed to come from the brass wire used in the machining process. The damage and contamination on the HfB_2-20% SiC material was only observed in some locations, while they were observed more regularly on the HfB_2-0%

57

SiC material. Additionally, the damage on the HfB_2-0% SiC material consistently went

to greater depths. It was assumed that differences could be correlated to differences in

the two materials, such as grain size, densification, the presence of SiC, and/or the source

of HfB_2 powder. For all of these factors, there were differences between the pure and

SiC-containing HfB_2, which are detailed in this section. Thus, the polishing depths for

pure and SiC-containing HfB_2 were set at 25 and 100 μm, respectively. Figure 7 includes

sample SEM images that show some of the damage and contamination observed on the

surface of the HfB_2-20% SiC material, following electric discharge machining.
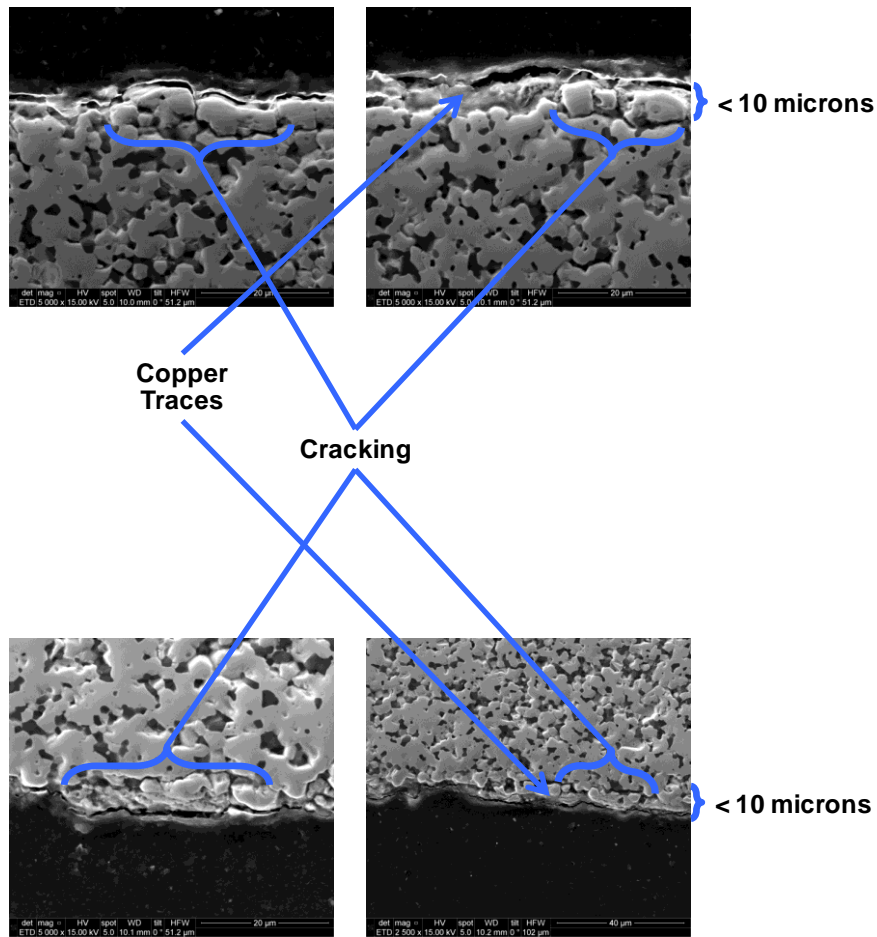
Figure 7: Observed Effects of Electric Discharge Machining on HfB_2-20% SiC

Characterization: The properties of the spark plasma sintered pucks were dependent on the composition of the *Powders* and the variables used in the *Sintering* process. Thus, much care was taken to characterize each material and ensure consistency from puck to puck and specimen to specimen. Characterization primarily included grain size analysis, thermal strain measurements, density measurements, impurities investigations, and microstructural observations. A summary of the findings are presented in Table 4, with additional details found in the following paragraphs and in *Appendices A, B, C, and D*, starting on page 132.

Table 4: Characterization of the Research Materials

Material (HfB_2 -)	Grain Size (μm)	Density (g/cm^3)	Density (% of Theoretical)	Impurities (Top 3 by % Weight)
0% SiC	39.1	10.57	95.0	Zr 0.78%, Fe 0.10%, W 0.05%
10% SiC	5.5	10.31	99.8	Zr 0.18%, Al 0.06%, Fe 0.03%
20% SiC	3.8	9.51	99.7	Zr 0.27%, Al 0.08%, Fe 0.02%
30% SiC	3.3	8.68	99.3	Similar to HfB_2-20% SiC Material

An average grain size was determined for each composition of the research materials (i.e. HfB_2-0%, -10%, -20%, and -30% SiC). This was accomplished on representative scraps of material via Electron Backscatter Diffraction (EBSD) and automated software using the planimetric procedure. The average, pre-test grain sizes, weighted by grain area, were 39.1, 5.5, 3.8, and 3.3 μm, respectively. Differences between the pre- and post-test grain sizes were less than 25% with no preferred

orientations observed. *Appendix A* starting on page 132 includes EBSD images, grain size distributions, and standard deviations for representative scraps of the pre- and post-test materials. Additionally, *Appendix A* includes an analysis that verifies the consistency of the reported grain sizes and compositions throughout a puck of material.

As an added measure to characterize the research materials and ensure integrity, coefficients of thermal expansion were calculated from the thermal strains experienced during the heat up period before each creep test. *Appendix B*, starting on page 139, presents the coefficients, which are consistent with values found in Winder's work and the literature. Coefficients, with units 10^{-6} / °C, ranged from 6 to 10 and averaged 8.

The Archimedes method was used to determine the density of a specimen from each puck and all specimens from some pucks. Helium pycnometry was used on some specimens to validate the technique and agreed within 0.5%. The densities for HfB_2-0%, -10%, -20%, and -30% SiC were 10.57, 10.31, 9.51, and 8.68 g/cm^3, respectively. These densities equate to 95.0, 99.8, 99.7, and 99.3% of the theoretical densities, when using 11.12 (HfB_2) and 3.2 (SiC) g/cm^3 for the densities of the constituent materials as in Gasch's work [51]. More information regarding the measurement techniques and variations in densities is reported in *Appendix C* starting on page 141. The results suggest that the SiC-containing materials attained nearly full densification, but the pure HfB_2 has about 5% porosity. This is less porosity than considered in the example calculation with Equations 6 and 7, starting on page 30, which help to quantify the effects of porosity on creep rates. Thus, the porosity in the pure HfB_2 material is expected to increase creep rates, but less than an order of magnitude. Additionally, the porosity is not expected to affect the present research's analysis of stress exponents, because results are only

60

compared among the same materials, and the appendix shows that only small variations in density occurred from specimen to specimen and puck to puck for the same materials. Otherwise, when applicable, the effects of porosity on the creep rates of the HfB_2-0% SiC materials are addressed in the results and analysis.

Microstructural observations were made in accordance with the *Data Collection* plan, and no irregularities were discovered that are expected to affect the analysis and conclusions of this research. As an example of these observations, SEM images and EDS spectra are provided in Figure 8 of samples from each of the three pucks of HfB_2-20% SiC. The SEM images were consistent throughout the samples and from puck to puck. Oxide scales were not found to exist before testing. SiC grains appeared homogenously dispersed within the SiC-containing materials. EDS spectra appeared similar.
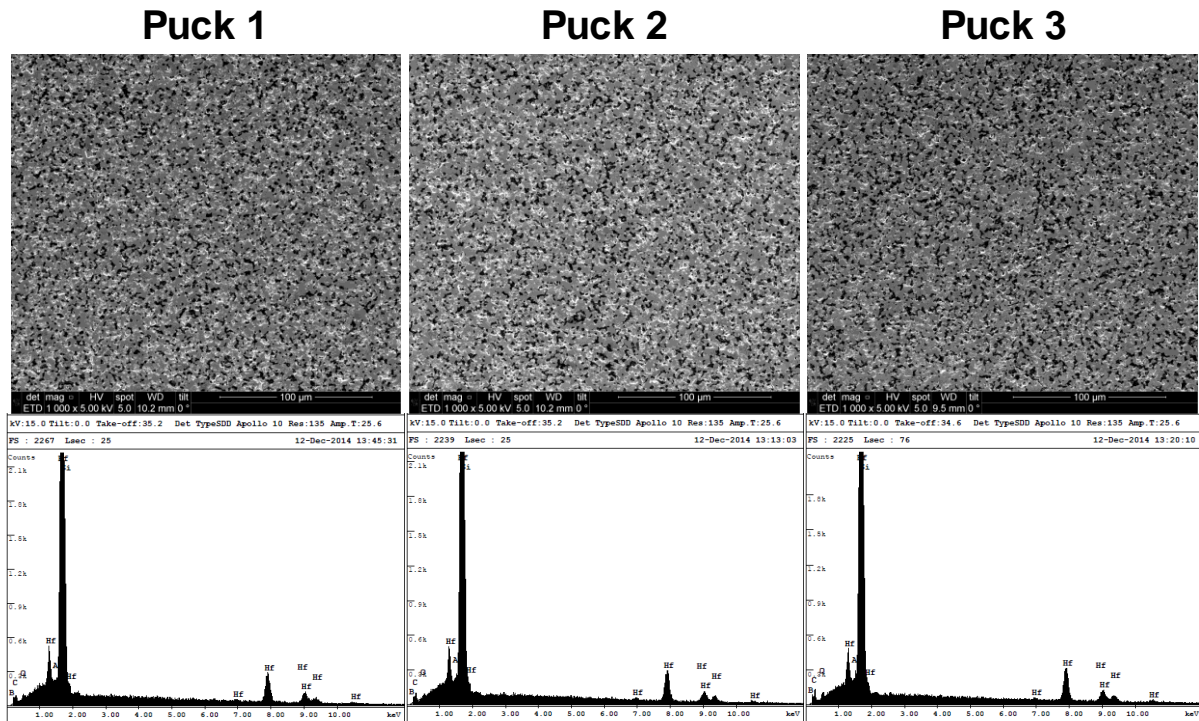
Figure 8: SEM Images and EDS Spectra from HfB_2-20% SiC Pucks

The microstructural observations included two irregularities, but they are not expected to affect the analysis and conclusions of this research. The first was a small number of SiC conglomerations in the HfB_2-30% SiC, whose extent is shown in Figure 44 on page 138, followed by discussion. The second was a small, isolated area of under-sized grains in the HfB_2-0% SiC, possibly caused by an impurity, which is shown in the Figure 9 SEM image. This was the only such area observed, and it was about 100 μm across. Only one specimen came from this particular puck of material, and it was not used in this research. This particular sample received a cursory polishing that was harsher than other efforts, which caused pitting in the surface of the specimen. It is interesting to note that pits do not seem to occur as prominently among the smaller grains.
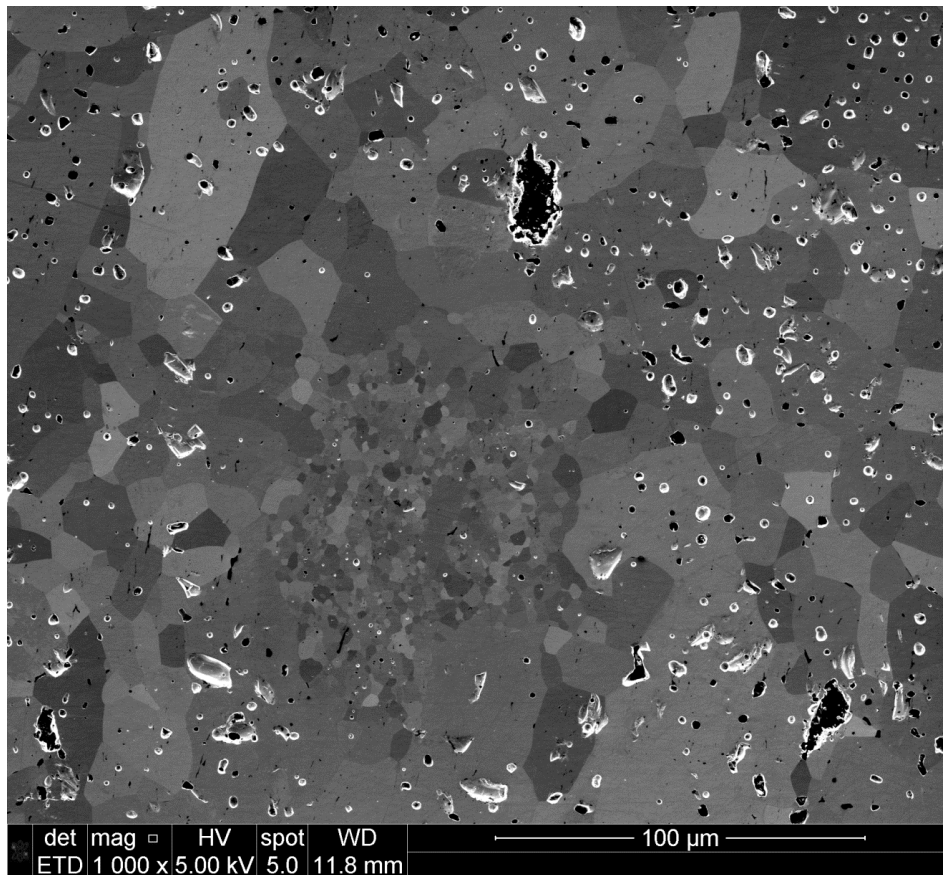
Figure 9: Isolated Area of Small Grains Observed in HfB_2-0% SiC Material

The impurities investigation included three methods: Energy Dispersive X-ray Spectroscopy (EDS), Wavelength Dispersive X-ray Spectroscopy (WDS), and Glow Discharge Mass Spectrometry (GDMS). With respect to the quantification of impurities in the bulk materials, the GDMS method proved most effective. GDMS was performed on pre-test specimens and out-sourced to a disinterested service provider. Table 5 lists all elements detected at greater than 100 ppm weight, plus nickel and copper. GDMS was not performed on the HfB_2-30% SiC material, but its impurities are assumed to be most similar to the HfB_2-20% SiC material, which is generally supported by the EDS and WDS results. The complete results may be found in *Appendix D* starting on page 145, including information on the EDS and WDS results. Discussions of the post-test results are also incorporated into the *Results and Analysis* section.

Table 5: Impurities in the Research Materials (all values in ppm weight)

Element	$HfB_2 - 0\%$ SiC	$HfB_2 - 10\%$ SiC	$HfB_2 - 20\%$ SiC
Al	8	600	810
Ti	120	13	12
Cr	180	18	9
Fe	990	330	180
Ni	40	14	6
Cu	1	30	0
Zr	7800	1800	2700
W	510	4	1
Os	110	1	24
U	120	0	0

Overall, the impurities investigation of the pre-test materials does not show any cause for concern. Zirconium impurity is expected due to its chemical similarity to hafnium, and its low presence of less than 1% by weight is not expected to affect the conclusions of this research with respect to creep or oxidation behavior. Nickel and platinum are added to this discussion, because the *Literature Review* shows them to affect the analysis of creep in transition metal diborides [13], [14]. The quantity of nickel is small and not sufficient to effectively wet grain boundaries and change the measured bulk material properties. Platinum is not included in the previous table, because it was not detected. The GMDS detectable limit for platinum was reported as 10 ppm. Copper traces appear more prevalent in the HfB_2-10% SiC material, which might indicate that more polishing should have been performed in order to completely eliminate the effects of electric discharge machining from the surface. These trace amounts are not expected to affect the results, and post-test observations of the oxide scale did not show any irregularities. The impurities of the HfB_2-0% SiC material appear to distinguish themselves from the HfB_2-10% and -20% SiC materials. This is probably related to the difference in sources from which the HfB_2 powders were obtained. Excluding zirconium, the impurities make up less than 0.3% of the research materials by weight and are considered acceptable for the purposes of this research. Any irregularities in the experimental data and post-test microstructural observations of the research materials are supplemented by EDS to ensure that impurities are not a factor.

3.2 Experimental Arrangements

Setup: The experimental setup follows the previous work of Winder, taking advantage of the painstaking development of a proven procedure that meets the well-known challenges of creep testing ceramics at high temperatures. The experimental setup in Figure 10, developed by Winder and used for compressive creep tests at 1500°C in air, includes a uniaxial load cell, furnace, and extensometer. This setup has many special features, designed to overcome the challenges of creep testing at high temperatures, which are described in the following section on *Equipment*. When setting up these experiments, specimen alignment, surface machining, and temperature accuracy are very important [113]. Alignment jigs assist in alignment, fine diamond grit polishes the surfaces to a consistent 45-μm finish, and calibration tests ensure temperature accuracy.
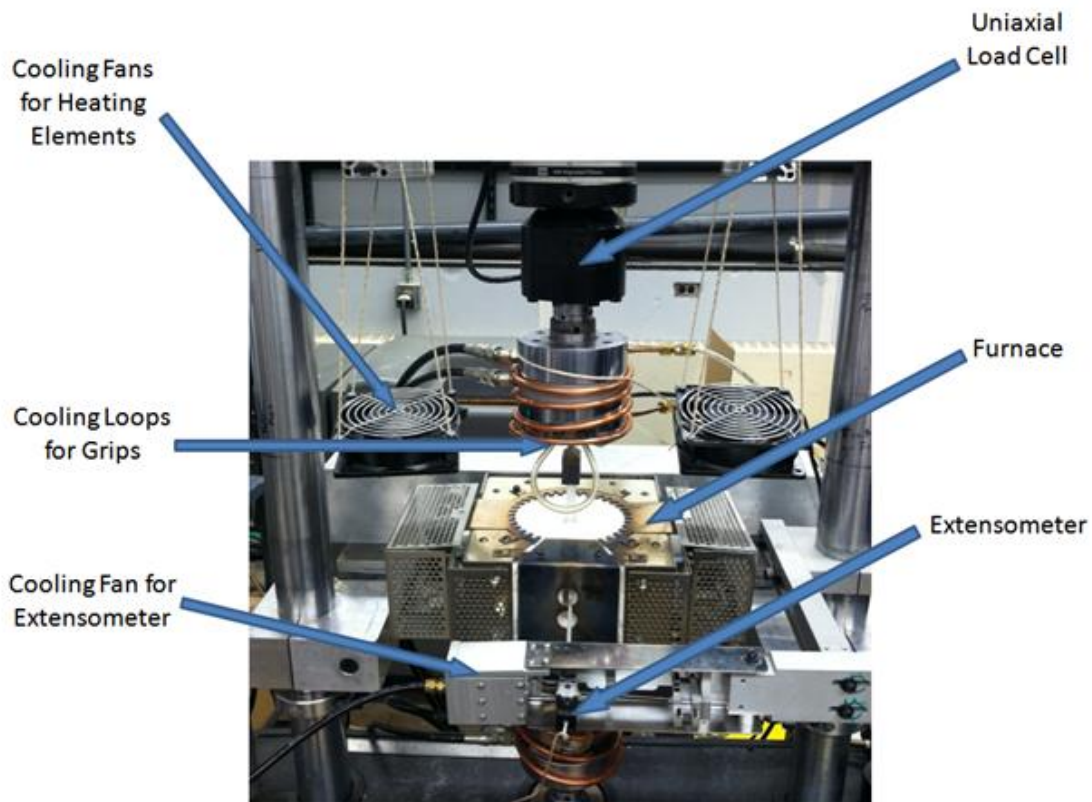
Figure 10: Experimental Setup

As in Winder's work, custom holders are loaded into the grips of the uniaxial load cell and aligned with a solid metal rod. After alignment, the solid metal rod is removed, and two shorter rods are loaded into the custom holders. These rods are made from single crystal yttrium aluminum garnet (YAG), which is known to exhibit excellent creep resistance at the desired test temperatures. Copper spacers are used on the outside ends of the YAG rods (i.e. between the YAG rods and the custom holders) to ensure a more uniform distribution of the load onto the ends of the brittle YAG rods. On the inside ends of the YAG rods, platinum foil and alumina spacers are used between the YAG rods and the HfB$_2$ specimens. The alumina spacers are doubled up to facilitate easy removal of the test specimens after each test, without disturbing the rest of the experimental setup between the grips, shown in Figure 11. The test specimen sits in the middle of the hot zone of the furnace. The extensometer rods are placed in direct contact with the test specimen.
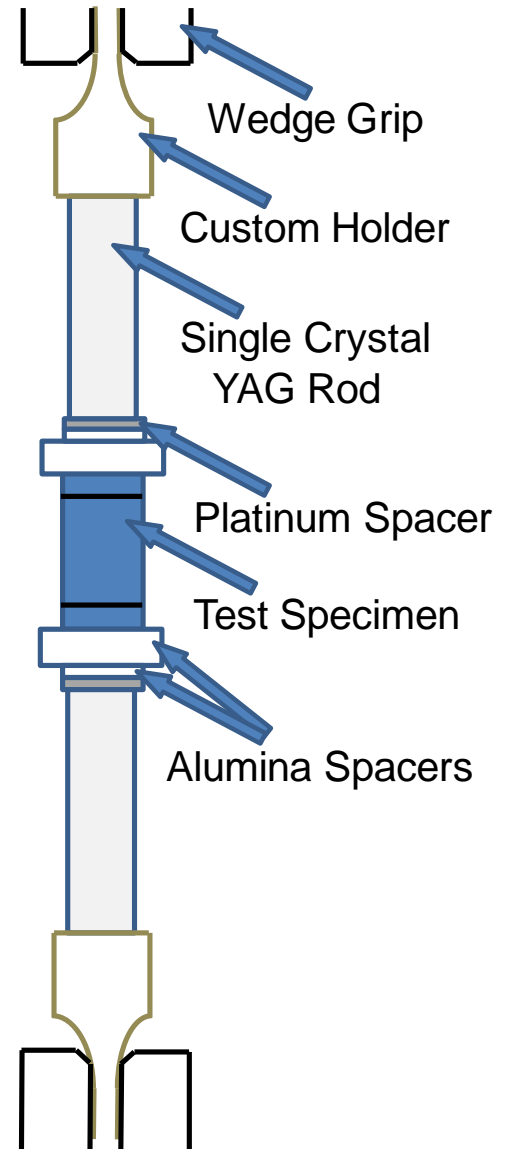
Figure 11: Compressive Creep Test Setup

In order to perform tests in an inert environment, the test setup developed by Winder was modified to incorporate the pumping of an inert gas, argon, into the furnace chamber. At the same time, as much similarity as possible was maintained with Winder's original configuration to facilitate comparison of results.

Although modifications to Winder's setup might seem simple, the high temperature environment made this no simple task. In addition to some new equipment, required modifications included a stable means to flow inert gas into the chamber, recalibration of temperature profiles, and procedural modifications to improve the containment of gases within the chamber and assure reliable performance of the heating elements. This section and 4.1 include descriptions of the work performed to validate the experimental setup.

Equipment: The 810 Test System, manufactured by MTS Systems Corporation, was used in all tests. The testing system had a load capacity of 25 kN and was fitted with the MTS 609 alignment fixture and MTS 661.19E-04 force transducer. The system was controlled by the MTS Flex Test 40 digital controller and Station Manager version 5.2B, which also collected and recorded the data. The wedge grips, MTS 647.02B, were water cooled, using a recirculation chiller, model NESLAB RTE 7, manufactured by Thermo Fisher Scientific. The Station Manager was setup with procedures and displays, as shown in Figure 12, to semi-automatically conduct, monitor, and end creep tests.

Figure 12: Station Manager Displays

The high temperature environment was provided by a single zone, model TD 18 Furnace System MA #100091, manufactured by the MELLEN Company and shown in Figure 13. The furnace was resistance heated by two MD-33 $MoSi_2$ heating elements, had a 31-mm hot zone, and was advertised to be capable of 1700˚C in argon. The furnace had a non-contacting, platinum-rhodium thermocouple, which supplied feedback to the MELLEN PS400 temperature controller. The thermocouple was contained within a yttria stabilized zirconia tube in order to prevent contamination of the test chamber.
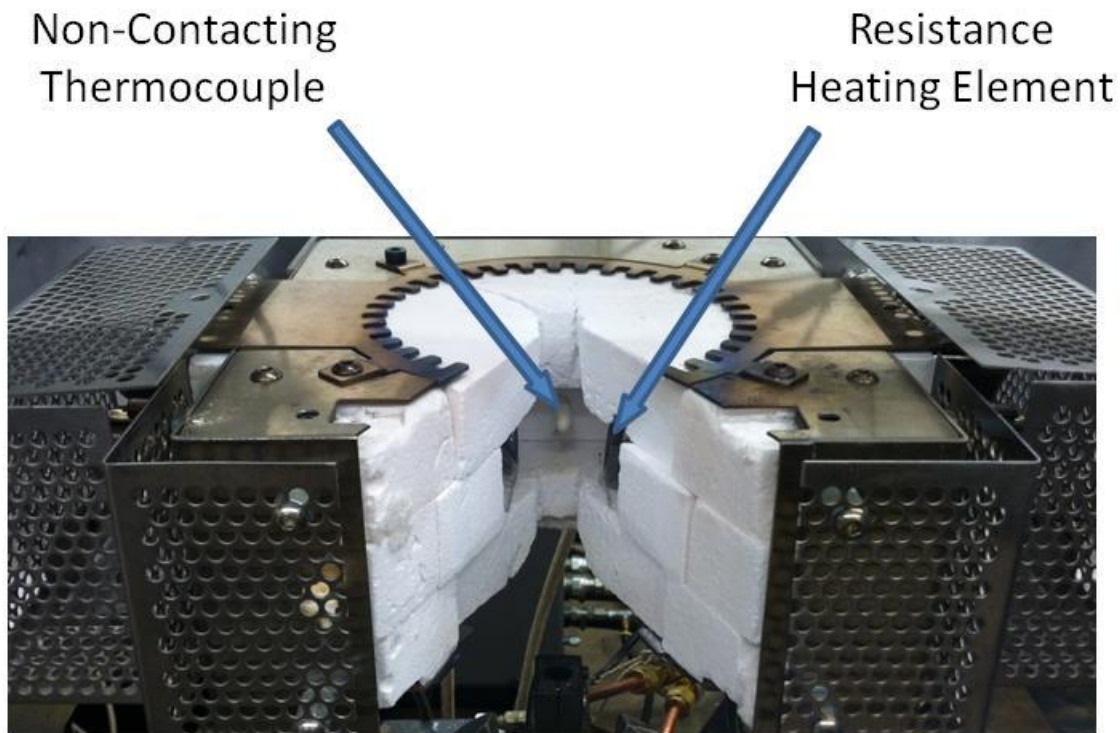
Figure 13: Furnace Interior

Figure 14 shows the modification to the experimental setup, which started by bringing in a high purity argon dewar. Although there was a shelf life due to evaporation of the liquid argon and release of excessive gas pressure buildups, the dewar was selected

for its ability to provide higher flow rates for longer durations than a solitary gas cylinder. The certificates of analysis typically reported 99.999% argon with less than 1 ppm of oxygen. A two-stage, high-purity regulator for argon provided convenient pressure control, through a Swagelok in-line filter, to an Omega FMA-2612-V2 gas mass flow controller, which was configured for argon. The flow controller was not calibrated, but performed the desired function of providing consistent gas flow, which made experiments easily repeatable with good results, following a series of preliminary oxidation and temperature validations to determine the best settings. The output of the flow controller was split and sent to two alumina tubes, which fed the argon into the furnace above and below the extensometer. The furnace was tightly wrapped with foil-backed alumina insulation to help keep air out and better-maintain the required temperatures.
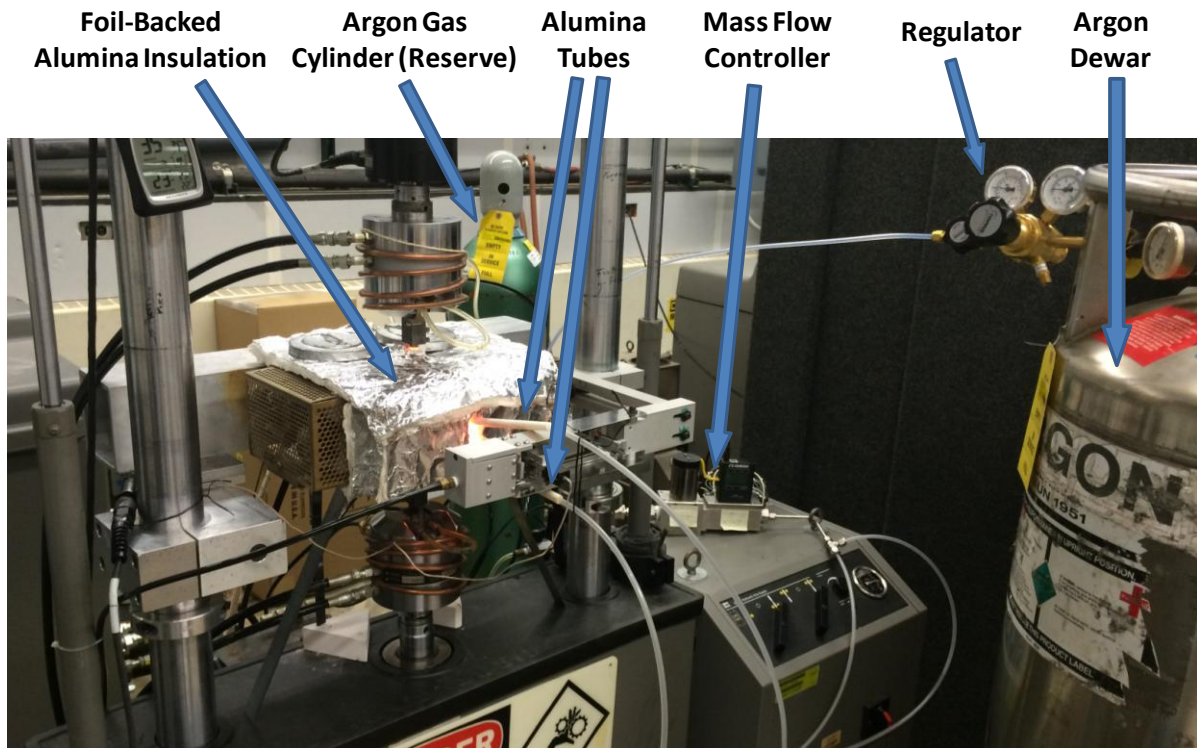
Figure 14: Experimental Setup Modified for Testing in Argon

Procedures: Preliminary procedures were used prior to the actual creep tests and focused on calibration, verification, and validation of the experimental setup. This was achieved by running over a dozen tests at elevated temperatures, but no loads greater than 5 MPa. Scraps of the research materials were often used, although the final validations were performed with specimen-sized scraps of material. The primary goals of these tests included:

1. Establish consistent and effective procedures for conducting tests in argon

2. Validate appropriate and consistent flow of inert gas

3. Calibrate the furnace's thermocouple

4. Validate acceptable inertness of the environment

The preliminary tests achieved all of the primary goals with the following notes. First, the preliminary tests served to work out the difficulties of conducting the creep tests, which were not trivial under such extreme conditions, and optimization of the furnace's insulation. Thus, the specific procedures evolved throughout the preliminary tests, until reaching the validation tests, which confirmed that consistent and effective procedures for conducting tests in argon had been established. Extra care was taken to validate typical requirements, such as alignment of the uniaxial load cell, reliable extensometer measurements, and effective abort procedures. The final procedures are reviewed in the following paragraph and detailed in *Appendix E* starting on page 152. Second, some of the preliminary tests included variations of the inert gas flow to observe the effects on specimen oxidation and furnace temperatures, which determined the

optimal settings. Third, the furnace's non-contacting thermocouple was calibrated with other B-type thermocouples, which were used to determine temperature profiles, both around and in contact with specimen-sized scraps, at various temperature settings. Fourth, the final validation of the inertness of the environment is reported in section 4.1, which starts on page 79.

Appendix E, starting on page 152, provides the specific procedures used to conduct the creep tests in this research effort. These procedures focus on uniaxial, compressive creep tests in argon at elevated temperatures. Also, these procedures were generally used to conduct the stressed oxidation tests, which are described in more detail in section 4.6 starting on page 112. The creep and stressed oxidation tests were conducted at constant loads and temperature, with the actual values remaining within +/- 5 N and +/- 10°C of the commanded values, respectively. Heat up and cool down were generally conducted at 20°C per second. Creep tests were conducted for each of the four research materials (i.e. HfB_2-0%, -10%, -20%, and -30% SiC) at 25, 50, and 75 MPa and 1500°C in argon. Creep tests with HfB_2-0% and -20% SiC at 50 MPa and 1500˚C should enable good comparisons with results obtained by Winder in air. The primary goals of the creep tests include:

1. Determine creep as a function of time

2. Determine the secondary creep rate and creep life, if applicable

3. Observe changes to the microstructure

Other procedures are discussed in other sections of this document, including procedures for observing changes to the microstructure. For example, procedures for measuring oxide scale thicknesses are discussed on page 77, determining grain sizes on page 132, and investigating for impurities on page 145. Procedures for determining the minimum creep rate, and whether steady state creep was achieved, are found starting on page 155.   Procedures for the baseline oxidation tests are covered starting on page 164.

3.3 Data Collection

Parameters: The following parameters were included in the data collection plan, in order to capture the proper information needed to complete the *Research Objectives*.

1. Composition, grain size, and density of the bulk materials

2. Pre- and post-test specimen weight and dimensions

3. Pre- and post-test microstructural observations

4. Test load, temperature, and strain as a function of time

Instrumentation and Calibration: The following paragraphs describe the instrumentation and calibration utilized to ensure the collection and accuracy of data for the load, temperature, and strain parameters. Data for all three of these parameters were fed into the MTS digital controller and recorded by the MTS Station Manager on a computer at 1 Hz. Test time was recorded by the Station Manager from an internal clock.

The load was determined from an MTS 661.19E-04 force transducer, which was attached below the alignment fixture. According to the manufacturer specifications, this force transducer has a repeatability of about 7.5 N, a compensated temperature range of -18 to +66˚C, and a useable temperature range of -54 to +93˚C. The sensitivity of the force transducer is affected by about 0.5 N/˚C.

The temperature was determined from a B-type, non-contacting thermocouple inside the furnace chamber. The signal was sent through the temperature controller and digital controller to the MTS Station Manager. The temperature commanded by the Station Manager was determined by a calibration described in the *Procedures*, where the

73

commanded temperature and the temperature sensed by the non-contacting thermocouple were calibrated to the temperature measured by a contacting B-type thermocouple on a representative test specimen.

The strain was determined from a MTS 632.53E-14, high temperature, low contact force extensometer, shown in Figure 15, which provided a signal from direct contact with the test specimen. The extensometer has a gauge length of 12.7 mm and, with air cooling and a heat shield, a maximum use temperature of about 1204˚C. However, the alumina extensometer rods were replaced with sapphire rods that have a maximum use temperature of about 1800˚C. The rest of the extensometer was outside of the furnace, and experienced acceptable operating temperatures within the manufacturer's recommended limitations, which were periodically monitored with an optical pyrometer.
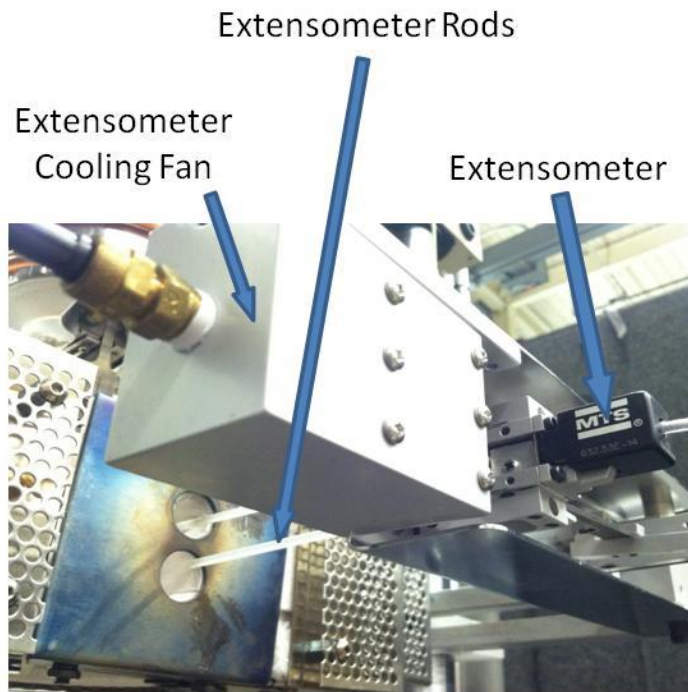
Figure 15: Extensometer

74

Specimen weight and density were determined using a calibrated scale and the Archimedes method. The Archimedes method was facilitated by a universal specific gravity kit, shown in *Appendix C* on page 144, and a thermometer. A calibrated micrometer and the optical microscope described in the following section were used to measure test specimen dimensions. As needed, an EDS, as described in the following section, was used to perform compositional analysis of the microstructure.

Microstructural Observations: Several different devices were used to make microstructural observations. However, examples of the most typically utilized devices are presented in the following paragraphs.

Simple observations and measurements of relatively large features on specimens were conducted with the Zeiss SteREO Discovery.V12 optical microscope, shown in Figure 16, at the Air Force Institute of Technology. This device offered 5 to 150X magnification.
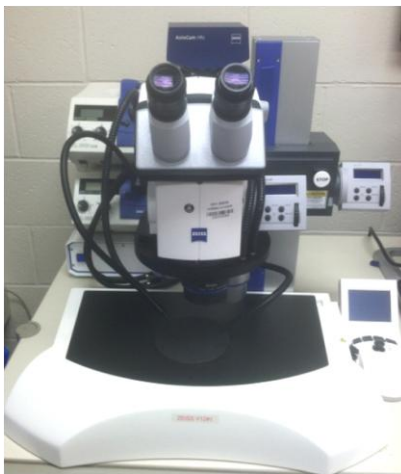
Figure 16: Zeiss SteREO Discovery.V12 Optical Microscope

Microstructural observations were made with the FEI Quanta 600 and Philips XL-30 FEG at the Materials and Manufacturing Directorate of the Air Force Research Laboratory, shown in Figure 17 and Figure 18, respectively. These setups included SEM, EDS, and EBSD capabilities, and provided this research effort with 20 to 80,000X magnification, up to 2 nm resolution, and detection of elements from boron to americium (Z=5 to 95) on the periodic table.

Figure 17: FEI Quanta 600 SEM with EDS and EBSD Capabilities

Figure 18: Philips XL30 FEG SEM with EDS and EBSD Capabilities

When microstructural observations required oxide scale thickness measurements, the total thickness was measured (i.e. including the glass, metal oxide, and SiC-depleted regions, whenever present). Unless otherwise specified, this research reports only these

total values and refers to them as "oxide scale thickness". Such measurements do not imply that all three regions are present. To the contrary, this research only observed SiC-depleted regions in the preliminary oxidation tests at temperatures above 1500°C. In order to consistently and accurately determine oxide scale thicknesses, several techniques were employed and cross checked with each other, shown in Figure 19, and then averaged among many measurements, typically 60 or more per specimen. It was noted that SiC-depleted regions appeared darker than SiC with the Everhart-Thornley Detector (ETD). EDS mapping was used to identify where the signal corresponding to oxygen fell off to background levels in the metal diboride. Under a Back Scattered Electron Detector (BSED), the metal oxide appeared darker than the metal diboride. If the electron power was turned up sufficiently, the oxide layer started to charge and returned more signal.
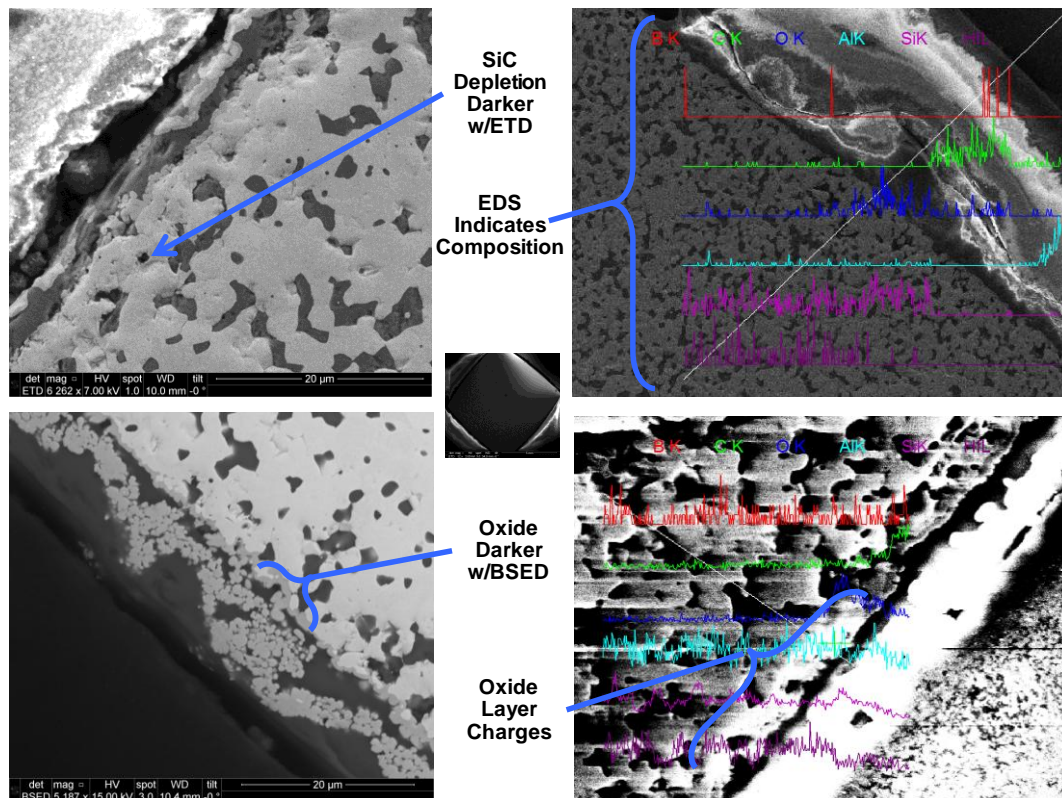
Figure 19: Techniques Used to Determine Oxide Scale Thickness

3.4 Summary of Assumptions

Most of the assumptions in this research arise in the analysis of the results. For example, reporting of minimum creep rates involved assumptions regarding the definition of the steady state or secondary creep region and the calculation of the rate, which is covered in *Appendix F* starting on page 155. Calculation of exponents with respect to the general creep equation assumed creep behavior followed an exponential function.

As far as assumptions pertaining to the experiments, there were relatively few. Proper and periodic calibration, verification, and validation made assumptions regarding the data minor. Long periods of data collection provided substantial opportunity to identify random noise and outlying data. The selection of uniaxial creep tests, with an extensometer in direct contact with the specimens, avoided some of the assumptions found in other works regarding strain. However, some mentionable assumptions regarding the experiments still exist. First, engineering stress was used in this effort, so changes in the cross sectional areas of the specimens were neglected, although pre- and post-test geometrical measurements ensured this assumption remained reasonable. Thus, stress calculations were based on the pre-test, unstressed cross sectional areas. Second, calibrations were assumed valid within the range of conditions experienced in the controlled laboratory environment. Third, deviations in oxidation rates during creep tests in argon were assumed small, compared to rates painstakingly determined during the preliminary tests. These levels are discussed in the following section, and the experimental setup, including argon source and flow, were maintained consistently among creep tests. Finally, these experiments are expected to be comparable to Winder's experiments, given the similarities of the experimental setup, materials, and procedures.

IV. Results and Analysis

This section presents the results of the experiments described in the *Methodology* section and then provides a thorough analysis as it relates to the creep and oxidation of UHTCs. More detailed information may be found in the *Appendix*.

4.1 Validation of the Experimental Facility

Results: The measures of effectiveness selected for the experimental facility include the duration of testing and the amount of oxidation. Ideally, the experimental facility would sustain the desired temperature and stress for as long as it takes to identify the minimum creep rate and maintain a perfectly inert environment that allows no oxidation. Realistically, failure of any of the materials used in the compressive load train might bring a premature end to the creep tests, and some minimal amount of oxidation will probably occur in the argon environment due to imperfections in the experimental setup, such as openings in the furnace to accommodate instrumentation, oxygen impurities in the argon, and out gassing of oxygen from furnace components. Considering the exploratory nature of these tests, assuming the ideal would be naïve and possibly lead to results that are out of context. For example, creep tests that are too short, might not provide a good look at the minimum creep rate, and tests that allow high rates of oxidation might make it difficult to separate the creep rate of the material under test from the effects of oxidation. Thus, presenting results, which demonstrate a) the setup can function without failure for a sufficiently long duration and b) the oxidation of the

test specimen is fully or nearly eliminated in the argon environment, provides important measures of effectiveness for the experimental facility.

Table 6 shows the durations for all creep tests conducted, along with the compressive stress levels and reasons that the tests ended. Creep duration was defined as the amount of time at the specified temperature and stress. Spacer failure refers to the alumina spacers shown in Figure 11 on page 66, and run out refers to intentionally ending a creep test because sufficient data from the secondary creep regime had been collected. Creep tests conducted at 25 MPa generally had the longest durations. The creep test for specimen H10-1 ended due to a power failure unrelated to the experiment. All creep tests conducted at stresses of 50 MPa and above ended suddenly due to spacer failure.

Table 6: Experimental Facility Measures of Effectiveness (Duration of Testing)

Specimen	Material HfB$_2$ -	Environ- ment	Temp (°C)	Compressive Creep Stress (MPa)	Creep Test Duration (h)	Reason for Test Ending
H00-1	0% SiC	Argon	1500	25	17.5	Run Out
H00-4	0% SiC	Argon	1500	50	3.6	Spacer Failure
H00-5	0% SiC	Argon	1500	75	1.3	Spacer Failure
H10-1	10% SiC	Argon	1500	25	12.0	Power Failure
H10-2	10% SiC	Argon	1500	50	4.1	Spacer Failure
H10-3	10% SiC	Argon	1500	75	0.5	Spacer Failure
H20-2	20% SiC	Argon	1500	25	16.0	Run Out
H20-3	20% SiC	Argon	1500	50	5.3	Spacer Failure
H20-1	20% SiC	Argon	1500	75	3.0	Spacer Failure
H30-5	30% SiC	Argon	1500	25	15.5	Run Out
H30-6	30% SiC	Argon	1500	50	3.5	Spacer Failure
H30-4	30% SiC	Argon	1500	75	0.3	Spacer Failure

Figure 20 shows a correlation between the compressive creep stress and creep test duration. Generally, the area to the bottom-left of the data points would be testable by the experimental facility in its present configuration.
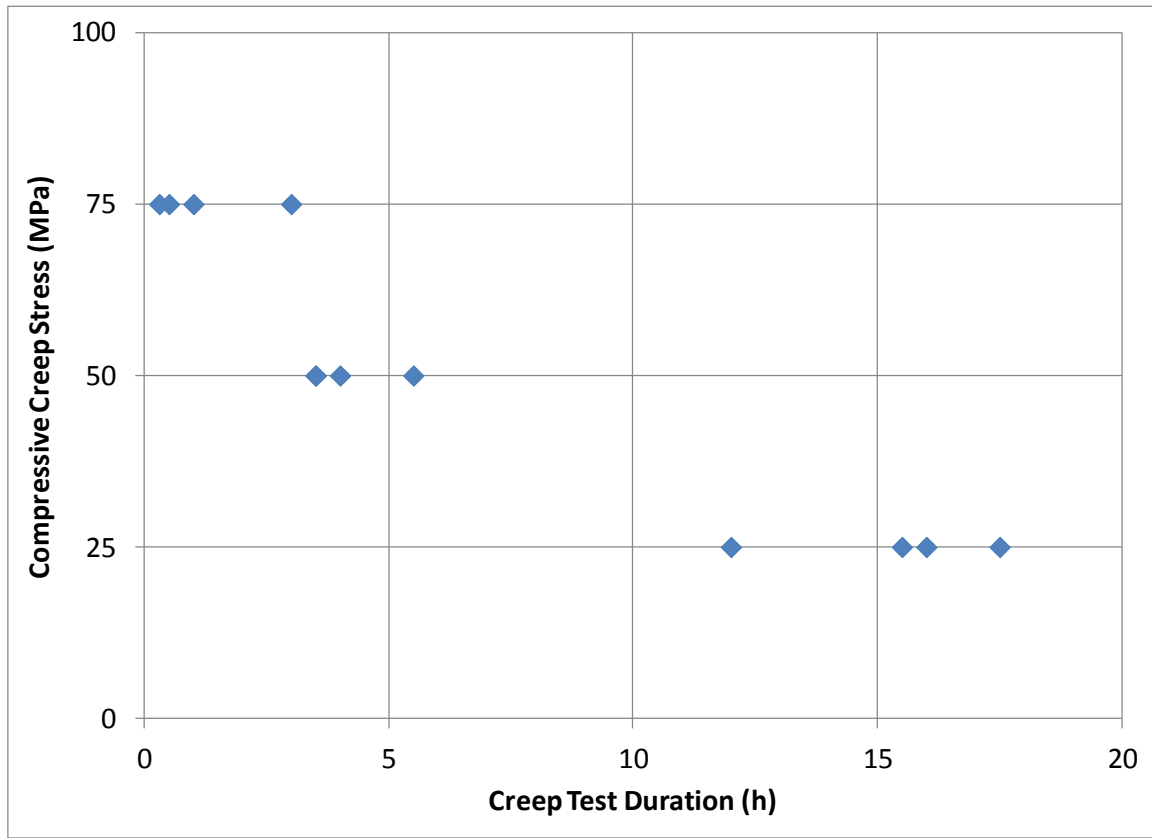
Figure 20: Compressive Creep Stress vs Creep Test Duration at 1500°C in Argon

Table 7 quantifies the amount of oxidation observed following four preliminary tests in the experimental facility's argon environment, assumed due to the previously discussed imperfections in the experimental setup. The oxide scale thicknesses were determined by sectioning the specimens after the tests and examining the sections using the SEM and EDS techniques described in the *Data Collection* section. The preliminary

81

test with the specimen designated as OT8 included temperature calibration procedures up to 1530°C. This was the only specimen from the preliminary tests that exhibited a region with a layer of SiC-depleted material. For this specimen, the average oxide scale thicknesses for regions with and without SiC-depletion were calculated separately and labeled active and passive, respectively.

Table 7: Experimental Facility Measures of Effectiveness (Amount of Oxidation)

Specimen	Material HfB$_2$ -	Argon Source	Argon Flow	Temp (°C)	Duration (h)	Average Oxide Scale Thickness in Argon (µm)
OT7	20% SiC	Gas Cylinder	1 SLPM	1500	9	9
OT8	20% SiC	Gas Cylinder	1 SLPM	1400-1530	5	8 (passive) 47 (active)
OT9	0% SiC	Gas Cylinder	1 SLPM	1500	10	97
OT10	0% SiC	Liquid Dewar	5 SLPM	1500	10	110

Analysis: Overall, the duration of testing and amount of oxidation, in conjunction with the data collected, indicate that the experimental facility was effective enough to meet the objectives of this research. However, redesigns of the experimental facility need to occur in order to collect data at higher stresses, at higher temperatures, and/or for longer durations in an inert environment, thus making further gains in our knowledge of the creep behavior of these material systems possible.

The experimental facility was not as effective as desired in terms of duration of testing, as will be discussed further in the following section. Although the experimental

facility could achieve run out at 25 MPa, this stress level was so low that precise measurements of minimum creep rates were difficult, characterized by low signal-to-noise ratios, and requiring longer test durations. Thus, tests at higher stresses were desired, but then alumina spacer failures continually shortened test durations as stress levels increased. This caused added work in terms of assessing whether sufficient data had been collected in the secondary creep regime and, if not, re-accomplishment of creep tests. At times, an objective method was helpful in determining whether a secondary creep rate had been observed. In the course of this research, the chosen method involved using a nonlinear, least-squares fit of Burger's model. A further discussion and example are provided in *Appendix F: Nonlinear Least Squares Fit of Burger's Model*, starting on page 155. Spacer failures also commonly caused Winder's tests to end suddenly [13], although her tests appear to have slightly longer durations on average. Two factors that might have caused a difference in creep test durations include the testing environment (i.e. argon versus air) and different batches of alumina spacers. Tai et al. report that grain growth and grain boundary etching near the surface, when alumina is heated above 1500°C in argon, can reduce flexural strength and create fracture origins [114]. The effects were greater when water vapor was added to the environment. The alumina also became whiter after heating in argon, which was also observed in this work. Some ideas for improving the creep test durations of future experiments include microstructural investigations of the spacers, reducing water vapor if applicable, only using two spacers instead of four, and, probably most conveniently, switching to a different material for the spacers such as sapphire. Reducing the rate of heat up, finely polishing the surfaces, and rounding all of the edges appeared to have no observable effect on spacer life at these

conditions. Overall, despite these obstacles, the durations of testing were sufficient enough to meet the objectives of the present research.

In terms of the amount of oxidation, the experimental facility performed admirably, especially considering the constraint of maintaining similarity to the methods developed by Winder for testing in air. Since the furnace was essentially built around the mechanical loading system, with additional openings for an extensometer, heating elements, and thermocouples, sealing off the experimental facility to air was difficult and imperfect. The argon flow was used as best as possible to maintain a positive pressure inside the furnace chamber to keep air out. However, out gassing from the porous alumina furnace and insulation was probably the primary source of oxygen, because further increases in argon flow did not seem to increase or decrease oxidation rates. Oxygen impurities in the source gas could not account for the amount of oxidation experienced. Unfortunately, the test chamber was too small to introduce oxygen barriers or scavengers without interfering with the mechanisms of heating, loading, and extensometry developed by Winder. Given those obstacles, it is quite amazing that, based on the results of the preliminary tests, the experimental facility should only be expected to result in an oxide scale thickness of about 10 μm for the HfB_2-20% SiC material and 100 μm for the HfB_2-0% SiC material after 10 hours at 1500°C. Given the size of the specimens, this means at the end of a 10 hour test at 1500°C, the cross-sections of the specimens should be expected to be composed of about 0.5% oxidized scale for the HfB_2-20% SiC material and 5% oxidized scale for the HfB_2-0% SiC material. This degree of oxidation is tolerable in meeting the objectives of this research, because the oxide scale should be expected to comprise a small portion of the cross

section and provide an order of magnitude contrast to the oxidation rates experienced in air. Strain rate correction factors are discussed on page 110.

Table 8 compares oxidation results obtained in this research with those reported in literature at 1500°C in terms of environment, material composition, time at temperature, and oxide scale thickness. Due to the scarcity of this data for HfB_2 materials at these specific conditions, data from tests conducted in air as part of this research were also included (reference *Appendix H* starting on page 164). The final column of Table 8 assumes parabolic oxidation kinetics and normalizes the data by squaring the oxide scale thickness and dividing by the time at temperature. This normalized data is referred to as the parabolic rate constant and illustrates the effectiveness of the experimental facility in terms of the amount of oxidation.

Table 8: Comparison of Oxidation Results to Literature at 1500°C

Lead Author	Ref.	Environ-ment	Material	Time (h)	Oxide Scale Thickness (μm)	Parabolic Rate Constant (cm^2/s)
DeGregoria		Argon	HfB_2-20% SiC	9	9	2.50E-11
Winder	[13]	Air	HfB_2-20% SiC	18	42	2.72E-10
Carney	[42]	Air	HfB_2-20% SiC	1	20	1.11E-09
DeGregoria		Air	HfB_2-20% SiC	.5-90	17-160	1.31E-09
Carney	[42]	Air	HfB_2-20% SiC	0.1	7	2.04E-09
Bargeron	[115]	55 torr O_2	HfB_2-0% SiC	0.5	18	1.80E-09
DeGregoria		Argon	HfB_2-0% SiC	10	104	3.00E-09
DeGregoria		Air	HfB_2-0% SiC	.5-6	88-504	7.95E-08
Winder	[13]	Air	HfB_2-0% SiC	18	830	1.06E-07

Table 8 shows that the experimental facility, modified with an argon gas flow, was effective at reducing the parabolic rate constant for both the HfB_2-0% and -20% SiC materials by over an order of magnitude. In comparison to Bargeron's work, the experimental facility, ignoring all other experimental factors, appears slightly shy of the reported effects of a 55 torr O_2 environment. It is difficult to compare this research's amount of oxidation to the work of other researchers, specifically those who performed creep tests of similar materials, because the amount of oxidation is often unreported in literature. No post-test amounts of oxidation or discussion of this issue could be found for the inert creep experiments listed in Table 1 on page 7, except for the work of Gangireddy et al. After a 75-second creep test of ZrB_2-30% SiC at 50 MPa and 2000°C in a 0.25% O_2 environment, Gangireddy reported a 5-μm, SiC-depleted layer of ZrB_2 on the surface. This layer was about 1.5% of the specimen's thickness and assumed not to affect creep [15]. Though not often discussed, these experiences speak to the difficulties of performing creep tests at these extreme conditions in an inert environment. For the purposes of this research, the amount of oxidation that occurred in the inert experiments is acceptable and assumed on par with the experimental capabilities reported in contemporary literature. The effects of the amount of oxidation that occurred in the inert experiments are further analyzed and discussed in section 4.5, which starts on page 107.

Further improvements to the inertness of experimental facility's environment are not expected to come from increasing the flow rate of the argon gas, reducing the impurities in the argon gas, or closing holes in the furnace. This is based on the preliminary tests, which unsuccessfully attempted the previously mentioned tactics with little to no effect. This points to other areas as the driving source of oxygen

contamination, such as the alumina furnace itself. Some ideas for further reducing the expected amount of oxidation, given the experimental setup, include the addition of graphite to act as an oxygen scavenger or replacing some of the furnace components with graphite materials. This, of course, would be no small endeavor given the small size of the furnace test chamber and possibly require a rebuild of the furnace. Otherwise, a conceptual redesign of the experimental facility would probably be required to make worthwhile gains in inertness, which would deviate from this research's objective of maintaining similarity to Winder's results in air.

Finally, it should be noted for future research that regions with layers of SiC-depleted material were observed in the scale of the OT8 specimen. As part of a temperature calibration, this specimen experienced the highest temperatures of this research effort, up to 1530°C. Regions of SiC-depleted material in HfB_2 and ZrB_2 have been reported in the literature at higher temperatures and described as evidence of the active oxidation of SiC. However, Shugart shows that lowering the partial pressure of oxygen can lower the temperature at which the oxidation of SiC transitions from passive to active [116]. Thus, given the flow of argon gas used in the present research's creep experiments, transition from passive to active oxidation of SiC should have been expected at temperatures lower than reported in the literature for HfB_2 in air. Shugart also shows that compositions with more SiC also transition to active oxidation at lower temperatures, and longer times at these temperatures result in larger SiC-depleted regions. In the present research, the experimental facility and test conditions appear to have closely avoided the transition to active oxidation, which could have accelerated oxidation rates and decreased the load bearing capability of the materials under test.

4.2 Effect of Compressive Stress on the Creep of HfB$_2$-SiC in Argon

Results: Compressive creep tests were performed at 1500°C in argon at 25, 50, and 75 MPa for each of the following materials: HfB$_2$-0%, -10%, -20%, and -30% SiC. Table 9 provides a summary of the results.

Table 9: Compressive Creep Results for HfB$_2$-SiC Specimens at 1500°C in Argon

Specimen	Material HfB$_2$ -	Creep Stress (MPa)	Creep Duration (h)	Creep Strain (%)	Minimum Creep Rate (10^{-8} sec^{-1})
H00-1	0% SiC	25	3.3	0.08	1.59
H00-4	0% SiC	50	3.6	0.12	2.55
H00-5	0% SiC	75	1.3	0.02	9.31
H10-1	10% SiC	25	2.1	2.8	303
H10-2	10% SiC	50	4.1	8.1	336
H10-3	10% SiC	75	0.5	0.97	489
H20-2	20% SiC	25	16.0	0.15	4.50
H20-3	20% SiC	50	5.3	0.39	14.9
H20-1	20% SiC	75	3.0	0.22	30.9
H30-5	30% SiC	25	15.5	0.15	0.46
H30-6	30% SiC	50	3.5	0.01	6.95
H30-4	30% SiC	75	0.3	0.03	13.4

Due to an abnormality in the creep data for specimen H10-1, the results were only reported for the first 2 hours, which only included primary creep. A sudden step change in the strain rate and noise, 2 hours into the creep test, suggested a problem with the extensometer rods. No root cause for the anomaly was identified, but the rods were replaced, and the anomaly did not recur. Data from the last 14 hours of the creep test of

specimen H00-1 were rejected for apparent impingement of the extensometer, which was not recognized during the test. These two tests were among the first tests performed and speak to the difficulty of conducting creep experiments at these conditions.

Figure 21 shows a representative creep curve from one of the tests; specifically, the raw data collected at 1 Hz for specimen H20-3, along with a smoothed curve that uses a moving average. Two disturbances of the extensometer can be seen. Such disturbances sometimes occurred due to interference with other parts of the tightly fitting experimental setup, which could often be quickly corrected.
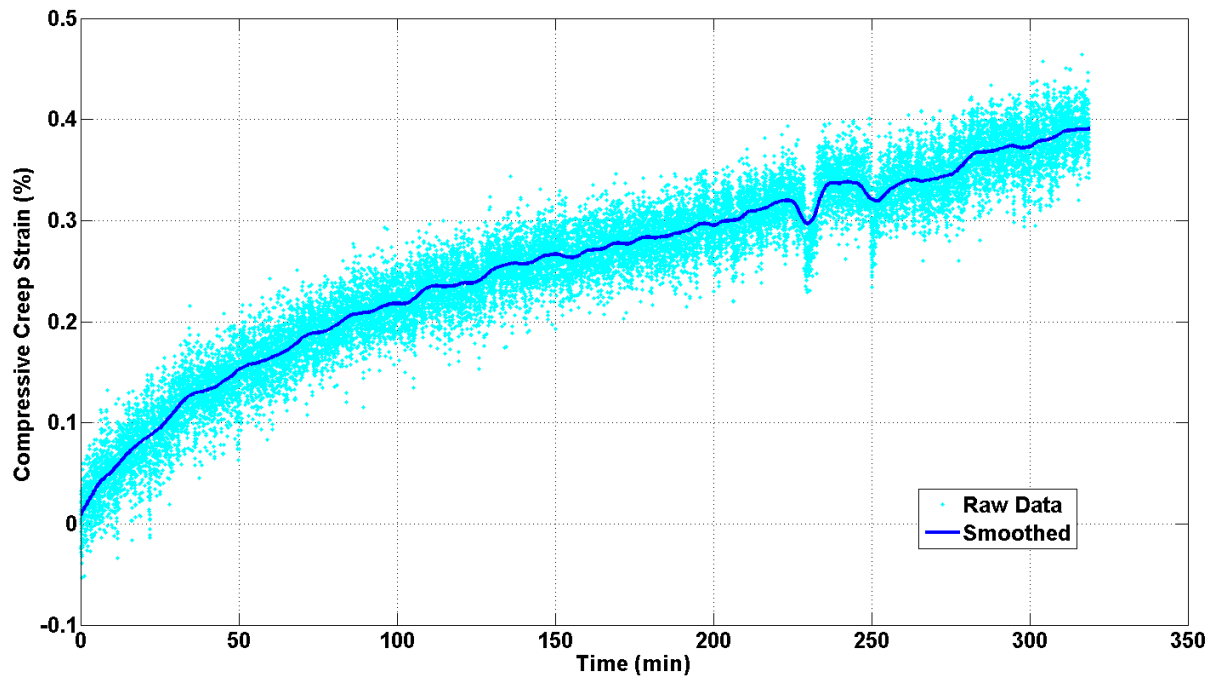
**Figure 21: Creep Strain vs Time
for HfB$_2$-20% SiC at 50 MPa and 1500°C in Argon**

Although different methods of analyzing creep mechanisms exist and different regions of creep curves might be important depending on the application, this research has chosen to analyze creep mechanisms by primarily examining steady state creep rates. This is the method most commonly used in the literature. The methods described in *Appendix F* starting on page 155 were often used to objectively identify whether steady state creep rates were achieved and which data should be used in calculations, so that the minimum creep rates reported in Table 9 are the best reflections of the secondary creep rates. In the case of the data from the creep test of specimen H20-3, shown in Figure 21, primary and secondary creep regions were clearly identifiable. The last approximately 2 hours of data were selected for calculation of the minimum creep rate, with the data from the two disturbances of the extensometer removed. In the case of the three creep tests of the HfB_2-10% SiC material, secondary creep regions could not be identified. The HfB_2-10% SiC material clearly exhibited the longest primary creep region in terms of time and strain, and testing in the experimental facility was unable to clearly capture secondary creep data. Thus, the minimum creep rates presented in Table 9 on page 88 for the HfB_2-10% SiC material are not intended to reflect the secondary creep rates. However, primary creep regions were sufficiently short for the other materials, such that the experimental facility was able to capture data from the secondary creep region. This interesting result, regarding the considerable variation in the length of the primary creep region with respect to SiC content, is analyzed in the following section on the effect of SiC additives. The accuracy of the methods used to determine minimum creep rates is also discussed in *Appendix F*.

Analysis: To illustrate the effect of compressive stress on minimum creep rate,

Figure 22 uses a log-log plot of the results with a least squares, power law regression in

accordance with Equation 1.   The regression indicates that the stress exponents, n, for the

HfB_2-0%, -10%, -20%, and -30% SiC materials were 1.5, 1.0, 1.8, and 1.4, respectively.

Figure 27 on page 104 shows the results normalized to a grain size of 1 μm.
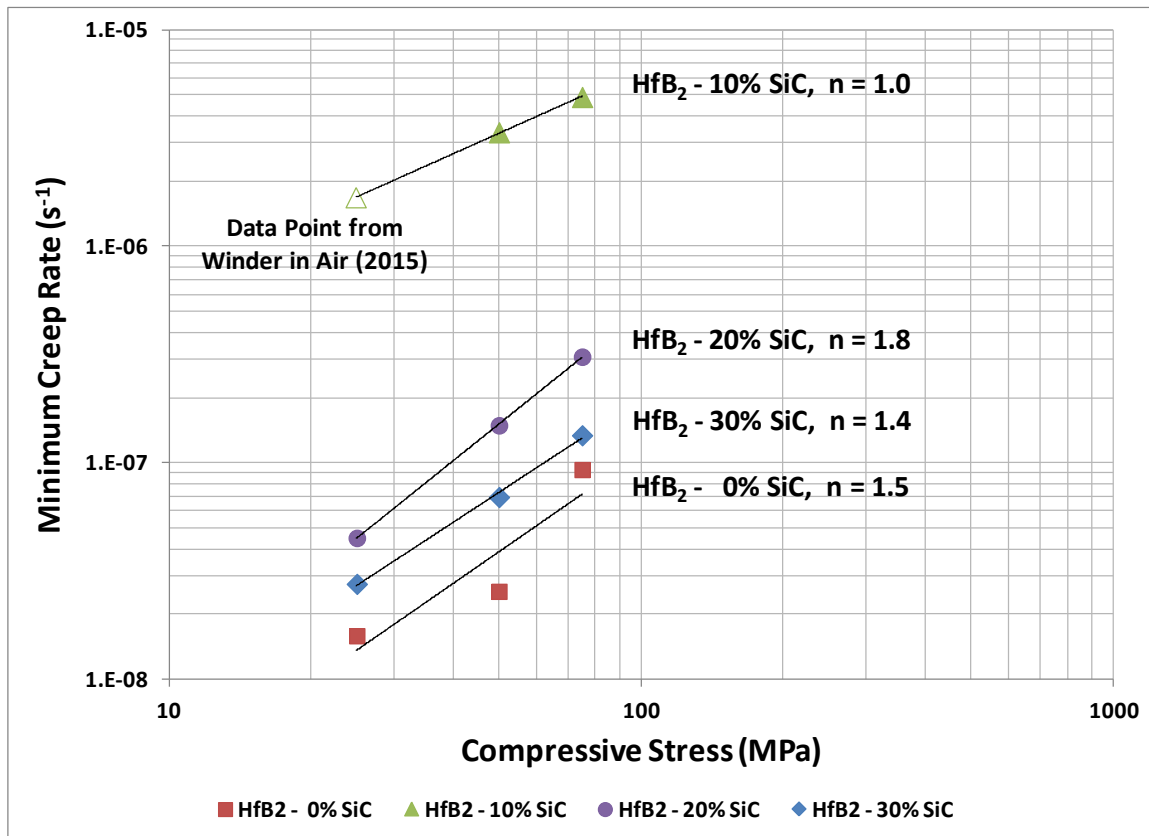
Figure 22: Minimum Creep Rate vs Compressive Stress
for HfB$_2$ -0%, -10%, -20%, and -30% SiC at 1500°C in Argon
Data Point for HfB$_2$-10% SiC at 25 MPa from Winder in Air [13]

The data point for HfB_2-10% SiC at 25 MPa comes from Winder's work [13].

Although Winder's tests were performed in air, it fills a void in the present research's

results, due to the previously discussed abnormality in the data. A later section pertaining

to the effects of oxidation on creep addresses the validity of including this data point from a test in air with tests in argon, specifically the strain rate correction factors in Table 12 on page 110. The constitutive model in *Appendix F* starting on page 155, applied to the 2 hours of good data from this research, implies a minimum creep rate of 120×10^{-8} s^{-1}, only slightly lower than the data point from Winder at 168×10^{-8} s^{-1}. The HfB$_2$-10% SiC material used in Winder's and this research's work came from the same puck of material.

Table 3 on page 27 suggests that stress exponents in the range of 1 to 2 indicate that boundary mechanisms dominated creep rates. These results are consistent with the creep mechanisms and stress exponents reported in the literature for HfB$_2$ and ZrB$_2$. Winder's stress exponents for HfB$_2$-0% and -20% SiC in air ranged from 1.7 to 2.3. Gangireddy reported 1.4 for ZrB$_2$-30% SiC in an inert environment, 1700-2000°C. Bird reported a transition from 1 to 1.7-2.2 between 1500 and 1600°C for ZrB$_2$-20% SiC in an inert environment. In air, Talmy reported 0.7-1.0 for ZrB$_2$ with 25% SiC or less and 2.5 for ZrB$_2$-50% SiC. Finally, Melendez-Martinez reported 1.7 for ZrB$_2$ in an inert environment, with transitions at higher temperatures and stresses. The most commonly cited controlling creep mechanism in these works was grain boundary sliding accommodated by diffusion. Thus, the results are consistent with the literature, but additional information, some of which is provided in the following sections, is needed in order to identify which specific boundary mechanism might be dominating the creep rates at these conditions, including any types of diffusion. Transitions of the dominant creep mechanism with stress and temperature are not apparent in the present research, which is expected, considering the limited range of temperatures and stresses. However, the following section proposes a transition in creep resistance with respect to SiC content.

4.3 Effect of SiC Additives on the Creep of HfB$_2$-SiC in Argon

Results: As described in the previous section, compressive creep tests were performed at 1500°C in argon at 25, 50, and 75 MPa for each of the following materials: HfB$_2$-0%, -10%, -20%, and -30% SiC. Please reference Table 9 and Figure 22 in the previous section for the results.

Analysis: The resulting data strongly suggest that the HfB$_2$-0% SiC material has the lowest minimum creep rate. Upon the addition of 10% SiC, the minimum creep rate appears to increase by two orders of magnitude. This is consistent with the literature, which generally associates an increase in SiC content with an increase in creep rate, due to smaller grain sizes and sliding of SiC grains [17]. However, the addition of more SiC to 20% and 30% appears to progressively decrease the minimum creep rates. This does not fit with the previous logic, because further increases in SiC content are expected to further decrease grain sizes (which was shown to have occurred in this research in the *Methodology* section) and/or further increase (or at least maintain) the same effects on grain boundary sliding. Since the minimum creep rates decreased, this suggests another factor, which is addressed in the following paragraph. For now, it might be helpful to look at the creep results with SiC content on the abscissa. Since there is at least one unknown factor in play, as well as other non-linear factors reported in the literature, the data is simply presented in Figure 23 as a scatter plot with no trend-lines.
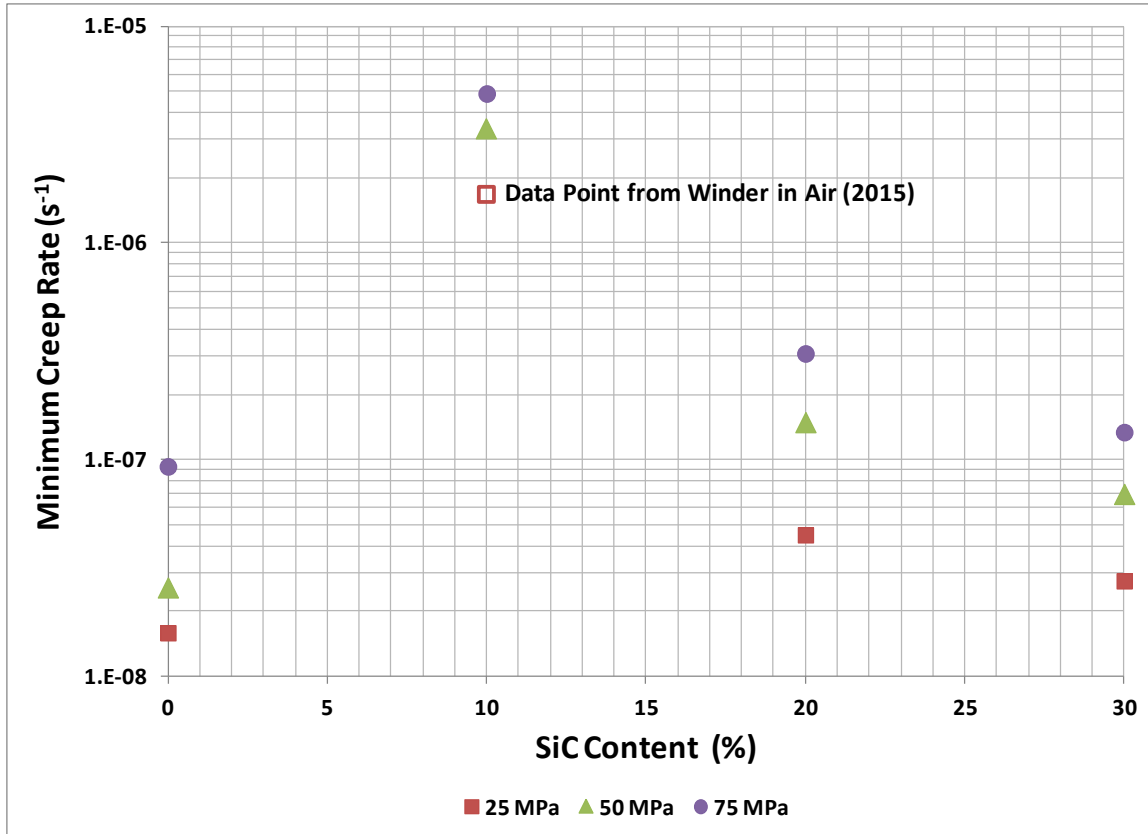
**Figure 23: Minimum Creep Rate vs SiC Content
for HfB$_2$ at 25, 50, and 75 MPa and 1500°C in Argon
Data Point for HfB$_2$-10% SiC at 25 MPa from Winder in Air** [13]

We know that the unknown factor appears to decrease minimum creep rates with increasing SiC content. One possible explanation is that the minimum creep rate is being more and more influenced by the mechanical properties of SiC as SiC content increases. After all, the well-known creep rates of SiC at these conditions appear an order of magnitude less than the creep rates reported for pure HfB$_2$ in this research and in Winder's research. Thus, it makes sense that more SiC might decrease creep rates, especially since we should expect SiC to drive the creep behavior by the time we reach 90 and 100% SiC. Under this proposition, one might consider the rule of mixtures as a

94

method for approximating the effect. An alternative method might be to assume there exists a hypothetical distance between SiC grains, where SiC starts to dominate the creep behavior. In low SiC-containing HfB_2 materials that have SiC grains separated by more than this distance, there might even exist a transition period that separates early-on creep behavior and post-transition creep behavior, after the SiC grains fully interact. Wilkinson describes such a phenomenon in terms of a percolative network with volume fraction as the critical variable [102]. Addressing creep in multiphase ceramics, Wilkinson proposes two percolations. The first occurs when the harder phase of independently acting particles develops a network of point-to-point contacts, thus decreasing creep rates. Wilkinson suggests that whisker additions to ceramic matrices can decrease creep rates by 2 orders of magnitude and also cites a theoretical, critical volume fraction of 16% [117], decreasing for increasing aspect ratios and arguably aligning with the experimental data in Figure 23. The second percolation occurs when the network of point-to-point contacts transitions into a network of facet-to-facet contacts. Wilkinson cites a critical volume fraction of 64% as one example, but reminds us that critical volume fractions are a function of particle morphology and preferred orientation. Wilkinson's framework appears to explain how increasing SiC content might decrease creep rates in this research.

A closer look at the creep test results from the SiC-containing HfB_2 materials in this research supports this proposal, as well as other results found in the literature. For the HfB_2-10% SiC material in this research, the creep strains are relatively high and the primary creep regimes appear to last for at least several hours. In fact, the previously described method for objectively determining whether a steady creep rate was reached (also described in *Appendix F* starting on page 155) indicates that a steady creep rate

95

might not have been reached in all three of the HfB_2-10% SiC creep tests. However, with

the HfB_2-0%, -20%, and -30% materials, the creep strains are much lower and the

primary creep regimes much shorter. Table 9 provides the relevant data, and Figure 24

shows a comparison of creep versus time for HfB_2-10 % and -20% SiC at 50 MPa in

argon. *Appendix F*, starting on page 155, provides a closer look at these two plots.
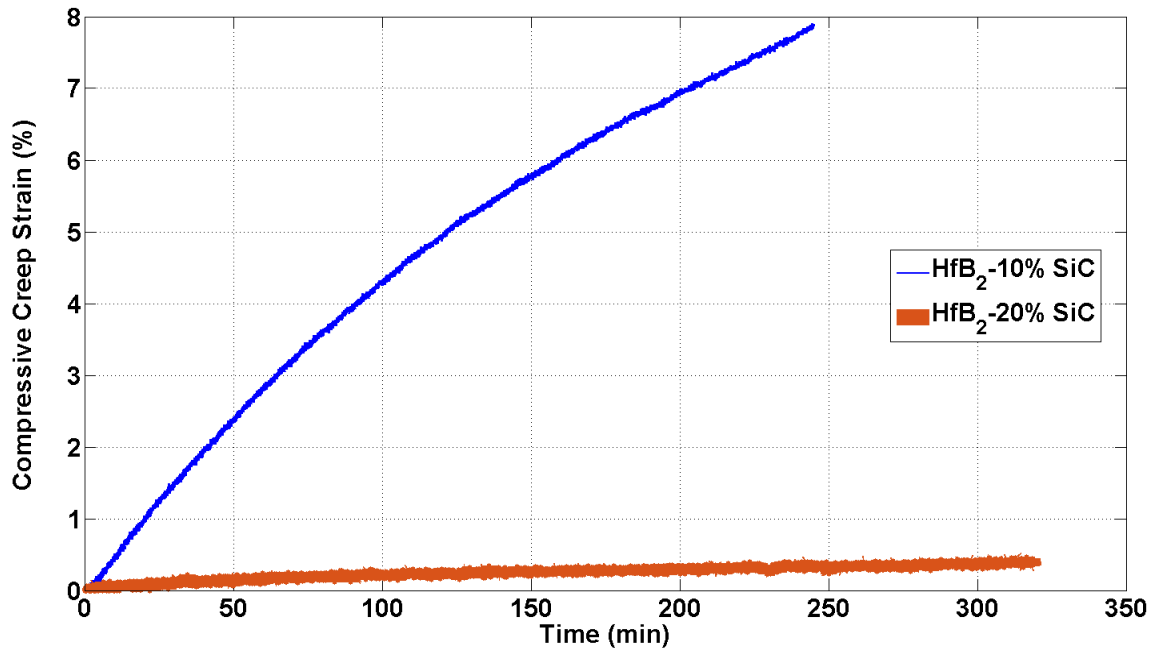
Figure 24: Creep Strain vs Time
for HfB_2-10% (top) and -20% (bottom) SiC at 50 MPa and 1500°C in Argon

Notice the accumulated creep strain is over an order of magnitude higher for

HfB_2-10% SiC, compared to HfB_2-20% SiC at the same conditions, and primary creep

for HfB_2-10% SiC has a much longer duration. Why would only the HfB_2-10% SiC

material take so long, in terms of time and strain, to reach a steady creep rate? We know

it is not grain size or the effects of SiC content on grain boundary sliding, because we

have data on either side of both issues that take less time and strain to reach a minimum

creep rate. We also ruled out impurities and grain size changes in the *Methodology*.

However, in light of the previously proposed explanation, it could be that the HfB_2-10% SiC material requires more compressive strain to occur before the SiC percolates into a point-to-point network. In the case of this research, over 8% strain was experienced without reaching a steady creep rate. Wilkinson points out that the development of a network likely occurs gradually. With the HfB_2-20% and -30% SiC materials, the SiC grains could already be close enough to form a point-to-point network, or achieve it with such little time and strain that it might simply be recognized as part of primary creep. Looking at the figures in *Appendix A* on page 133, one could imagine how it would take a lot of strain for the SiC (i.e. dark) grains in the HfB_2-10% SiC material to come together and form a point-to-point network, but the SiC grains in the HfB_2-20% and -30% SiC materials might already be close enough. Keep in mind Wilkinson's observation that networked particles do not necessarily need to touch, in order to form a network, due to stress gradients. In future studies, it might be beneficial to determine how much strain is required for the SiC in the HfB_2-10% SiC material to work through the first percolation and develop, if ever, a network equivalent to HfB_2-20% SiC.

What is clearly understood from the literature is that the addition of some SiC to HfB_2 increases creep rates, which has been primarily attributed to its effects on grain size. Results of this research propose the idea that there exist combinations of SiC content and strain where SiC decreases creep rates. The curve in Figure 25 illustrates the synthesis of these two ideas, where creep rates start off at a value for pure HfB_2, increase when small amounts of SiC are added, then decrease as SiC grains gradually form a network, and eventually reach a value for SiC. Finding the true magnitude and SiC content of the peak

and its width might prove difficult for secondary creep rates, because large strains and/or transitioning through percolations of networks might be required to obtain secondary creep rates for low SiC-containing HfB_2 materials. Figure 25 does not portray the second percolation described by Wilkinson. However, the point is made that SiC at lower levels increases HfB_2 creep rates by reducing gain sizes and possibly affecting grain boundaries. At higher levels, this research has also shown that SiC decreases HfB_2 creep rates.
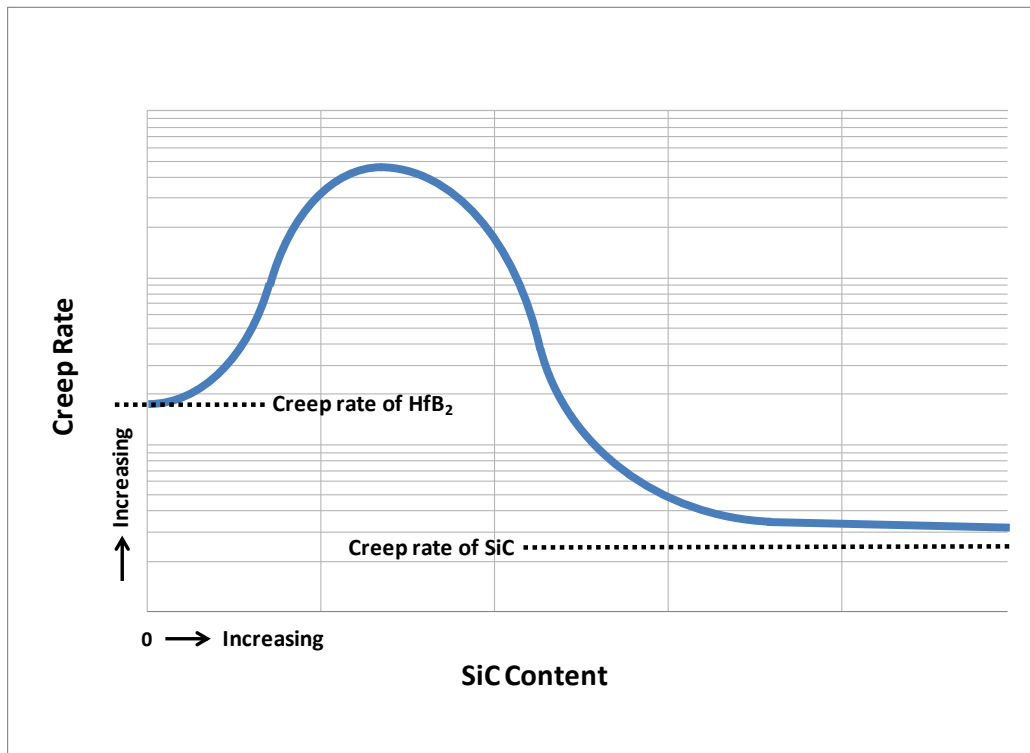
Figure 25: Creep Rate vs SiC Content
(Postulated Trend-line for HfB_2 at Constant Stress and Temperature)

For the lowest SiC-containing HfB_2 material investigated in this research (HfB_2-10% SiC), the experimental setup was unable to sustain the required creep durations at 50 MPa and above in order to reach secondary creep. Additionally, at 25 MPa, an unexplained abnormality in the strain data and a power failure that prematurely ended the

creep test prevented the determination of a secondary creep rate. If the secondary creep rates were not obtained for the HfB_2-10% SiC material, then the peak in Figure 23 could be lower than perceived. Alternatively, if the peak actually occurs at a SiC content between those selected in this research, then the peak could be higher than perceived. In order to obtain better data and construct a curve like Figure 25, creep tests would need to be performed for a more refined selection of SiC-containing HfB_2 materials with low SiC contents (e.g. 5%, 7.5%, 10%, 12.5%, and 15% SiC). Also, creep tests would need to be performed for longer durations at the higher stress levels, and the extensometer's signal-to-noise ratio would need to be decreased at the lower stress levels. For these efforts, new materials would need to be procured, and the experimental setup would need to be further improved or modified to meet these needs. This would be a worthwhile endeavor, because characterizing the magnitude and width of the peak in Figure 25 is important for aerospace applications. Some applications would not appreciate it, if a small variation in SiC content unexpectedly resulted in a large increase in creep rates. For now, it is reassuring to see that an SiC content of 20%, often identified in the literature as being good for oxidation resistance, appears to benefit from lower creep rates in Figure 23. However, the formation of a SiC network that increases creep resistance would probably proceed differently or not at all in tension, implying a difference in creep behaviors.

Finally, Talmy's work with ZrB_2 suggests a lower stress exponent for lower SiC contents. Results of this research might seem to agree, if only looking at stress exponents for HfB_2-10% (n=1.0) and -20% (n=1.8) SiC in Figure 22 on page 91. However, such a correlation is risky for this research, given the limited data and previous discussions regarding the difficulty obtaining secondary creep rates for the HfB_2-10% SiC material.

4.4 Effect of Grain Size on the Creep of HfB$_2$-SiC in Argon

Results: The near order of magnitude difference in the grain size of the pure HfB$_2$ material, compared to the other three materials containing SiC, presents an opportunity to look at the results from the perspective of grain size effects. Although grain size was an uncontrolled variable in this research, this perspective could aid in the identification of controlling creep mechanisms. For convenience, Table 10 gathers some of the relevant data already presented.

**Table 10: Grain Sizes and Compressive Creep Results
for HfB$_2$-SiC Specimens at 1500°C in Argon**

Specimen	Material HfB$_2$ -	Grain Size (µm)	Creep Stress (MPa)	Minimum Creep Rate (10^{-8} sec^{-1})
H00-1	0% SiC	39.12	25	1.59
H00-4	0% SiC	39.12	50	2.55
H00-5	0% SiC	39.12	75	9.31
H10-1	10% SiC	5.48	25	-
H10-2	10% SiC	5.48	50	336
H10-3	10% SiC	5.48	75	489
H20-2	20% SiC	3.78	25	4.50
H20-3	20% SiC	3.78	50	14.9
H20-1	20% SiC	3.78	75	30.9
H30-5	30% SiC	3.28	25	0.46
H30-6	30% SiC	3.28	50	6.95
H30-4	30% SiC	3.28	75	13.4

Analysis: Any analysis of grain size effects in this research must include the effects of SiC content, because each difference in grain size among the materials is also accompanied by a difference in SiC content. However, it is interesting to note that the HfB_2-0% SiC material had an average grain size of about 39 μm, while the -10, -20, and -30% materials had average grain sizes between 3 and 6 μm. Undoubtedly, this near order of magnitude difference in grain sizes between the pure and SiC-containing materials should have an exponential effect on the creep rate as shown in Equation 1 on page 26. But how can we separate the effects of grain size from SiC content? One method might be to assume that grain size effects dominate sometimes and SiC content other times. This would be a reasonable assumption, considering Figure 26.
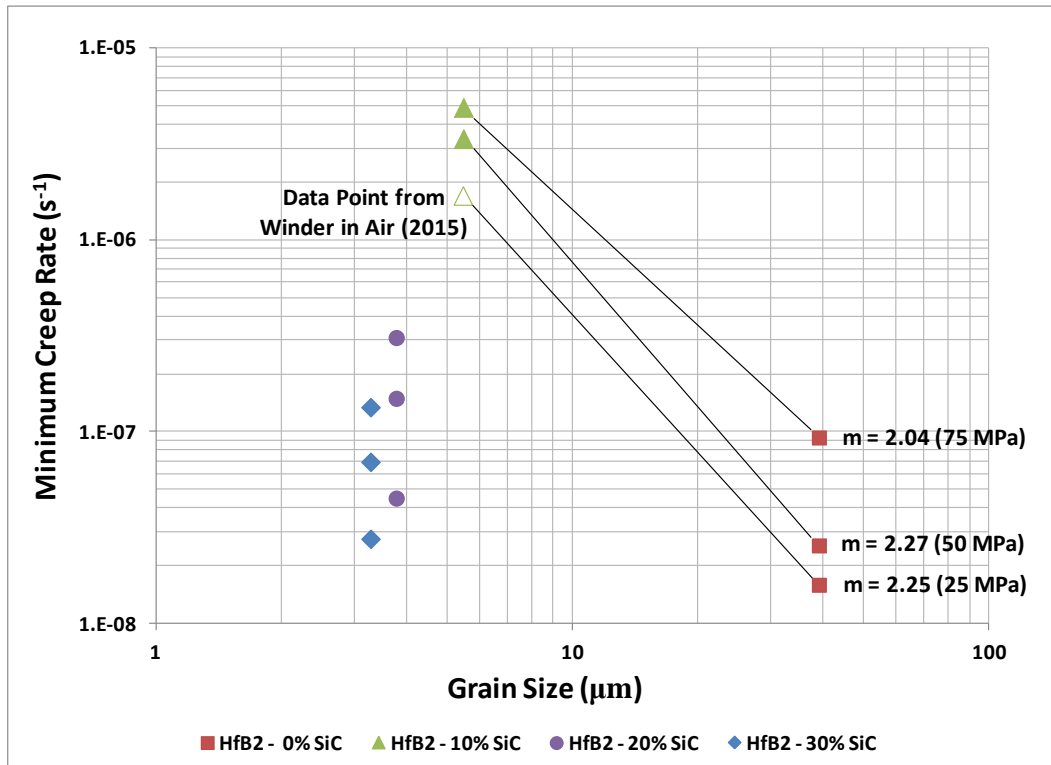

Figure 26: Minimum Creep Rate vs Grain Size
for HfB₂-SiC Specimens at 25, 50, and 75 MPa and 1500°C in Argon
Data Point for HfB₂-10% SiC at 25 MPa from Winder in Air [13]

101

Figure 26 clearly shows an increasing trend in the creep rate from the HfB_2-30% SiC material to the -20% and -10% materials. Of course, the grain size also increases, but it is generally accepted that an increasing grain size should decrease creep rates. Alternatively, Figure 26 shows a clear decrease in creep rate from HfB_2-10% SiC to the -0% material. Thus, we might deduce that grain size effects are dominating the difference in creep rates at the lower SiC contents, but not the higher. However, we must also recognize that some effect of SiC content probably remains present in this comparison. The literature generally relates increases in SiC content to increases in creep rates for these materials at these conditions. We must also keep in mind the previously discussed suspicion that the HfB_2-10% SiC materials did not reach steady creep rates and the effects of 5% porosity on the creep rates of HfB_2-0% SiC. So how can we decouple grain size and SiC content and solve for these two effects simultaneously? Unfortunately, based on previous discussions, we expect the effect of SiC content to be non-linear. Even if we could model the effect for some values of SiC content (e.g. 10%, 20%, and 30%), that model should probably not be used at other values of SiC content (e.g. 0% and 10%) to decouple the effects of SiC content from grain size.

However, if an assumption is made that the effect of SiC content between the HfB_2-0% and -10% SiC materials is small compared to the effect of grain size, then an approximation of the grain size exponent might be found. While there are several factors to discourage such an assumption, not the least of which include the effects of SiC on creep and oxidation, there are some mitigating factors that make it tenable. First, microstructural observations show that SiC in the -10% material forms into grains that appear clearly disconnected. Thus, interactions between SiC grains should not affect the

results. Second, the use of argon decreases the difference in oxidation rates between the -0% and -10% materials and its effects on creep rates. In both cases, the effects are far from eliminated, but should be considered reduced and arguably less than the grain size effect. Finally, we must assume the HfB_2-10% SiC creep rates are near steady state and that the effect of the HfB_2-0% SiC porosity is small, or that the two effects are of a relatively similar magnitude. Proceeding with the assumptions and applying Equation 13 to the creep rates obtained for the HfB_2-0% and -10% SiC materials at 25, 50, and 75 MPa, we arrive at grain size exponents, m, of 2.25, 2.27, and 2.04, respectively. The closeness of these values could support an argument that the previous assumptions were valid. Thus, assuming the HfB_2-10% SiC minimum creep rates are indeed close to the secondary creep rates, then there are six data points in Figure 26 on page 101 that suggest the grain size exponent is near 2.

The key assumption in conducting this grain size analysis was that either the change in grain size or SiC content dominates the difference in creep rates between two HfB_2 materials with different SiC contents. Thus, it is important to go full circle by looking back at the previous sections of the analysis (i.e. the effects of compressive stress and SiC content) in light of the observed effects of grain size. To accomplish this, the minimum creep rates were normalized to a grain size of 1 μm using Equation 31, which was also employed by Armani [118] and Winder [13]. Based on the grain size analysis conducted in this section, the gain size exponent, m, was set at 2.

$$\dot{\varepsilon}_{normalized} = \dot{\varepsilon} \left(\frac{d}{d_{normalized}} \right)^m \qquad\qquad (31)$$

103

Using the minimum creep rates normalized to a grain size of 1 μm, the Minimum Creep Rate versus Compressive Stress figure was recreated. Thus, Figure 27 effectively re-presents Figure 22, but with the effects of grain size removed.

**Figure 27: Normalized Minimum Creep Rate vs Compressive Stress
for HfB$_2$ at 25, 50, and 75 MPa and 1500°C in Argon
Data Point for HfB$_2$-10% SiC at 25 MPa from Winder in Air** [13]

Figure 27 appears to confirm the assumption that the effects of grain size dominated over SiC content when comparing the HfB$_2$-0% and -10% SiC materials, because their data points are very close (i.e. relative to Figure 22) now that the effects of grain size have been removed. However, the data points for the -20% and -30% materials remain relatively different, compared to each other and compared to the -0% and -10% materials,

suggesting that the effects of grain size do not account for a lot of the differences in minimum creep rates at 20% and 30% SiC content. The normalized minimum creep rates were also used to recreate the figure that showed Minimum Creep Rate versus SiC Content (Figure 23), which effectively removes the effects of grain size in Figure 28.
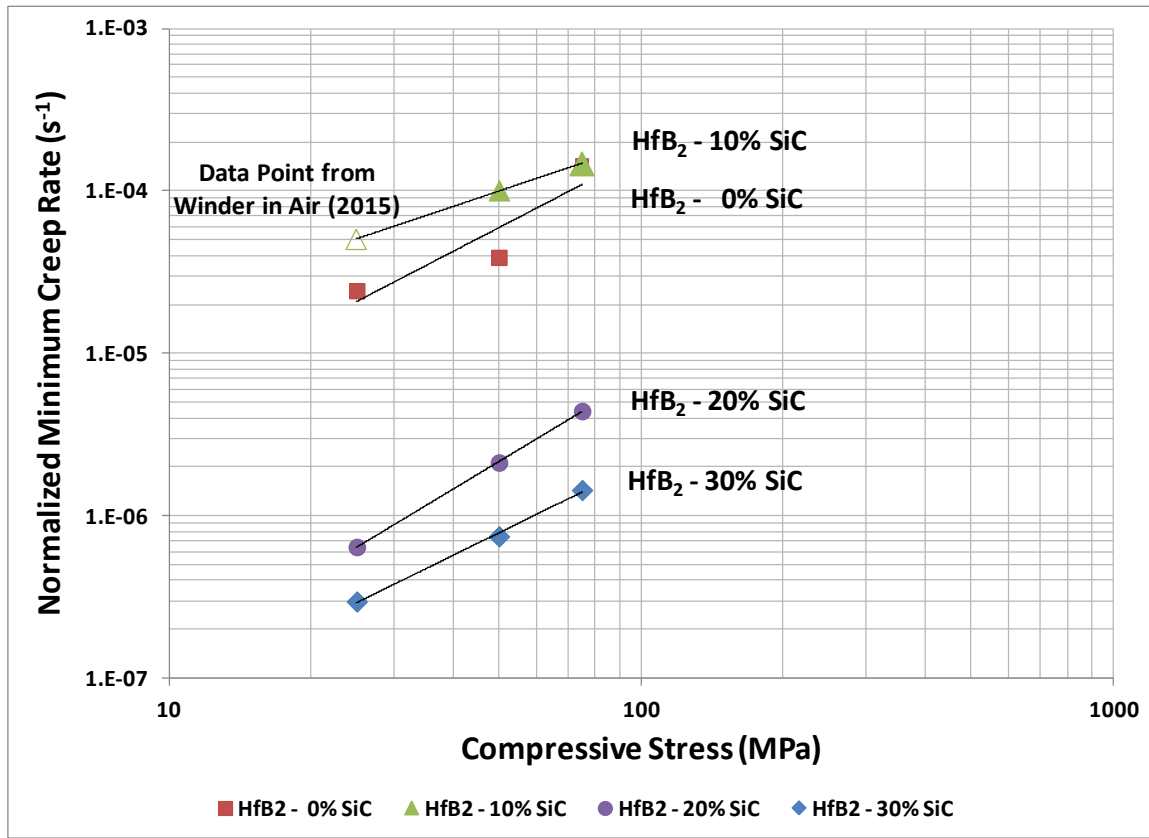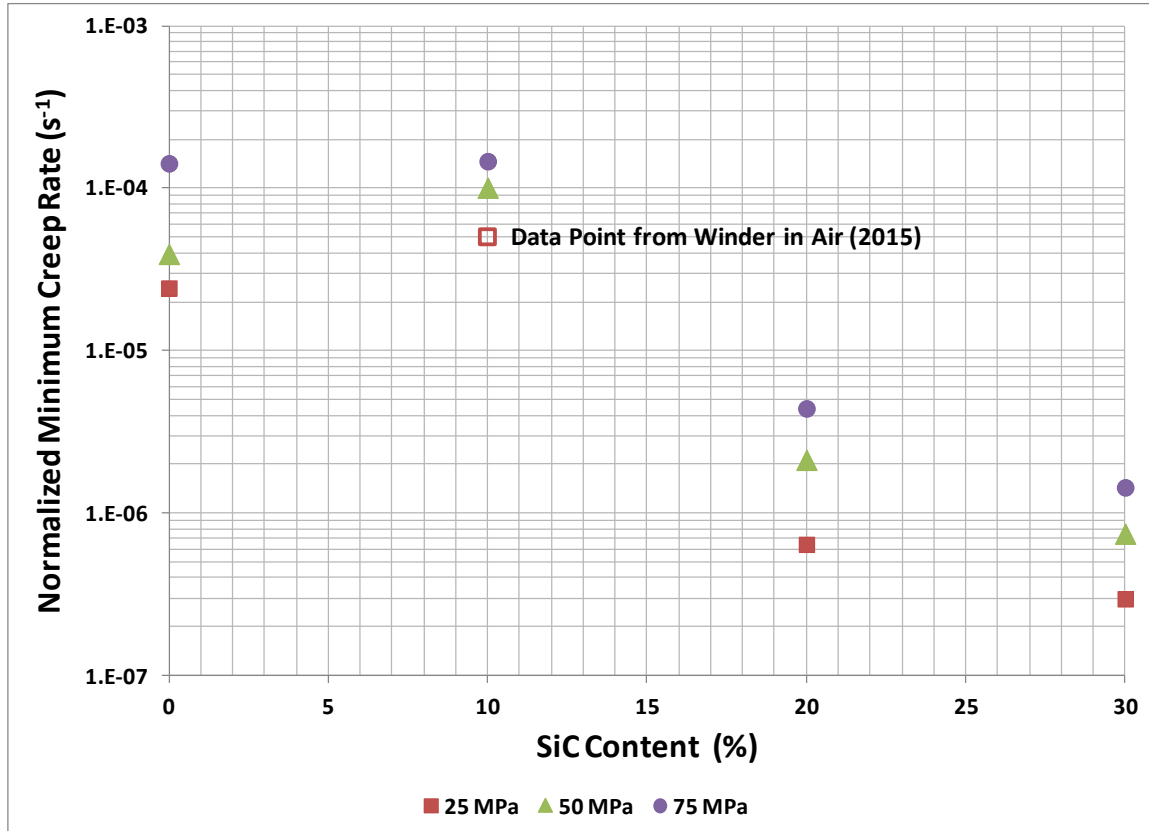

**Figure 28: Normalized Minimum Creep Rate vs SiC Content
for HfB$_2$ at 25, 50, and 75 MPa and 1500°C in Argon
Data Point for HfB$_2$-10% SiC at 25 MPa from Winder in Air** [13]

Once again, the normalization of grain size shows that SiC content has little effect on minimum creep rates from 0% to 10%, suggesting that grain size effects dominate. However, increasing to 20% and 30% brings a remarkable 2-order of magnitude decrease in the minimum creep rates, which suggests that the effects of SiC content dominate. It is

105

interesting to note, if the previous assumptions regarding the HfB_2-0 and -10% SiC materials are relaxed, their creep rates would be lower than reported in this research and their data points would move downward in Figure 28. Then, the effects of SiC content, after removing grain size effects, would appear to have a more consistent trend across the range from 0% to 30% SiC. More likely, as previously discussed, the effect of SiC content on the creep rates follows Wilkinson's treatment [102], and the reported minimum creep rates for HfB_2-0 and 10% SiC are near the secondary creep rates. From this perspective, the previous figure illustrates the modest effect that small amounts of SiC content have on the creep rate of HfB_2, independent of grain size. Then, before 20% SiC content, creep rates start to decrease, eventually dropping two orders of magnitude by 30% SiC. Thus, the grain size analysis reaffirms the proposal that Wilkinson's framework aligns with the results of this research.

Regardless of how SiC content affects creep, the grain size analysis shows that a transition between the dominance of grain size and SiC content exists as portrayed in Figure 25. Thus, normalizing the creep rates for gain size and re-presenting the results of the other analysis sections shows that a grain size exponent of 2 is consistent with the assumptions and proposals made throughout the *Results and Analysis* section. Grain size exponents close to 2 suggest that boundary mechanisms dominated the creep rates, which was also indicated in the analysis of stress exponents. It also suggests, more specifically, that Nabarro-Herring creep dominates, with Coble creep occurring in some proportion. However, additional information is needed before drawing such specific conclusions, and would not necessarily apply to HfB_2 materials at all percentages of SiC content. In either case, diffusion would play an important role in the dominant creep mechanism.

106

4.5 Effect of Oxidation on the Creep of HfB$_2$-SiC

Results: One of the objectives of this research was to maintain as much similarity as possible to the work of Winder [13], in the hopes that the data could be usefully compared with minimal difficulty. Since Winder performed her work in air, and this research performed its work in argon, Table 11 takes advantage of that opportunity, bringing the data together and considering the effects of oxidation on creep.

Table 11: Minimum Creep Rates for HfB$_2$-SiC Materials at 1500°C in Argon and Air (All minimum creep rates are in units of 10^{-8} s^{-1}) Data in Air from Winder [13]

Creep Stress at 1500°C	Argon				Air			
	HfB$_2$- 0% SiC	HfB$_2$- 10% SiC	HfB$_2$- 20% SiC	HfB$_2$- 30% SiC	HfB$_2$- 0% SiC	HfB$_2$- 10% SiC	HfB$_2$- 20% SiC	HfB$_2$- 30% SiC
25 MPa	1.59	-	4.50	2.76	1.54	168	1.69 2.65 3.58 52.0	-
50 MPa	2.55	336	14.9	6.95	24.8 33.6	-	4.52 13.4	-
75 MPa	9.31	489	30.9	13.4	6.12 18.2	-	-	-
100 MPa	-	-	-	-	32.4	-	116	-

A thorough review of Winder's results and the current research could provide many points for discussion. However, in light of the present research's objectives, it is sufficient to present the minimum creep rates and point out that the creep strains and durations experienced in air by Winder were generally higher than in argon by this work.

Analysis: The combined results provide a good number of data points to compare for the HfB$_2$-0% and -20% SiC materials. However, there are no direct comparisons available between the -10% and -30% SiC materials in air and argon at any stress level. Thus, Figure 29 presents all of the HfB$_2$-0% and -20% SiC results in argon and air, along with trendlines for each material as a point of reference.

**Figure 29: Minimum Creep Rate vs Compressive Stress
for HfB$_2$-0% and -20% SiC at 1500°C in Argon and Air
Data in Air from Winder** [13]

From this initial perspective, it appears the magnitude of the minimum creep rates in argon were generally less than in air (i.e. the filled squares representing tests in argon all fall below the overall trendline for HfB$_2$-0% SiC). This does not appear as true for HfB$_2$-20% SiC, whose results generally appear similar in argon and air. It is possible that the

differences between the results in argon and air are less severe for HfB$_2$-20% SiC, because of the enhanced oxidation resistance of the SiC-containing materials. For both materials, it appears that the scatter in the data prevents a simple plotting of the results from leading to any clear conclusions regarding the effects of oxidation on creep. Thus, a closer look is warranted.

First, consider the results normalized for grain size. The HfB$_2$-0% and -20% SiC materials in this work and Winder's work used the same sources and processes, but came from different lots with different grain sizes. Figure 30 uses Equation 31 to normalize all of the results to a 1 µm grain size. *Appendix G* starting on page 161 presents individual figures and additional trendlines for the two materials in argon and air.
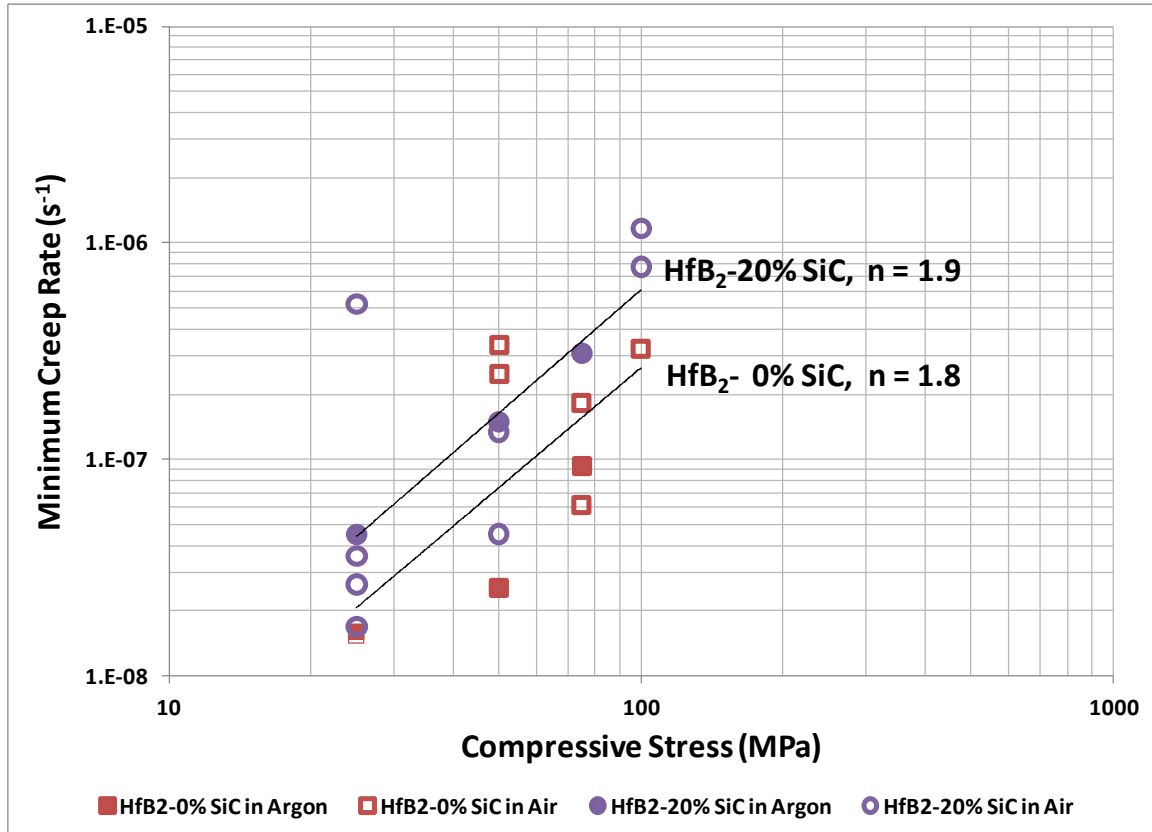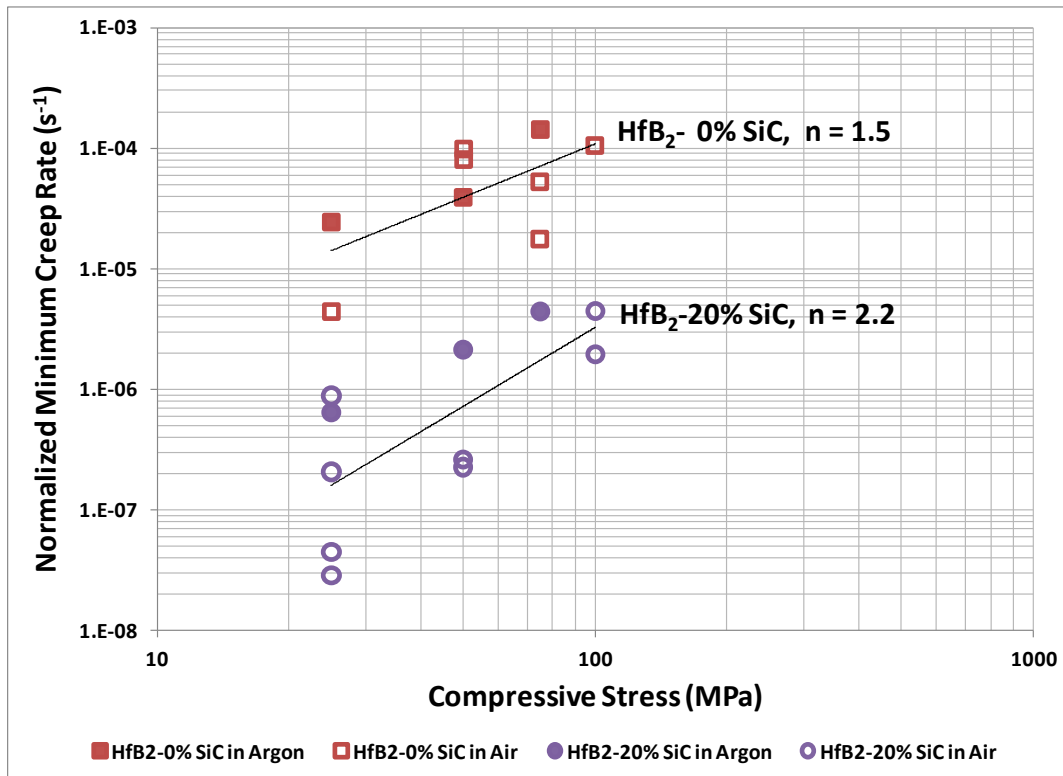

**Figure 30: Normalized Minimum Creep Rate vs Compressive Stress
for HfB$_2$-0% and -20% SiC at 1500°C in Argon and Air
Data in Air from Winder** [13]

Unfortunately, normalizing the results for grain size appears to have painted a picture that defies the previous logic (i.e. the filled squares and circles representing tests in argon all fall above or near the overall trendline for the respective material). Thus, the results for both materials appear to have slightly higher minimum creep rates in argon than in air. Considering the porous microstructure of the oxide, it is natural to assume that higher oxidation rates in air would lead to higher minimum creep rates. Since this expectation is not reflected in the data, there must be other, larger factors to consider, which create the apparent scatter in the experimental data.

At a minimum, we would expect oxidation to affect the creep rate by decreasing the effective load bearing area of the parent material. What might the order of magnitude of such a decrease be in a worst case scenario? Gangireddy et al. [15] provided a useful approach with Equations 10 and 11, where the oxidized material is assumed to carry no load, a true stress is calculated, and then used to correct the strain rate. To simplify the process, let us select a scenario and simply look at the ratio of the nominal stress to the true stress, squared, which is the factor used to correct the strain rate in Equation 11. Given 10 hours at the oxidation rates presented in Table 8 on page 85, Table 12 gives strain rate correction factors for the HfB_2-0% and -20% SiC materials in argon and air.

**Table 12: Strain Rate Correction Factors
for the Oxidation of HfB_2-SiC Materials at 1500°C in Argon and Air**

Material (HfB_2-)	Strain Rate Correction Factors	
	Argon	Air
0% SiC	0.99272	0.96342
20% SiC	0.99942	0.99807

The differences in the strain rate correction factors between argon and air for the HfB_2-0% and -20% SiC materials are less than 3.5% and 0.7%, respectively. These values are much less than the variations observed in the results. This does not mean that oxidation has no effect on creep rates. However, it is safe to say that, if oxidation was affecting the creep rates by reducing the load bearing areas, the results analyzed in this research are not sufficient to identify the effect.

Finally, due process obligates us to look at the stress exponents in argon and air to see if any effects of oxidation on creep might be observed. The stress exponents are presented in Table 13.

Table 13: Stress Exponents for HfB_2-SiC Materials at 1500°C in Argon and Air Data in Air from Winder [13]

Material (HfB_2-)	Stress Exponents	
	Argon	**Air**
0% SiC	1.5	1.7
20% SiC	1.8	2.1

Although the stress exponents seem slightly higher in air than in argon, the variations in the results due to other factors seem large compared to any differences that might be attributed to the environments. *Appendix G* starting on page 161 provides some supporting analysis. Thus, the results are considered insufficient to draw any conclusions about the effects of oxidation on creep rates, other than to say that this research shows no effect at these conditions. However, it is interesting to note that, if compressive stress increases oxidation rates, then higher stress exponents might be expected in air than in argon, which is discussed in the following section.

4.6 Effect of Compressive Stress on the Oxidation of HfB$_2$-SiC

Results: There appears to be no experimental results in the literature regarding

the effect of compressive stress on the oxidation of transition metal diborides. Winder's

work [13] is an exception, but all of the data points in that work came from separate creep

tests and were compared to a modeled baseline (i.e. 0 MPa), instead of an experimentally

validated baseline. Thus, preliminary tests were conducted, using an extra long alumina

spacer in place of one of the standard-sized spacers. This provided additional room, so a

scrap specimen could be set to the side of the creep specimen in the furnace chamber, as

seen in Figure 31. Thus, specimens from the same lot were heated to 1500°C in the same

environment for the same length of time, but one was subjected to compressive creep

stress, and the other remained under no load. Assessing the cross sections after the test

showed that oxidation scales remained generally uniform on all sides, suggesting the

conditions were also uniform for both specimens. This type of test was termed a stressed
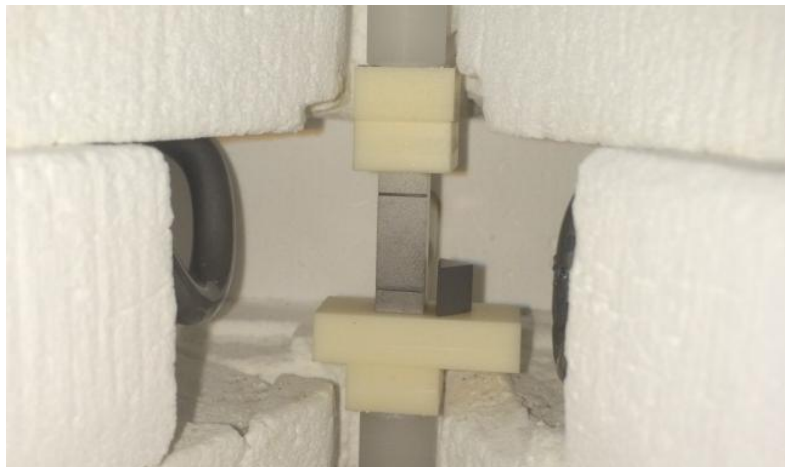
oxidation test.

**Figure 31: Photo of Specimens before a Preliminary
Stressed Oxidation Test of HfB$_2$-20% SiC**

Preliminary stressed oxidation tests were conducted for HfB_2-0% and -20% SiC at 75 MPa. The specimens were at the test temperature of 1500°C for 2 and 4.5 hours, respectively, while the durations of the creep tests were 1 and 3 hours. Figure 32 shows SEM images from the cross sections of the specimens after testing, as well as the average, standard deviation, and range of the oxide scale thicknesses. These statistics were all based on 48 or more measurements each, using the methods described in the *Data Collection* section.

HfB_2-0% SiC Compressed	HfB_2-0% SiC Uncompressed	HfB_2-20% SiC Compressed	HfB_2-20% SiC Uncompressed
Oxide Thickness Average: 101 μm Std Dev: 18 μm Range: 70-135 μm	**Oxide Thickness** Average: 106 μm Std Dev: 31 μm Range: 46-155 μm	**Oxide Thickness** Average: 50 μm Std Dev: 8 μm Range: 34-74 μm	**Oxide Thickness** Average: 28 μm Std Dev: 10 μm Range: 12-53 μm
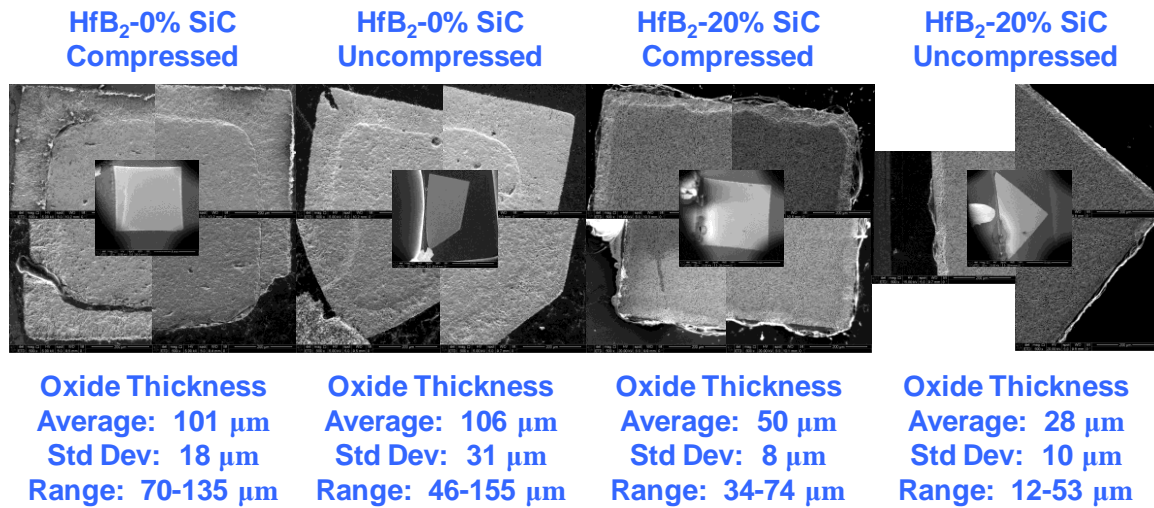
Figure 32: Results of the Preliminary Stressed Oxidation Tests

Since preliminary stressed oxidation tests produced interesting data, efforts were made to design an experiment and procedures for more meaningful tests. The objective was to collect convincing data and provide an idea of oxide scale thickness with respect to time for specimens under compression. Over a dozen methods were considered, and several attempted, but finding a reliable method to measure oxide scale thickness at various time intervals in the course of a compressive creep test at 1500°C proved difficult. However, a sufficient compromise was found that met the objectives of this

113

research. The stressed oxidation tests would be stopped at the desired time interval and the specimens cooled and removed from the setup. Then, a section of specimen would be removed by cutting, and the remaining length re-inserted into the test setup, so the stressed oxidation test could continue. The removed section would be used to determine the oxide scale thickness for that time interval. Unfortunately, the scale of HfB_2-0% SiC was too brittle and detached from the parent material that a reliable method could not be found to cut the specimen and not disturb the remaining scale. However, HfB_2-20% SiC was able to be cut without disturbing the scale. Unlike the preliminary tests, the stressed oxidation test used full sized specimens for both the compressed and uncompressed test articles. Additionally, based on temperature profiles conducted with a thermocouple, the specimens were placed one behind the other, as shown in Figure 33, so they would experience similar heating. Both specimens were prepared and handled in the same way.
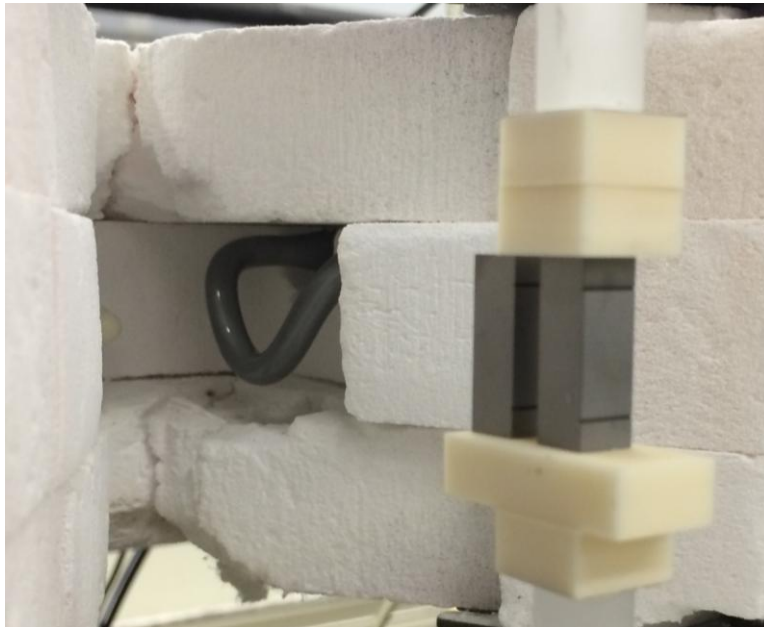

Figure 33: Alignment of Specimens for HfB$_2$-20% SiC Stressed Oxidation Test (Prior to Furnace Entry)

Table 14 presents the results of the stressed oxidation tests conducted on HfB_2-20% SiC at 50 MPa in air. Results are also provided for the no-load specimen (i.e. $\sigma = 0$ MPa) from the same puck of material, which was located inside the furnace chamber, behind the 50 MPa specimen, and was otherwise subjected to the same environment and experimental procedures as the 50 MPa specimen. Recall, from the *Methodology*, that oxide scale thicknesses reported in this research include the total of the glass, metal oxide, and SiC-depleted regions, which does not imply that all three regions are present in any given measurement. Photos of the specimens at each time interval may be found in Figure 38 on page 124.

Table 14: Stressed Oxidation Test Results for HfB$_2$-20% SiC at 50 MPa in Air

Cumulative Creep Time	Creep Stress	Average Oxide Scale Thickness (µm)	Standard Deviation	Number of Measurements	Minimum (µm)	Maximum (µm)
5.00 h	0 MPa	47	13	100	21	78
	50 MPa	55	9	100	35	81
8.25 h	0 MPa	67	14	85	40	95
	50 MPa	63	11	100	35	95
9.37 h	0 MPa	77	18	100	18	117
	50 MPa	73	15	109	29	136
11.75 h	0 MPa	81	24	100	28	159
	50 MPa	73	19	98	33	179
12.27 h	0 MPa	84	23	91	36	155
	50 MPa	70	22	64	37	135

Analysis: The preliminary stressed oxidation tests appear to suggest that compressive stress does not affect the oxidation of the HfB_2-0% SiC material, but does affect HfB_2-20% SiC. This is entirely possible, especially considering that the oxidation mechanisms of the two materials are different.

With the HfB_2-0% SiC material, there is no glass phase filling the pores of the oxidized material, and the stress levels might not affect the diffusion of oxygen through the open pores of the material. The closeness of the average oxide thicknesses for the compressed and uncompressed HfB_2-0% SiC materials (i.e. 101 and 106 μm) supports this idea. However, these results do not necessarily mean that there are no effects of stress on oxidation, only that there are no measured effects at this stress level. The differences in the standard deviations and ranges of oxide scale thicknesses suggest there might be something different between the oxidation of the compressed and uncompressed HfB_2-0% SiC specimens. This particular test only lasted for 1 hour, but did show a 5% difference in average oxide thickness. Tests for longer durations and/or at higher stress levels could show a more pronounced effect. However, at 75 MPa and 1 hour, no measured difference was observed in the oxidation of compressed and uncompressed HfB_2-0% SiC.

In the absence of more convincing data on the effects of compressive stress on the oxidation of HfB_2-0% SiC, it is prudent to glean what we can from the results presented in the literature. Unfortunately, there is very little information available on the oxidation of transition metal diborides under stressed conditions. In fact, only one work, Winder's work [13], presents an oxide scale thickness following a test for a given time, temperature, and non-zero stress. Winder reports such information for three campaigns

116

of materials. Two of the materials are not included in Figure 34, because they had notable differences in composition (i.e. Pt, HfO_2, and SiC within grain boundaries). Winder discussed these compositional differences in relation to oxidation results that varied by more than 100%. Fortunately, Winder's other campaign seems to have a similar composition to the material from this research's baseline oxidation test of HfB_2-0% SiC. There is a difference in grain size, but the effects are assumed small in a comparison of the oxidation rates. *Appendix H* starting on page 164 provides information about the baseline oxidation test.
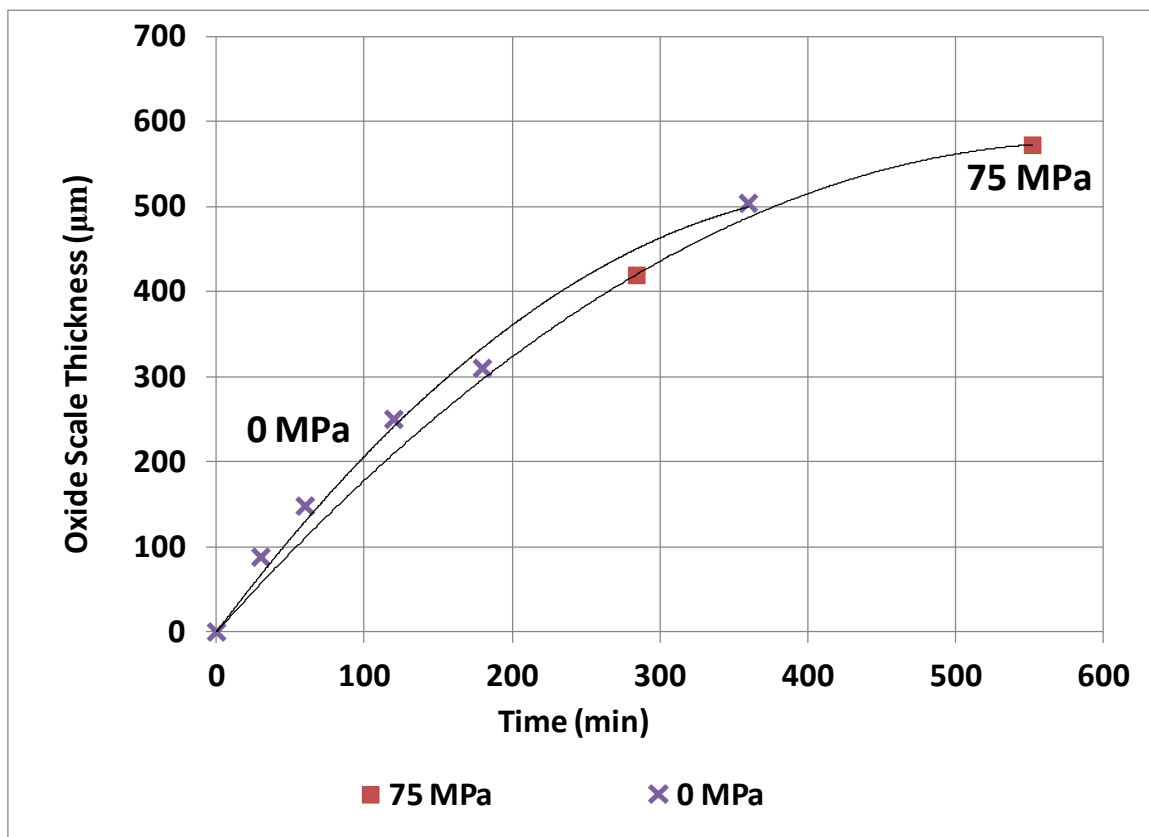
**Figure 34: Oxide Scale Thickness vs Time
at Two Different Stress Levels for HfB₂-0% SiC at 1500°C in Air
Data at 75 MPa from Winder** [13]

What is remarkable about Figure 34 is how close the oxidation rates appear, even though they are from 0 and 75 MPa tests. Along with the previously discussed results from the preliminary stressed oxidation test, this comparison also suggests that compressive stress has little effect on the oxidation of HfB_2-0% SiC at these conditions, even after almost 10 hours at 75 MPa. However, it is also clear that other factors, such as composition, can have an overwhelming effect. Thus, due to the comparison being made between two different lots of materials and the sparseness of the data, any conclusions should be made with caution. Nonetheless, this research has presented two independent tests, both of which suggest that there is no measured difference in the oxidation rates of HfB_2-0% SiC at 75 MPa and 1500°C for up to several hours.

A similar comparison to Winder's work can also be made for HfB_2-20% SiC, since the composition also seems similar to this research. Although there are three data points available from Winder's work, they all come from different stress levels (0, 25, and 50 MPa), as opposed to the same stress level at different times. So, in order to utilize this diversity of this data in a meaningful way, Figure 35 normalizes the oxide scale thickness with time and adds stress to the abscissa. The normalization assumes parabolic oxidation kinetics and squares the oxide scale thickness, then divides by time. The data from the HfB_2-0% SiC tests are also included in Figure 35, which includes three data points (25, 75, and 75 MPa). Although there are some more data points available in Winder's research, as well as other works, especially at 0 MPa, this is all of the data available that meets the following two requirements: 1) data points at two different stress levels and 2) with similar materials. Of course, the reported data must also include the material composition, temperature, stress level, duration, and oxide scale thickness.
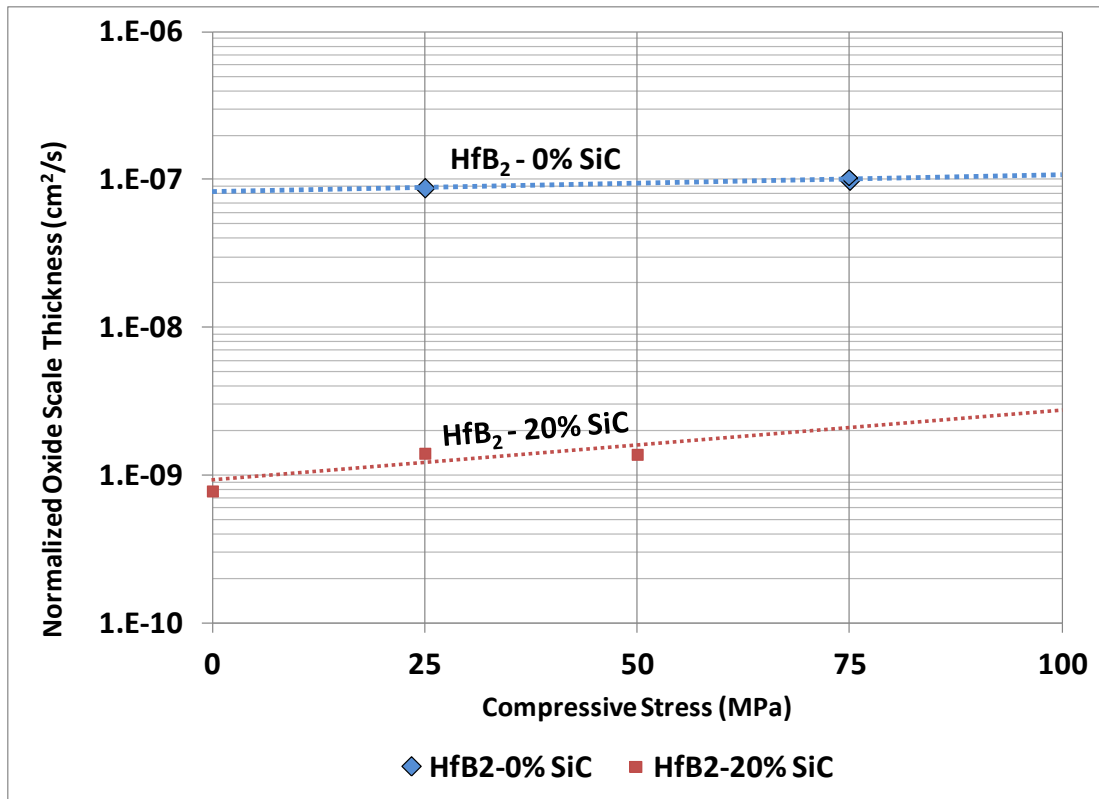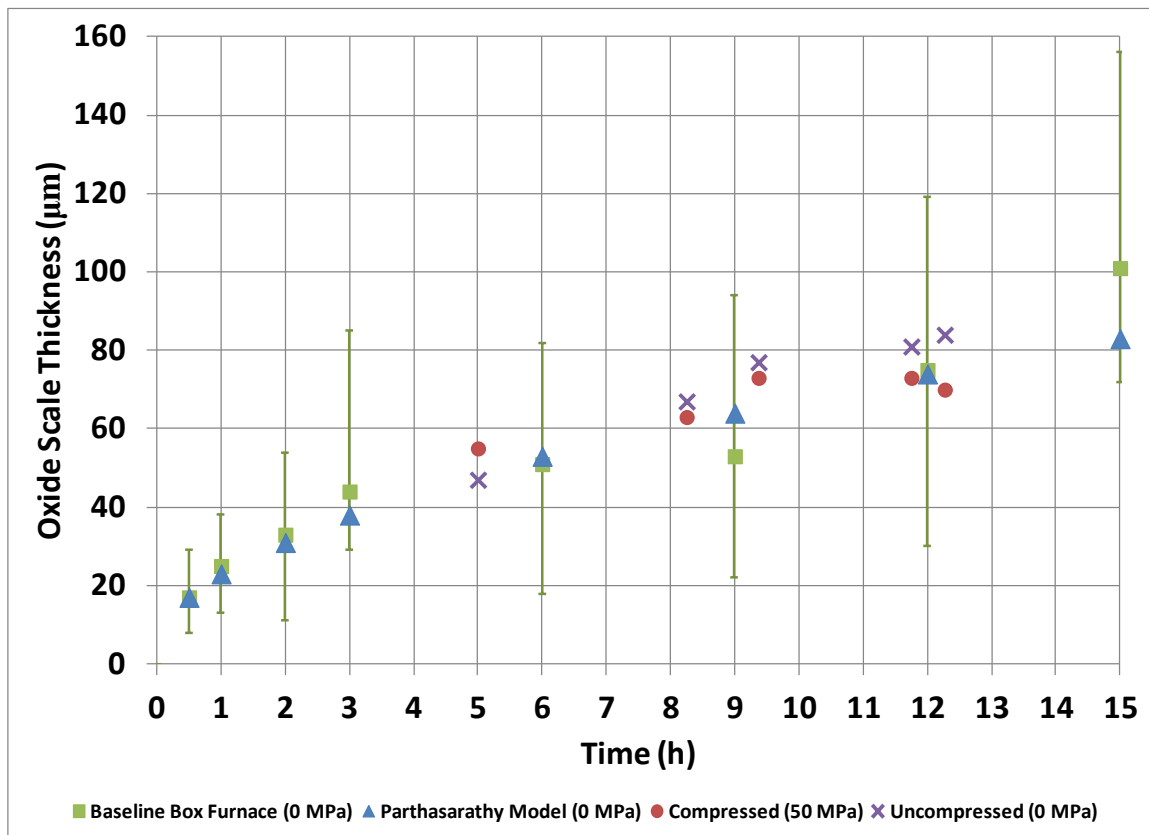
**Figure 35: Normalized Oxide Scale Thickness vs Time
for HfB$_2$-0% and -20% SiC at 1500°C in Air
All Data from Winder** [13]

For the HfB$_2$-20% SiC material in Winder's work, Figure 35 appears to show an increase in the normalized oxide scale thickness as compressive stress increases. However, the normalized oxide scale thickness appears consistent for HfB$_2$-0% SiC. Both results are consistent with the preliminary stressed oxidation tests. However, the data is limited, and the trend in the HfB$_2$-20% SiC data very small, which motivates further investigation by analyzing the results of this research's stressed oxidation test.

The most effective way to analyze the results of the HfB$_2$-20% SiC stressed oxidation test at 50 MPa and 1500°C in air is to graphically compare the results to the uncompressed specimen of the same lot of material, which was sitting right behind it in

the same furnace chamber. Figure 36 does that and includes data from a baseline

oxidation test that also occurred in air under no load at 1500°C, but in a different furnace.

The purpose of this baseline test was to provide oxide scale thickness versus time in a

more controlled and continuous environment, so the effects of stopping and starting the

stressed oxidation tests might be more fully understood. The bars on the data points

reflect the range of oxide scale thicknesses measured during the baseline test. *Appendix

H* starting on page 164 provides details about the HfB_2-20% SiC baseline oxidation test.

Figure 36 includes results from the model referenced in the *Literature Review*, which

were kindly provided by Parthasarathy for the same conditions [98].

**Figure 36: Oxide Scale Thickness vs Time
for HfB_2-20% SiC at 50 MPa and 1500°C in Air
Model Data from Parthasarathy** [98]

Figure 36 shows no apparent difference in the oxidation of compressed and uncompressed HfB_2-20% SiC materials, even after 12 hours at 50 MPa. Both sets of data compare favorably with Parthasarathy's model. Additionally, the data compares favorably with the baseline oxidation test, which suggests the cooling and heating cycles imposed on the materials during the stressed oxidation test did not cause any measured differences in the results. Looking back at the HfB_2-20% SiC preliminary stressed oxidation test, it is easy to identify reasons that could have caused the compressed and uncompressed specimens to have different oxide scale thicknesses, whereas the actual stressed oxidation test did not. Probably most imoprtantly, the uncompressed specimen was a much smaller, triangular geometry with a corner, instead of a flat surface, facing the adjacent heating element (reference Figure 31 on page 112). Thus, heating of the uncompressed specimen could have been less than found in the temperature calibrations that were performed on full-sized, rectangular specimens, resulting in a thinner and less turbulent oxide scale. Additionally, the preliminary tests were conducted at 75 MPa, versus 50 MPa in the actual test. It is important to keep in mind that the preliminary tests were exactly that…preliminary. They were short-duration tests of scrap material in order to determine whether there might be measurable differences in oxidation behavior that should be further investigated. Thus, the bottom line in the analysis of these stressed oxidation tests is that no measurable difference was found in the oxidation behavior of the HfB_2-20% SiC materials after over 12 hours at 50 MPa and 1500°C in air.

It is interesting to note that a smooth and consistent surface layer of glass and HfO$_2$ was only observed in the uncompressed specimen at the first (i.e. 5-hour) time interval. Recall, a similar observation was made in the uncompressed specimen in the preliminary stressed oxidation test (reference Figure 32 on page 113). At all other time intervals, and for the compressed specimen, the oxide scale was inconsistent, as described in the literature by Shugart in terms of scallops. This time interval also corresponded to the only time interval where the average oxide scale thickness was smaller for the uncompressed specimen, although the difference was small and standard deviation higher. Thus, we are left with the thought that uncompressed specimens might be more likely to develop smooth and consistent glass layers than compressed specimens. Regardless of this more frequent smoothness and consistency in the glass layer early on, the long term oxidation behavior of the uncompressed specimen did not appear measurably different than the compressed specimen at later time intervals. Figure 37 provides example micrographs of the oxide scales from the stressed oxidation test at the 5-hour time interval. The uncompressed specimen exhibited a smooth and consistent glass layer more frequently than the compressed specimen, only at this time interval.
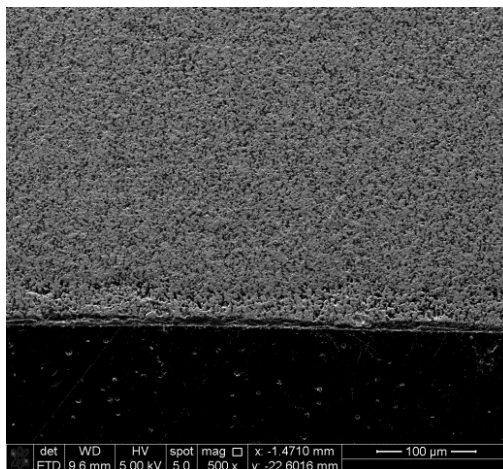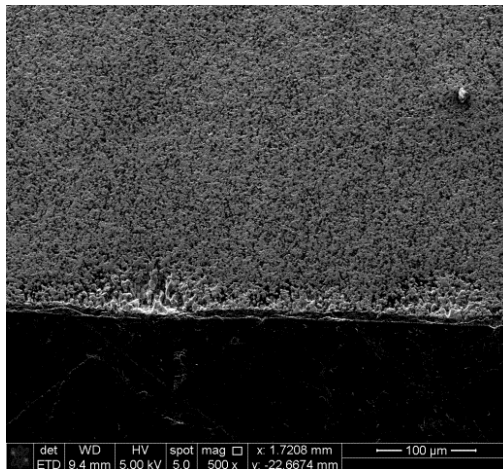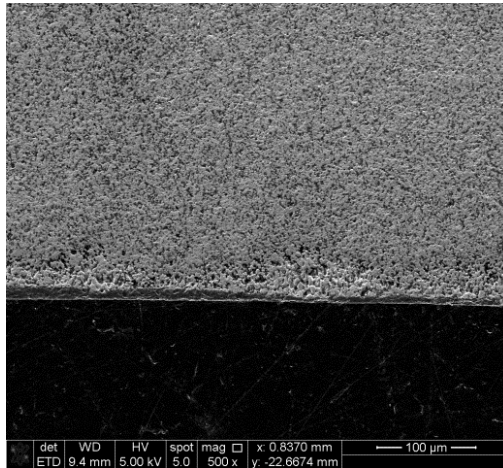
Uncompressed   **Compressed**
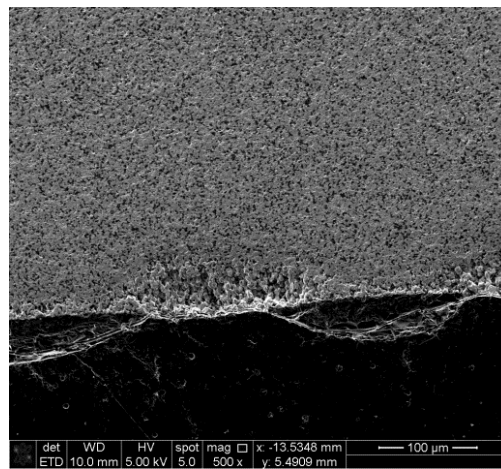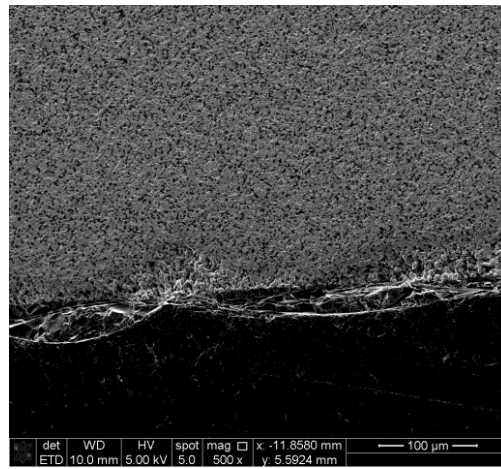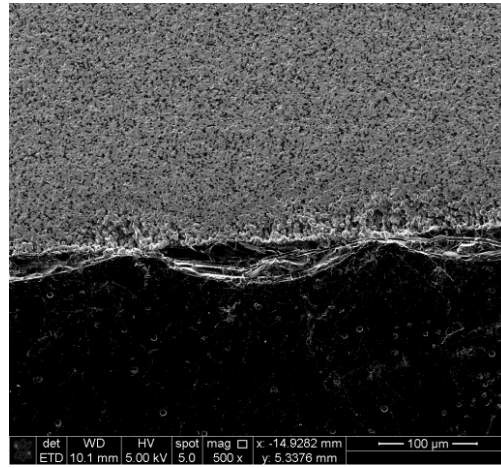
Figure 37: SEM Images of HfB$_2$-20% SiC Oxide Scales after 5 h at 1500°C in Air from the Stressed Oxidation Test – Uncompressed (Left) and Compressed (Right)

Snapshots of the stressed oxidation test specimens at the various time intervals, chronicled in Figure 38, provided an opportunity to show that large defining surface features, identified as initial burst bubbles, do not appear to change much with time, even with cooling and reheating.
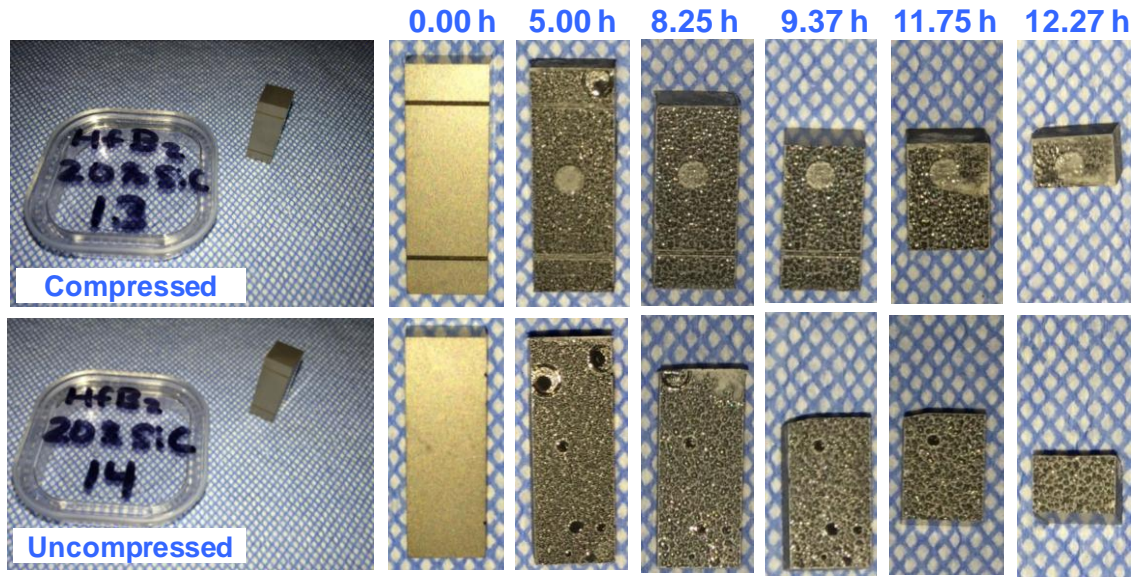
Figure 38: Photos of Identical, Initial Burst Bubbles Observed throughout the Stressed Oxidation Test

Like Shugart's work and the previous discussion about the smooth and consistent glass layer observed in the uncompressed specimens early on, these results speak to whether interesting details in the initial formation of the oxide scale have significant effects on long-term oxidation behavior. Such phenomena are not a focus of this work, but further discussions and illustrations, which are captured from the baseline oxidation test, are provided in *Appendix H* starting on page 164.

V. Conclusions

This body of research produced new and relevant knowledge related to the creep and oxidation of the HfB_2-SiC material system. The knowledge provided a better understanding, not only of this material system, but also of similar ultra high temperature ceramics. Furthermore, the knowledge provided hope for improved material performance and future, defense-focused, structural applications. The following sections summarize this knowledge in the categories of creep, SiC's effect on creep, the interaction of creep and oxidation, oxidation, and finishing with recommendations for future research.

5.1 Creep of the HfB_2-SiC Material System

Modifications to a high temperature experimental facility successfully enabled uniaxial, compressive creep tests at 1500°C in argon. The experimentation in argon provided good creep results, not confounded by the effects of oxidation. The research materials, which included HfB_2-0%, -10%, -20%, and 30% SiC by volume, exhibited minimum creep rates from about 10^{-8} to 10^{-6} s^{-1}, over a range of stresses from 25 to 75 MPa, resulting in stress exponents between 1 and 2.

A thorough analysis showed that the effects of SiC content could be decoupled from grain size, thanks to the various grain sizes and SiC contents of the research materials. The difference in grain sizes and creep rates between the HfB_2-0% and -10% SiC materials provided the key basis for a determination of a grain size exponent, assuming the effects of grain size dominated the effects of SiC content. Thus, for the first

time, experimental results were used to show grain size exponents close to 2 for this material at these conditions, although this conclusion might not apply to all percentages of SiC content.

The grain size exponents reinforced the notion that boundary mechanisms accommodated by diffusion dominate creep rates at these conditions. More information is needed before drawing specific conclusions, but together the stress and grain size exponents suggest that Nabarro-Herring creep dominates, with Coble creep occurring in some proportion. Normalization of the creep rates for grain size confirmed the assumptions made in the analysis and enabled additional conclusions regarding the effects of SiC content, which are presented in section 5.2.

Overall, the creep results confirm, in an argon environment, that boundary mechanisms dominate the creep rates at these conditions, with diffusion through grains playing an important role.

5.2 SiC's Effect on the Creep of HfB$_2$

A 10% addition of SiC to HfB$_2$ decreased grain sizes about an order of magnitude and increased minimum creep rates two orders. However, 20 and 30% additions of SiC decreased minimum creep rates about two orders of magnitude, while grain sizes remained steady. This research proposed the idea that the effect of grain size dominated the changes in creep rates from 0 to 10% SiC, while the effect of SiC content dominated from 10 to 20 and 30% SiC. As previously discussed, a thorough analysis validated this proposal, resulting in grain size exponents near 2. After decoupling grain size effects, the

effect of SiC content was shown for the first time with these materials to be consistent with Wilkinson's framework. This suggests that small additions of SiC have a modest effect on creep rates, independent of grain size, but drive down creep rates by more than an order of magnitude as SiC begins to percolate a network of point-to-point contacts, somewhere near 10% and/or before 20% SiC content.

Thus, small additions of SiC resulted in higher creep rates, primarily due to changes in grain size. Larger additions eventually resulted in the formation of a network of point-to-point contacts and increased creep resistance. This transition is important to the future design and application of these material systems, as well as the magnitude and breadth of the effect. Caution should be taken when designing these materials for creep and oxidation resistances, because small changes in SiC content could result in large changes to creep strains and rates, if in the vicinity of percolation. Effectively, this work concludes that a transition in compressive creep mechanisms occurs at some combinations of strain and low SiC content, as SiC grain interactions take effect. Furthermore, it is assumed that the formation of a SiC network that increases creep resistance in compression would probably proceed differently or not at all in tension, providing a clear reason why the creep behavior of these materials might be different in tension and compression.

5.3 Interaction of Creep and Oxidation in the HfB$_2$-SiC Material System

The creep results in argon were compared to Winder's similar results in air, and the effect of oxidation was within the scatter of experimental measurements. Thus, the

effects of oxidation on creep might be considered small at these conditions, namely less than an order of magnitude at 1500°C, from 25 to 75 MPa in compression, and for up to 15 hours. The effects of oxidation on creep rates of magnitudes less than those reported and durations longer than those tested were of less interest to this research, whose objectives related to potential aerospace applications.

To consider the effects of compressive stress on oxidation, this research devised a unique stressed oxidation test, which included simultaneous assessments of oxide scale thickness at various time intervals on compressed and uncompressed specimens, subjected to the same environment. Although preliminary tests and limited data in the literature suggested that compressive stress might affect the oxidation of HfB_2-20% SiC, the stressed oxidation tests showed no measurable effect after 12 hours at 1500°C and 50 MPa in air. Thus, with no significant effects of oxidation on creep or compression on oxidation, this research showed that the effects of creep and oxidation might be decoupled in future models of these materials at these conditions.

5.4 Oxidation of the HfB_2-SiC Material System

Unexpectedly, the oxidation tests performed in this research provided some interesting perspectives on burst bubbles and the long term effects of phenomena in the early development of the oxide scale. Specifically, initial burst bubbles were shown to be distinct from the burst bubbles that are suspected of producing alternating build ups of glass and metal oxide in the long term, referred to as scallops. Exciting smoothness and consistency were observed in the glass layer of uncompressed specimens early on, but did

not seem to affect overall and long term oxidation rates. However, smooth and consistent glass layers correlated, as in other research, to regions with less oxidation. Although, at times, the recovery of glass over scallops did not appear to arrest oxidation, suggesting that burst bubbles might have long term effects, possibly due to larger pores in the scallops.

As expected, SiC greatly enhanced the oxidation resistance of HfB_2, as shown with the baseline oxidation tests in air. Comparison of oxide scale thicknesses, weight gains, and microstructures of the oxide scales of the materials used in this research effort were consistent with the literature. Although within an order of magnitude, differences between the observed HfB_2-0% SiC oxide scale thicknesses and Parthasarathy's model reaffirm the need for experimental data that shows the effect of certain parameters on oxidation rates, such as pore fraction, pore radius, velocity, water content, and the porosity of the parent material. Such studies could be worthwhile, because observations in this research effort seem to suggest that the oxidation resistance of these materials can be further improved and possibly boost their demand for use in future applications.

5.5 Recommendations for Future Research

Based on the new knowledge presented in this research, a potential appears to exist for improvements to the creep and oxidation resistances of HfB_2-based UHTCs at 1500°C, with some important structural properties such as plasticity being tailorable. This assertion is primarily based on the idea that the formation of SiC networks can be beneficially used or avoided to obtain a desired plasticity or creep behavior and that

regions with very little oxidation are able to persist in some HfB$_2$-SiC materials even after 90 hours in an oxidizing environment. Thus, this work puts forward the following four recommendations for future research, in the hopes that further understanding and improvements of this and similar material systems can be made, one day leading to aerospace vehicles that can fly faster, farther, and more efficiently.

First, modify the experimental setup, so that creep and stressed oxidation tests can be conducted at higher stresses, higher temperatures, and for longer durations. Creep tests are not easy or trivial at these conditions, and the performance of the material under investigation often outpaced the materials used to construct the experimental setup, which should not seem so ironic. Some suggestions were provided in Section 4.1. The improved capability of the experimental setup could be used to act upon the following recommendation.

Second, continue creep tests to further refine the results of this research and expand the map of creep mechanisms to higher temperatures and stresses. Testing at various temperatures might also enable determination of activation energies and specific diffusion mechanisms. Similarly, stressed oxidation tests could be conducted at higher temperatures, higher stresses, and longer durations to determine if conditions exist where stress affects oxidation behavior. Creep tests could also be run for longer durations in search of creep rupture and answers to some of the questions posed in the next recommendation.

Third, take a closer look at the strengthening mechanisms occurring in low SiC-containing metal diborides. In this research, longer primary creep regimes and creep strain more than an order of magnitude higher were observed in HfB$_2$-10% SiC, which

could be driving factors in potential design applications. Not only is it important for applications trying to avoid such behavior and maximize creep resistance, but it could be important for applications trying to achieve such behavior and maximize plasticity. Some prospective questions include: What SiC content provides the highest creep rates, and how do creep rates fall off from there? How long does is take in terms of strain to work through the first percolation from a given SiC content? Does percolation reach a steady state? What is that steady state? Can grains be shaped, sized, or otherwise varied to tailor behavior?

Fourth and finally, investigate the transition from passive to active oxidation and when the transition occurs in terms of various combinations of temperature, composition, oxygen partial pressure, and any other driving parameters. SiC-depleted regions have been observed in the oxide scales of many works, but points of transition have been described much less often and only under specific conditions [42], [99], [116]. Nothing provides a multi-dimensional understanding of the boundaries between the two distinct oxidation behaviors in these materials. Understanding these boundaries could be critical to future applications.

Appendix A: Grain Size Investigation

The following pages include an Electron Backscatter Diffraction (EBSD) image and grain size distribution for each of the materials used in this research effort (i.e. HfB_2-0%, -10%, -20%, and -30% SiC). The data was gathered from a representative scrap of each material (i.e. as-sintered, pre-test), which was polished with diamond abrasives down to a 1-μm, mirror finish. The SEM work was mostly performed on the Philips XL30 with a 100 micron aperture, a spot size of 5, and an electron beam of 20 kV.

The EBSD images in Figure 40 are inverse pole figures of the HfB_2 grains only, cleaned up by automated software in a consistent manner, and gray-scaled based on image quality. Although one image shows a different micron bar in the lower left corner, all four images were taken at 500x magnification and portray a 200 by 200 micron area. The colors represent different HfB_2 grain orientations in accordance with the legend in Figure 39. Grain elongation and biases in grain orientation were not observed.
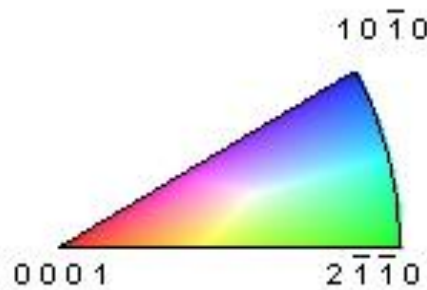
Figure 39: Grain Orientation Legend

HfB$_2$-0%SiC

HfB$_2$-10%SiC

HfB$_2$-20%SiC

HfB$_2$-30%SiC
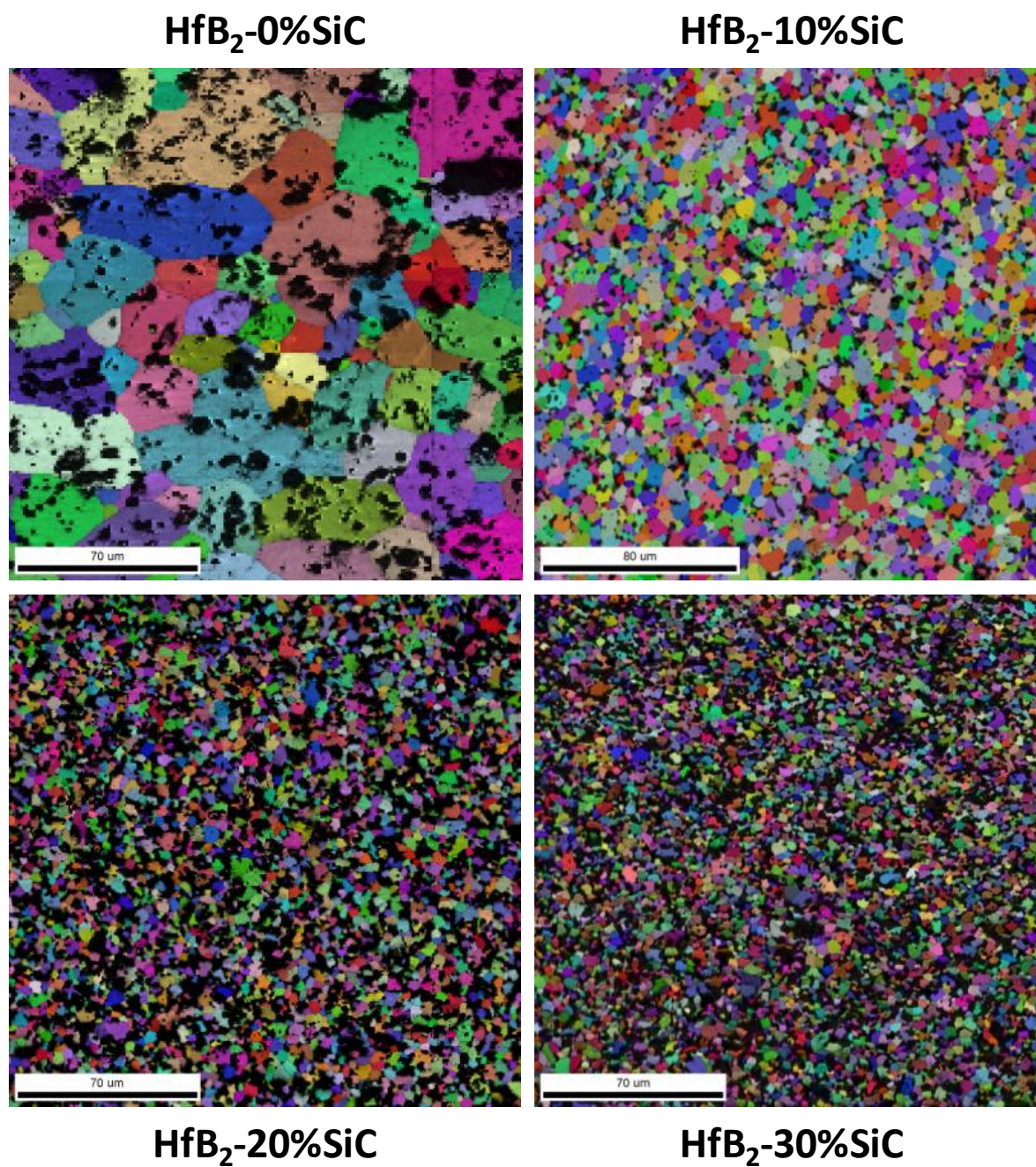
Figure 40: Representative EBSD Images of the Research Materials
(HfB$_2$-0%, -10%, -20%, and -30% SiC)

133

The automated software compiled the grain size distributions in Figure 41, which were weighted by grain area. In other words, if a material was composed of only the same number of 1-μm and 10-μm grains, the software would not report that 50% was 10-μm and the average grain size was 5.5 μm. Instead, the software would report that 91% was 10-μm and the average grain size was 9.9 μm. Each of the distributions in Figure 41 is plotted on the same scale. The vertical axes represent the area fraction and are 0 to 0.4, and the horizontal axes represent the grain size and are logarithmic from 0.1 to 100 μm. The HfB_2-0% SiC grain size distribution is based on about 1,000 grains, while the -10% is based on over 2,000 grains, and the -20% and -30% are based on over 4,000 grains.

Figure 41: Grain Size Distributions of the Research Materials (Weighted by Grain Area)

134

Table 15 presents the HfB_2 average grain size and standard deviation for each material. As expected, grain size decreased as SiC content increased. Standard deviation also decreased, indicating grain size became more uniform. Table 15 includes post-test grain sizes, which were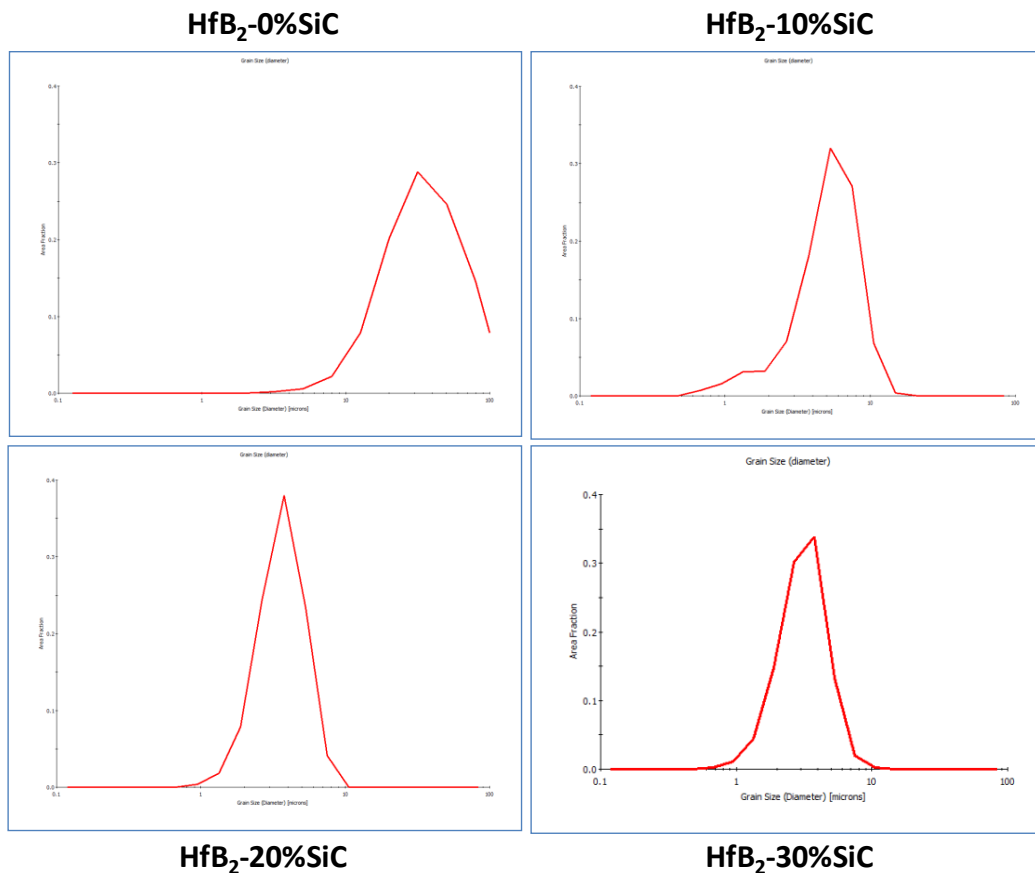 obtained from the 25 MPa creep test specimens. Each specimen was heated to 1500°C and compressed for 12 to 18 hours, depending on the specimen (reference Table 6, page 80). Differences in the pre- and post-test grain sizes of the SiC-containing materials were too small (i.e. < 1 μm) to measurably affect the creep and oxidation results (reference Equation 31 on page 103 and Figure 5 on page 46). The largest difference in pre- and post-test grain sizes was observed with HfB_2-0% SiC. This difference might be affected by the pre- and post-test specimens coming from different pucks. Regardless, the small differences in the pre- and post-test grain sizes are not expected to affect the creep and oxidation analysis and conclusions.

Table 15: Average Grain Sizes and Standard Deviations of the Research Materials

Material (HfB_2 -)	Condition	Number of Grains Counted	Average Grain Size Weighted by Area (μm)	Standard Deviation
0% SiC	Pre-test	956	39.12	13.30
10% SiC	Pre-test	2164	5.48	2.00
20% SiC	Pre-test	4371	3.78	1.19
30% SiC	Pre-test	4678	3.28	1.05
0% SiC	Post-test	506	48.96	16.43
10% SiC	Post-test	2286	5.64	1.52
20% SiC	Post-test	3705	3.61	1.03
30% SiC	Post-test	4315	2.92	0.86

Since the grain sizes were determined from a representative scrap of each material, an EBSD scan across the entire radius of a 40-mm puck was conducted, in order to gauge the expected variation in grain sizes and phase compositions within the same lot of material. For this analysis, a thin, 40-mm disc of HfB_2-30% SiC material was used; a cross-section of the spark plasma sintered puck from which the test specimens were cut. Figure 42 shows the disc and a representative EBSD tile from the scan.

Figure 42: Thin Disc of HfB₂-30% SiC (left) and Representative EBSD Tile (right)

439 EBSD tiles, each 50 by 50 μm, were stitched together to provide the data in Figure 43 and Figure 44, from the edge of the puck (EBSD Tile Number 0) to the center (EBSD Tile Number 439). In Figure 43, the average HfB_2 grain size of each tile, weighted by grain area, is plotted, along with a moving average in red.
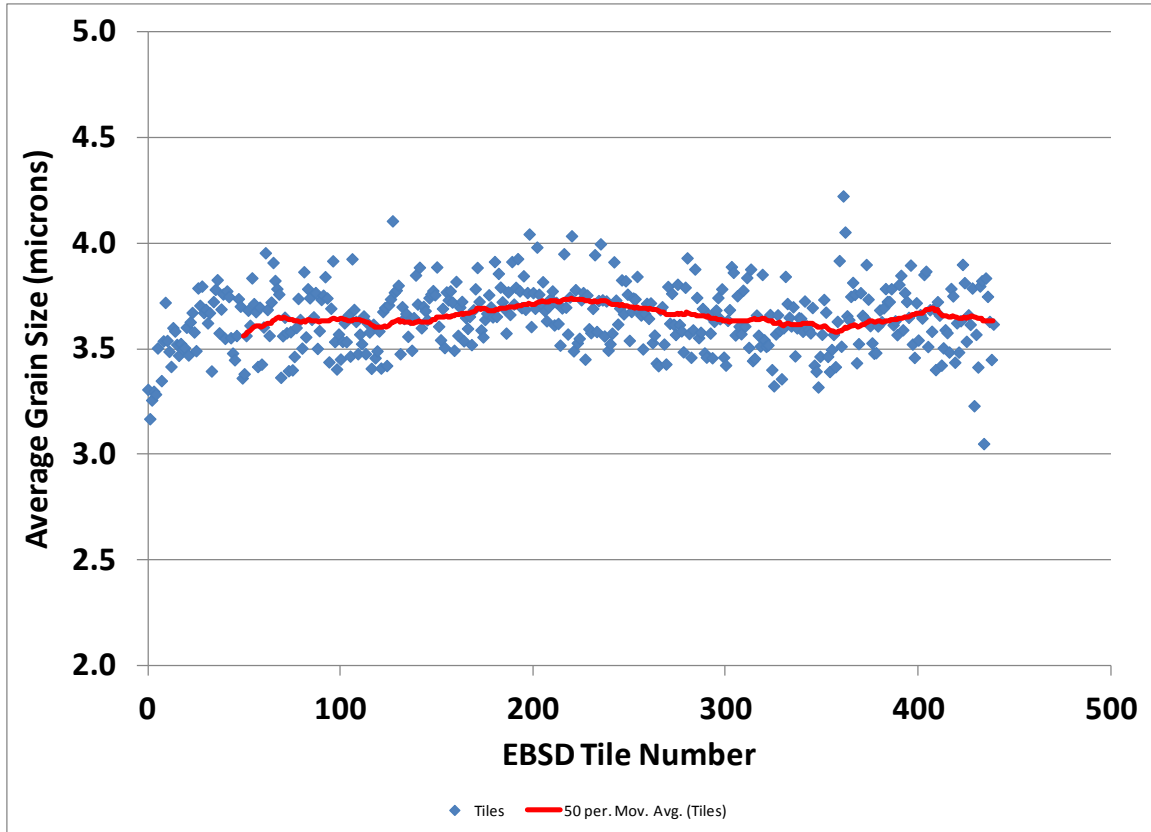
Figure 43: Average HfB$_2$ Grain Size Across a Puck of HfB$_2$-30% SiC Material (Weighted by Area)

Figure 43 shows that the HfB$_2$ grain size is very consistent, within 1 μm, across the entire radius of the puck. However, it appears there might be a slight decrease in grain size near the edge of the puck. As a precaution, material was not used from near the edges of the pucks. Similarly, analysis of the EBSD data provides Figure 44, which shows the phase composition of each tile along the radius of the puck.
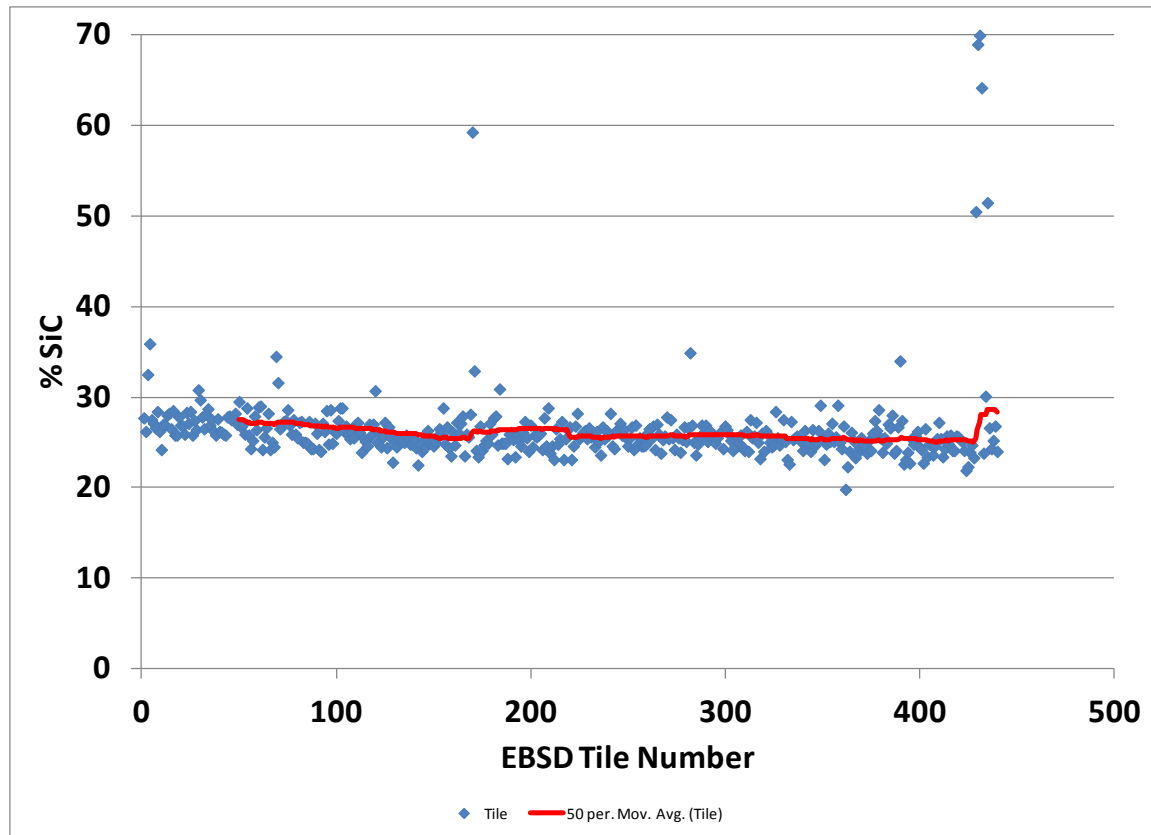
Figure 44: Percent SiC Content across a Puck of HfB$_2$-30% SiC Material

The phase composition data shows about a 3% decrease in SiC from the edge of the puck to the center. Once again, most of this difference seems to occur close to the edge of the puck, so material close to the edges was not used in this research. Additionally, there are several outlaying data points, which correspond with large conglomerates of SiC. Winder's work reported that such SiC conglomerates did not have an effect on strain rates [13]. From analysis of the EBSD data across the entire radius of a puck, it is expected that HfB$_2$ average grain sizes are within about 0.5 μm, and phase compositions of specimens cut from the same puck are consistent, no matter where they are cut from within the puck, except for near the edges.

Appendix B: Coefficients of Thermal Expansion

Since every creep test included an extensometer and heat up from laboratory temperature to 1500°C, coefficients of thermal expansion were conveniently determined for each specimen. This not only provided a validation of properly functioning equipment before each creep test, but an opportunity to assess whether there was any unusual behavior in the thermal strains of the research materials. Figure 45 shows a typical plot of the strain versus temperature data during the heat up from laboratory temperature to 1500°C, which generally took 1 hour.

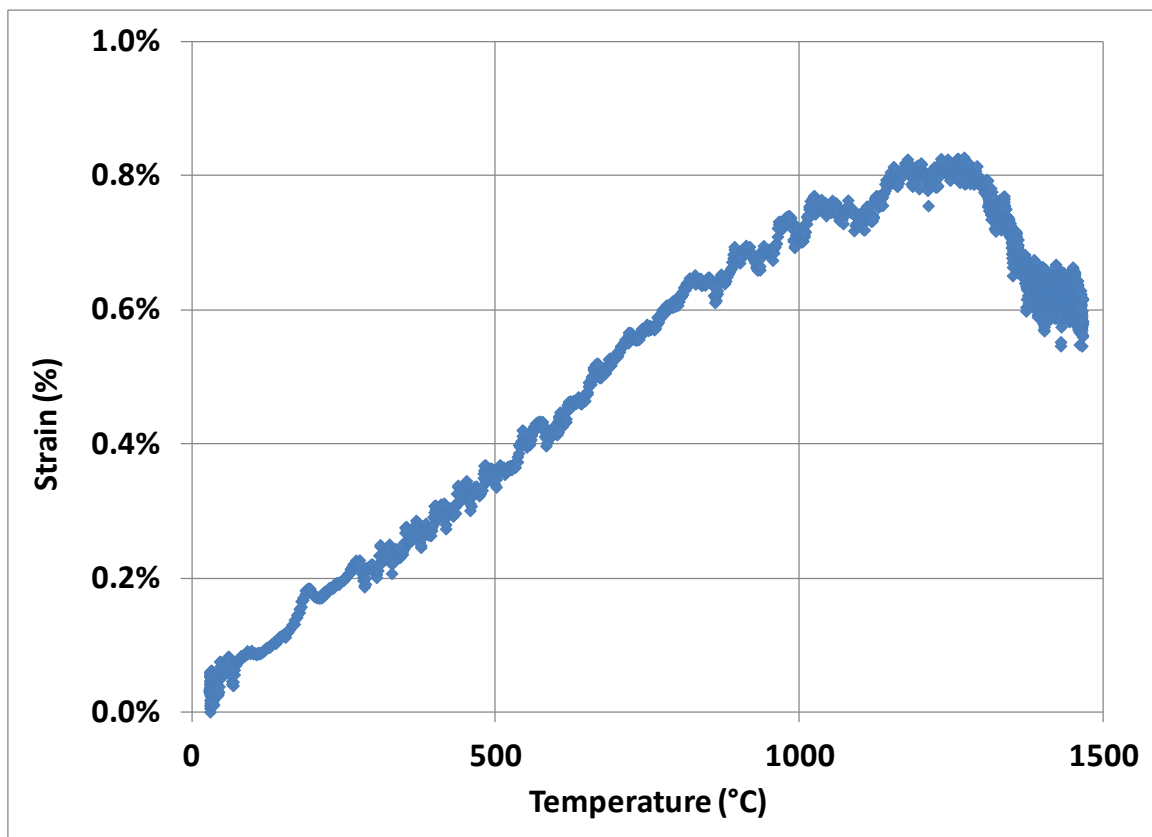**Figure 45: Strain vs Temperature during Heat Up of Specimen H20-2 in Argon**

A temperature soak of 1 hour generally occurred after reaching 1500°C, but that data is not included in Figure 45. The temperature soak ensured the materials reached equilibrium and the strain and temperature measurements were steady before applying the creep stress. This provided a clear distinction between the effects of heating and stress on strain, although a nominal compressive force of 50 pounds (i.e. about 5 MPa) was usually applied throughout the heat up and temperature soak in order to hold the specimen securely in place. This compressive force, as well as slower heating rates at the higher temperatures, contributed to the decrease in strain from about 1200°C, onward.

Coefficients of thermal expansion were derived from the strain versus temperature plots for each creep test and presented in Table 16. For consistency, the calculations generally relied on a linear, least squares fit of the data from 400 to 1000°C.

Table 16: Coefficients of Thermal Expansion for Each Creep Test Specimen

Specimen	Material HfB$_2$ -	Compressive Holding Load (lb$_f$)	Coefficient of Thermal Expansion (10^{-6} / °C)
H00-1	0% SiC	25	8.9
H00-4	0% SiC	50	9.3
H00-5	0% SiC	50	9.8
H10-1	10% SiC	50	8.9
H10-2	10% SiC	50	7.3
H10-3	10% SiC	50	7.5
H20-2	20% SiC	75	7.7
H20-3	20% SiC	50	7.0
H20-1	20% SiC	75	6.4
H30-5	30% SiC	50	7.7
H30-6	30% SiC	50	7.6
H30-4	30% SiC	50	8.7

Appendix C: Density Determination

The densities reported in the *Methodology* each came from a minimum of eight measurements, which were all in good agreement. As an example, specimen H20-4 from the HfB$_2$-20% SiC material was measured 26 times and the data presented in Figure 46. This provided a baseline for the precision of the utilized Archimedes technique and showed little variation, even between polished and unpolished specimens. The standard deviation of repeated measurements was 0.27%.
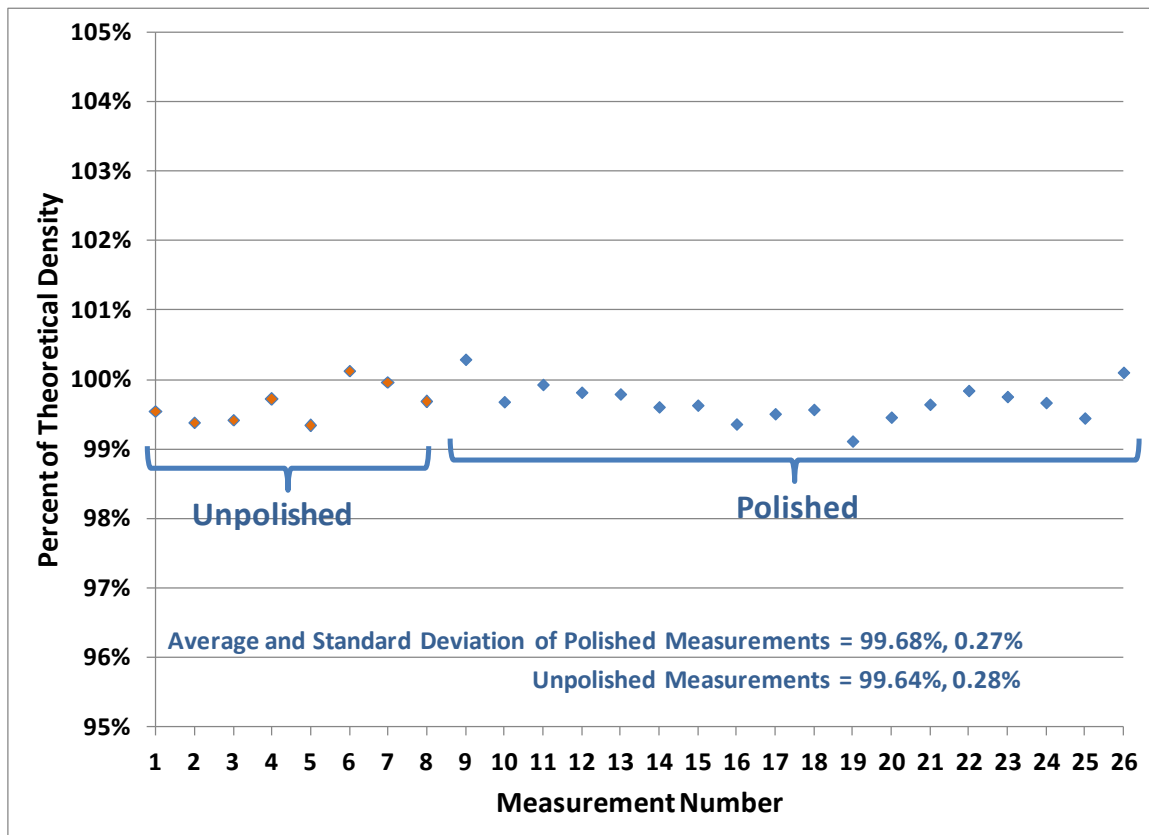
Figure 46: Repeated Archimedes Density Measurements for Specimen H20-4

Additionally, densities were found for each of the 18 HfB_2-20% SiC specimens, except for one, which had already been used. These specimens came from three different pucks, so the Figure 47 shows a typical variation between pucks of the same material and between specimens within the same puck. The standard deviation was only slightly higher than the standard deviation of repeated measurements, suggesting a small variation in the densities between pucks. These puck-to-puck variations are not a concern when comparing results from similar tests in this research, because similar tests used materials from the same pucks in this research. For example, all of the HfB_2-20% SiC creep test specimens came from the same puck, which was different from the puck used for the specimens in the stressed oxidation test. Puck-to-puck variations in density are assumed small when making comparisons between different tests in this research.
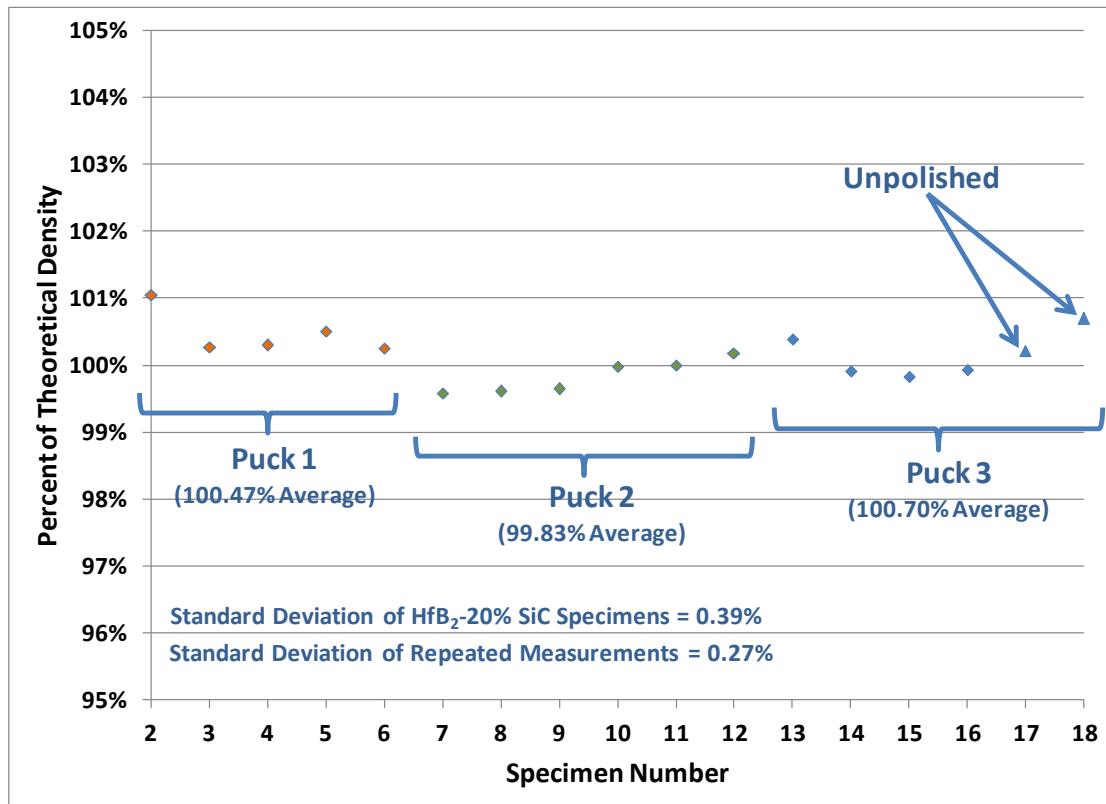
Figure 47: Archimedes Density Measurements for All HfB_2-20% SiC Specimens

Sometimes, the densities obtained slightly exceeded the theoretical densities. While some of this excess might be attributed to the variation in measurements, other authors have noted some important considerations. For example, Gasch concluded that SiC losses during hot pressing of HfB_2-20% SiC could account for observed densities 2% greater than the theoretical [51]. Carney identified the formation of HfC as another reason HfB_2-SiC materials might have higher than expected densities [103]. These phenomena were not specifically observed in this research, but they could have contributed to slight increases in densities. Figure 44 on page 138 suggests that the actual volume of SiC might be slightly lower than expected in the HfB_2-30% SiC materials used in this research. HfC and closed porosity were not observed during microstructural investigations. Though any of these factors, or combinations thereof, could have caused the slightly higher than theoretical densities, the variations have been shown to be small and densities close to theoretical.

Figure 48 shows the apparatus used for conducting the measurements to determine the densities via the Archimedes method. The scale was a Mettler AE 240, resting on a solid marble table. A universal specific gravity kit enabled the weight measurements in water. A thermometer and barometer provided the conditions for determining the density of water to use in the calculations.

Figure 48: Apparatus for Density Determination via the Archimedes Method

Appendix D: Impurities Investigation

The impurities investigation included three methods: Energy Dispersive X-ray Spectroscopy (EDS), Wavelength Dispersive X-ray Spectroscopy (WDS), and Glow Discharge Mass Spectrometry (GDMS). This three-pronged approach enabled the collection of reliable and affordable information about the impurities in all four compositions of the research materials and validation of the methods. In summary, no impurities were found in the pre- or post-test research materials that were suspected of having affecting the analysis or conclusions of this research effort.

The EDS method was primarily utilized to qualitatively identify the presence of impurities in specific locations and assess relative quantities. Such results were most convenient to obtain, used often in conjunction with SEM imaging, and presented and discussed throughout this paper. This appendix only presents the EDS results related to the post-test impurities investigation. The purpose of this investigation was to determine whether the research materials acquired impurities during the creep tests in argon. Winder's work [13] was crucial to the development of an experimental setup that mitigates undesirable chemical reactions during high temperature creep testing of the research materials in air, but this work's testing was performed in argon. Thus, it is prudent to verify that materials inside the furnace, such as platinum and yttrium aluminum garnet (YAG), did not contaminate the research materials during testing. This was accomplished in two parts. First, SEM imaging was used to search large areas of the post-test research material for any irregularities. This included close looks at grain boundaries, triple points, and oxide scales. EDS was then used to identify the elemental

composition of irregularities. Second, standardless EDS spectra were collected from representative 1 mm by 1 mm areas of the pre- and post-test research materials, interior and near to the surface, for long periods of time. This provided higher counts and improved confidence. EDS spectra were collected at 20 kV to ensure responses could be excited for all desired elements and at 5 kV to provide higher resolution information at the lower energy levels. Then, all peaks in the EDS spectra of the post-test materials were identified and compared to results from the pre-test materials.

No significant differences were observed in the EDS results of the pre- and post-test research materials. Small oxygen and zirconium peaks were always noticeable. The automated quantification software consistently reported about 0.1% and 0.3% zirconium by atomic percentage in the SiC-containing and HfB_2-0% SiC materials, respectively. 1% oxygen was consistently reported in all of the pre- and post-test materials. The location of the oxygen K_α peak is marked by a green line in the following figure. Visually, the silicon K_α peak overlaps with the hafnium M_α peak. Working with overlaps was facilitated by the analysis at 5 kV and the automated software. Traces of copper were detected in the post-test HfB_2-0% SiC material, and traces of iron were detected in the pre-test HfB_2-10% SiC material. Traces of both of these elements were also found in the WDS and GDMS investigations. Sometimes, aluminum and other suspected traces were manually added to the EDS analysis software, but never registered quantities. In all cases, the trace amounts were not expected to affect the results, and post-test microstructural observations did not show any irregularities. As an example, Figure 49 provides the EDS spectra collected at 20 kV for the HfB_2-10% SiC pre- and post-test materials.
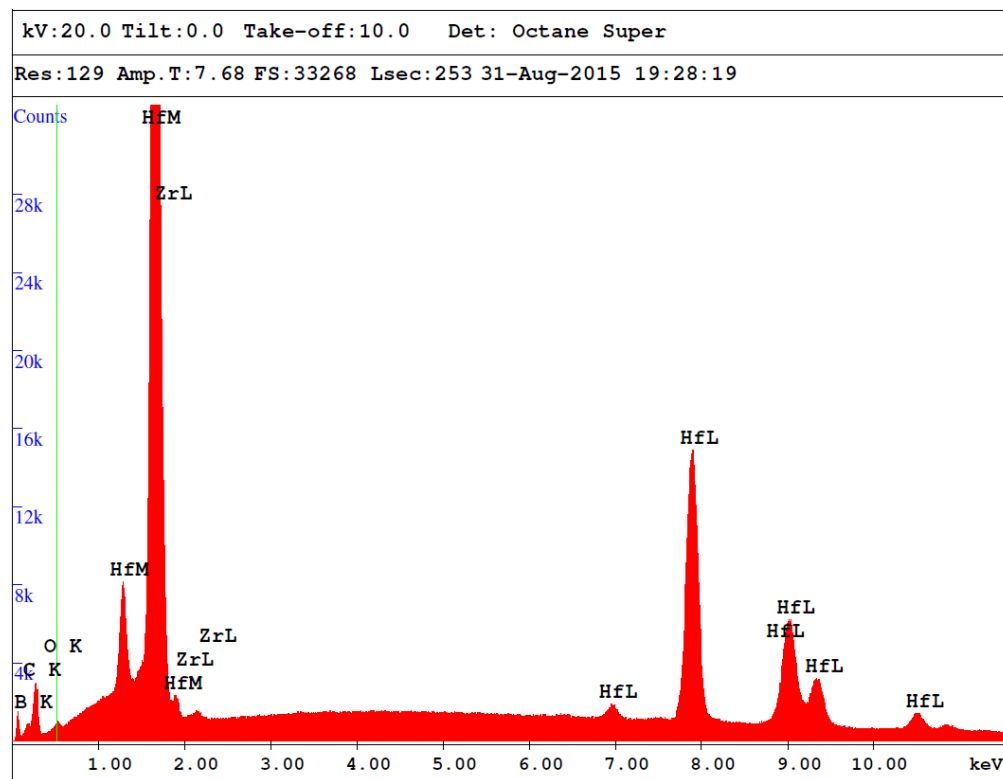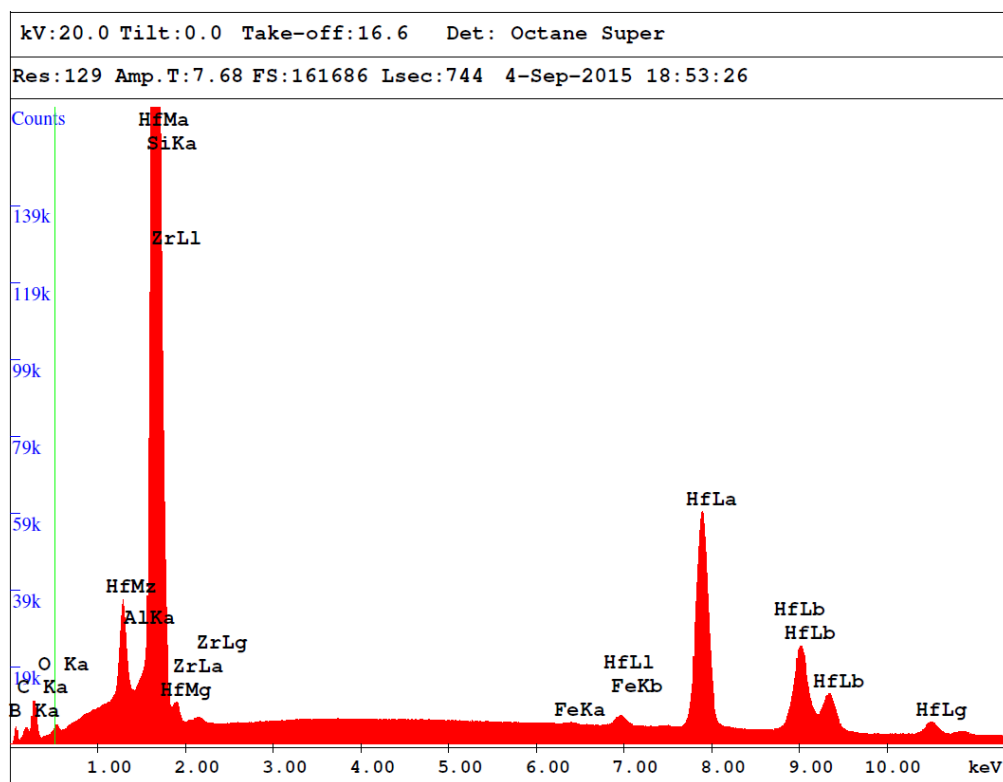
Figure 49: EDS Spectra Collected at 20 kV for the HfB$_2$-10% SiC Materials Pre-test (Top) and Post-test (Bottom)

147

The WDS method was utilized for similar purposes as EDS. However, due to its more involved processes, WDS was only used on one occasion to search for impurities in the pre-test HfB_2-30% SiC research material and determine weight percentages for seven selected elements in all four research materials. The HfB_2-30% SiC material was chosen for the WDS impurities search, because it was the only research material not examined by the GDMS method. For the HfB_2-30% SiC research material, the Cameca SX-100 Electron Probe Microanalyzer scanned through its full range of wavelengths and provided WDS spectra for each of its crystals. These spectra were analyzed and eleven elements were clearly identified. Seven of these elements were selected for quantification in all four research materials. Lithium fluoride crystals were used for Cu, Hf, and Ta, and thallium acid phthalate crystals were used for Al, Si, Zr, and W. Four elements were identified, but excluded from the analysis: B, C, O, and Fe. The electron probe microanalyzer was run at 15 kV and 50 nA over a 280 μm by 280 μm representative area with 20 μm step sizes. Thus, data from 225 points were collected on each of the four research materials. Table 17 presents the results in terms of atomic percentage, where B and C were added by stoichiometry with Hf/Zr and Si, respectively.

Table 17: Quantification of 9 Elements in the Pre-Test Research Materials via WDS
(all values in atomic percent)

	HfB$_2$ – 0% SiC	HfB$_2$ – 10% SiC	HfB$_2$ – 20% SiC	HfB$_2$ – 30% SiC
B	66.396	59.194	50.059	40.407
Hf	31.156	28.765	24.411	19.645
C	0.027	5.437	12.318	19.577
Si	0.027	5.437	12.318	19.577
Zr	2.042	0.832	0.618	0.559
Ta	0.309	0.281	0.238	0.193
Al	0.006	0.069	0.148	0.090
Cu	0.044	0.052	0.032	0.027
W	0.000	0.002	0.005	0.016
Total	100.00	100.00	100.00	100.00

For the most part, the WDS results were consistent with the GDMS results. WDS identified Zr, Al, Fe, W, and Cu as impurities, which were also among the highest impurities identified via GDMS. WDS results seem to indicate a much higher Zr content than GDMS, however, the WDS results for Zr are most likely high. A highly pure Hf standard was not available for WDS calibration and, instead, relied upon a Hf standard with a reported content of 1.65% Zr by weight. Additionally, analysis of the Hf standard via WDS consistently resulted in a quantification of about 5% Zr by weight. Thus, it is reasonable to assume that the research materials contained less Zr than the standard, which is consistent with the GDMS results. Both methods also showed more Zr in the HfB$_2$-0% SiC material than the SiC-containing materials. This is attributed to the fact

that the HfB_2 powders used to make the HfB_2-0% SiC material came from a different source, which reported 2.5% Zr by weight. Si and C in the HfB_2-0% SiC material is assumed to come primarily from the ball milling process. Overall, the WDS analysis appears consistent with the GDMS analysis and shows that the HfB_2-30% SiC material should be considered as good as the other SiC-containing materials.

The GDMS method was only utilized for an impurities investigation of the pre-test HfB_2-0%, -10%, and -20% SiC research materials. The summarized results and discussion are presented in the *Methodology* starting on page 63. In this appendix, the full results are simply presented in Table 18 as they were received from the disinterested GDMS service provider. King provides a very nice, general description of the GDMS method [119]. The service provider typically uses argon as the discharge gas and collects data from a 50 to 80 mm^2 area.

Table 18: Glow Discharge Mass Spectrometry of the Research Materials

(all values in ppm weight unless otherwise noted)

	HfB$_2$ – 0% SiC	HfB$_2$ – 10% SiC	HfB$_2$ – 20% SiC		HfB$_2$ – 0% SiC	HfB$_2$ – 10% SiC	HfB$_2$ – 20% SiC		HfB$_2$ – 0% SiC	HfB$_2$ – 10% SiC	HfB$_2$ – 20% SiC
Li	< 0.01	< 0.01	0.04	Ge	< 0.1	0.23	< 0.1	Nd	0.07	< 0.05	< 0.05
Be	< 0.01	< 0.01	< 0.01	As	< 0.05	< 0.05	< 0.05	Sm	< 0.05	< 0.05	< 0.05
B	Matrix	Matrix	Matrix	Se	< 0.1	< 0.5	< 0.5	Eu	< 0.05	< 0.05	< 0.05
C	=< 3500	Matrix	Matrix	Br	< 0.5	< 0.5	< 0.5	Gd	< 0.05	< 0.05	< 0.05
F	< 0.5	< 0.5	< 0.5	Rb	< 0.05	< 0.05	< 0.05	Tb	< 0.05	< 0.05	< 0.05
Na	0.14	0.46	1.2	Sr	0.59	0.36	0.37	Dy	< 0.05	< 0.05	< 0.05
Mg	0.15	11	14	Y	6	1.5	0.62	Ho	< 0.05	< 0.05	< 0.05
Al	8.4	600	810	Zr	~ 0.78 wt%	0.18 wt%	0.27 wt%	Er	< 0.05	< 0.05	< 0.05
Si	Matrix	Matrix	Matrix	Nb	1.3	0.77	0.27	Tm	< 0.05	< 0.05	< 0.05
P	0.42	3	2.4	Mo	9.8	1.7	1.4	Yb	< 0.05	0.36	0.16
S	0.14	0.34	0.06	Ru	0.66	< 0.05	0.33	Lu	< 0.05	< 0.05	< 0.05
Cl	~ 2	1.4	~ 0.2	Rh	0.45	0.08	0.09	Hf	Matrix	Matrix	Matrix
K	0.16	0.68	0.54	Pd	=< 5	0.28	0.25	Ta	=< 220	=< 7	< 5
Ca	6.9	56	36	Ag	0.08	0.32	0.5	W	510	3.8	0.74
Sc	=< 1	=< 0.6	=< 0.8	Cd	< 0.5	< 0.1	< 0.1	Re	0.54	< 0.1	0.18
Ti	120	13	12	In	Binder	Binder	Binder	Os	110	0.68	24
V	5.8	6.3	9.8	Sn	0.19	< 0.1	< 0.1	Ir	< 5	< 10	< 10
Cr	180	18	8.6	Sb	< 0.1	< 0.1	< 0.1	Pt	< 10	< 10	< 10
Mn	7.2	1.5	2.4	Te	< 0.05	< 0.05	< 0.05	Au	< 20	< 20	< 20
Fe	990	330	180	I	< 0.05	< 0.05	< 0.05	Hg	< 10	< 10	< 10
Co	37	3.7	2.6	Cs	< 0.5	< 0.5	< 0.5	Tl	< 5	< 5	< 5
Ni	40	14	6.3	Ba	0.62	0.95	2.3	Pb	< 5	< 5	< 5
Cu	0.65	30	0.49	La	39	0.35	0.46	Bi	< 0.5	< 0.5	< 0.5
Zn	< 0.1	0.49	0.25	Ce	0.46	0.3	0.96	Th	0.02	0.008	0.03
Ga	< 0.1	< 0.1	< 0.1	Pr	0.25	< 0.1	< 0.1	U	120	0.23	0.29

Appendix E: Test Procedures

PRE-TEST

Specimen

- Select specimen, YAG rods, alumina spacers, temperature, stress, and argon or air for test
- Weigh, measure (micrometer and optical), and photo specimen
- Calculate load required for desired stress

MTS Station

- If MTS Station Manager needs to be opened, select "Temperature.cfg" and desired parameters
- Select "New Specimen" on MTS Station Manager, enter specimen name, and hit <ENTER>
- Reset and edit procedure Creep.000 (load, temp, displacement limit detector values) and Save
- Check to ensure heating element leads are clear of metal-to-metal contact with the furnace
- Power on Eurotherm controller, then MTS and grip hydraulic power
- Clear MTS Station Manager limit detectors, reset/override if needed, and start hydro
- Start function generator (1 Hz, 1 mm sine wave near centerline of furnace)
- Stop function generator after a minimum of 30 minutes; check for good responses

Alignment

- Wrap steel shims around alignment rod
- Insert alignment rod into custom grips, then insert assembly into MTS grips and close grips
- Ensure alignment rod is still free to move (i.e. not loaded)
- Raise top crosshead, remove alignment rod
- Measure and inspect YAG rods
- Wrap YAG rods with copper shims and insert into custom grips; secure top YAG rod w/4 screws
- Bring YAG rods together to verify alignment; repeat alignment procedure if not aligned
- Lower bottom crosshead, place wrap around soft insulation thru bottom YAG rod, raise crosshead
- Cut 2 pieces of Pt foil to size of an alumina spacer
- Stack 1 piece of Pt and 2 spacers on top of bottom YAG rod, Pt down; center specimen on top
- Zero force, then stack 2 spacers and 1 piece of Pt on top of specimen, Pt up
- Adjust stack until everything appears to be perfectly aligned
- Lower top crosshead until close, but do not contact stack; lock top crosshead
- If specimen appears to be in a good position, zero displacement, set values for displacement limit detectors on MTS Station Manager, and activate for Program Hold Interlock (nominally +7/-3 mm)
- Raise bottom crosshead in 0.1 mm intervals until -10 lb_f; switch to force control and go to -50 lb_f
- Verify alignment; repeat alignment procedure if not aligned; zero displacement
- Inspect extensometer rods and replace if necessary
- Test extensometer on specimen; adjust rods as necessary; error closer to topside of support arm
- Zero strain; remove extensometer

<u>PRE-TEST</u> (continued)

Insulation

- Slide furnace forward and secure; insert pie piece
- Place insulation around bottom YAG rod, between wrap around and furnace, to plug lower hole
- Wrap up wrap around soft insulation; secure with weight bar
- Place top soft insulation; secure with weights
- Support bottom of wrap around soft insulation with braces
- Place side soft insulation x2
- Place extensometer; verify strain reading should be near zero with appropriate noise levels; zero strain

Argon (if required)

- Power on mass flow controller and verify it's set to zero flow and argon gas
- Record argon dewar/cylinder gas pressure
- Open dewar/cylinder gas valve; open regulator valve to mass flow controller; record pressures
- Set mass flow controller to 10 SLPM; check for flow; ensure no leak between feeding tubes and hoses
- Insert argon feeding tubes x2 and secure in place
- After 20 minutes, turn mass flow controller down to 3 SLPM

Heat

- Loosen screws on top custom holder
- Turn on coolant to grips; ensure chiller is filled with distilled water
- Turn on heating element cooling fans and cooling air for extensometer
- Start procedure "Creep.000" (starts heat up and displays "Start", "End", and "ABORT" test buttons)
- Record lab temperature, relative humidity, and anytime the temperature goes into or out of limits
- When furnace begins to glow, visually verify the specimen and extensometer are in good position
- After reaching target temperature, wait for 1 hour of temperature soak
- Verify temperature and strain readings are steady before proceeding with Load

Load

- Verify good thermal strain; verify temperature and strain are stable and within limits
- Select "Start Test" button (loads up to desired load)

DURING TEST (at least every hour)

- Check to ensure extensometer is clear of obstacles
- Check temperature, mass flow controller, and force values
- Check to ensure displacement is not too close to limit detector values
- Record strain, displacement, argon pressures, and time

POST-TEST

- "End Test" button (commands -50 N and 0°C)
- Increase argon flow rate if faster cooling desired
- Wait until 100°C, then look and note position of extensometer on specimen and support arm
- Remove top and side soft insulations; raise topside of wrap around insulation
- Photo specimen through top hole; remove extensometer and note condition
- Remove argon feeding tubes
- Tighten screws on top custom holder
- Remove pie piece; photo specimen; "Release Specimen" button, switch to displacement control
- Lower bottom crosshead in 0.1 mm intervals until there's clearance to remove specimen
- Remove, photo, and secure specimen
- Set flow controller to zero, close regulator valve, then power down controller; close dewar valve
- Power down grip coolant, hydro on MTS Station Manager, Eurotherm controller, and grip coolant
- Remove bottom supports and wrap around
- Push back furnace and secure
- If required, remove top and bottom custom grips and power down hydro for grips
- If required, remove YAG rods from custom holders and turn in for repair if reparable
- Copy and analyze data from MTS computer
- Weigh and measure specimen; assess oxide scale and thickness

Appendix F: Nonlinear Least Squares Fit of Burger's Model

Sometimes, when creep tests ended prematurely, it was difficult to determine whether the secondary creep rate had been reached. In these situations, an objective method was helpful in determining whether the secondary creep rate had been observed or at least a creep rate close to the secondary creep rate. In the course of this research, the chosen method involved a nonlinear, least-squares fit of Burger's model. Of course, choosing such a method, or any method for that matter, involves assumptions. While this effort chose to focus on experimental research and not dive too deeply into theoretical discussions, it is still very much concerned with publishing good data. Thus, the model was only utilized if it appeared to be a good fit to the actual data. If the fit was good, the derivative of the model was taken and the limit determined as time went to infinity. This provided an idea of how much the creep rate might have decreased if the test had continued. Of course, since this fit of the creep rate is based on a generalized constitutive model, it is far from a guarantee that the creep rate would have continued to fit the model after the data collection stopped, even if it was a good fit up to that point. However, this research proposes that it is a good tool to use, in appropriate situations, to show whether the secondary creep rate had been reached.

First, the model selected for use in this research was Burger's model as described in Shames [61]. Burger's model consists of a Maxwell and Kelvin component in series, which might also be described as a parallel spring and dampener in series with a spring and dampener in series. For the purpose of this effort, the constitutive equation and

155

coefficients were simplified and strain was expressed with Equation 32, where ε

represents strain, t represents time, and a, b, c, and d are coefficients.

$$\varepsilon = a\,e^{-bt} + c\,t + d \qquad (32)$$

MATLAB was used to provide a nonlinear, least squares fit of this model to the

data. If the fitted model was a good fit, the derivative of the fitted model would be taken

to arrive at a model for the strain rate, Equation 33.

$$\dot{\varepsilon} = -a\,b\,e^{-bt} + c \qquad (33)$$

The actual strain data was smoothed and the derivative taken numerically, so that the

strain rate as function of time could be compared between the data and the model. If the

strain rate model appeared to be a good fit, MATLAB was also used to project a

minimum creep rate by taking the limit of Equation 33 as time went to infinity, arriving

at Equation 34.

$$\dot{\varepsilon}_{minimum} = \lim_{t\to\infty} -a\,b\,e^{-bt} + c \qquad (34)$$

As examples of how this process was used in this research, examples are provided from the creep tests performed at 50 MPa on the HfB$_2$-10% and -20% SiC materials. Typically, the MATLAB script that implemented this process was used during creep tests to quickly verify whether a steady creep rate had been reached or if testing should continue. Unfortunately, the 50 MPa creep tests for the HfB$_2$-10% and -20% SiC materials ended prematurely due to spacer failure. Thus, the option was not available to continue testing.

First, a look at the strain data from the HfB$_2$-10% SiC creep test shows that Burger's model fit very well to the data (reference Figure 50).
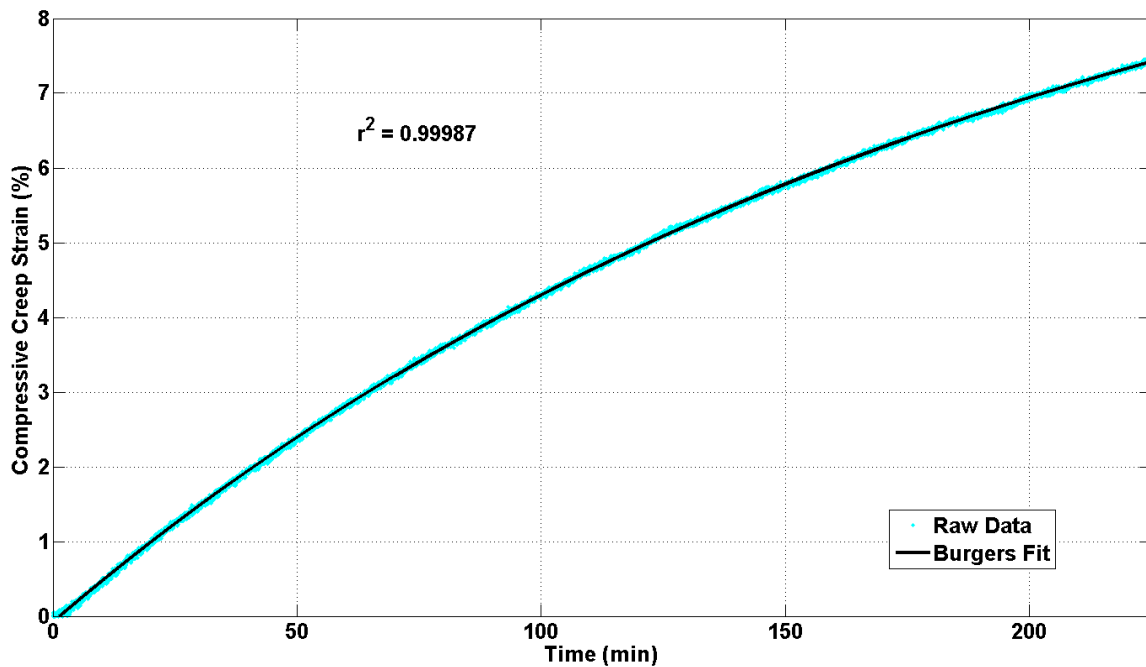

**Figure 50: Creep Strain vs Time with Burger's Fit
for HfB$_2$-10% SiC at 50 MPa and 1500°C in Argon**

Then, the strain data was differentiated and smoothed and compared to the strain rate

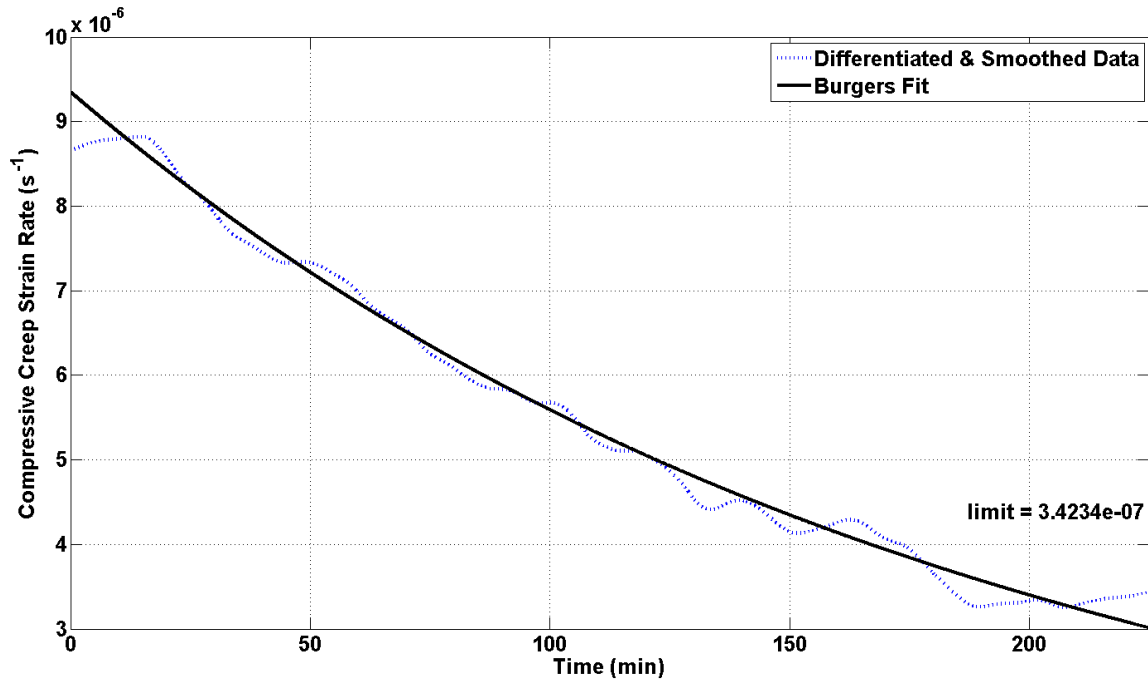model. As seen in Figure 51, the strain rate model also provided a good fit.

**Figure 51: Creep Rate vs Time with Burger's Fit
for HfB$_2$-10% SiC at 50 MPa and 1500°C in Argon**

From the magnitude and direction of the fitted curve in Figure 51, especially towards the

end of the data around 225 minutes, it appears that the strain rate probably would have

continued to decrease if the test had continued, and maybe by as much as an order of

magnitude according to the limit. However, it does not imply that the data is not useful,

as there are other characteristics of the creep test data that are still useful, especially when

put in perspective with other information, such as was done in the *Analysis and Results*

section of this research. It is also interesting to note that there appears to be a sudden

leveling off of the differentiated and smoothed data in the last 50 minutes, which is not

158

apparent from looking at only the fitted curve. Would the creep rate have continued to decrease if the test had not ended prematurely? Did some kind of transition in the creep mechanisms suddenly happen, towards the end of the test, and a minimum creep rate was attained? Obviously, more data would have been desired, but this example illustrates how this process might be used as a tool for looking at creep rates in experimental data as a function of time and highlights the importance of putting the results of such a process in perspective with other important information from the research.

A look at the HfB_2-20% SiC creep test also shows that Burger's model fit very well to the data in terms of both strain (Figure 52) and strain rate (Figure 53), although the r^2 value appears low. The low r^2 value is a natural consequence of working with combinations of relatively high noise, low slopes, and short test durations sometimes experienced in this research.
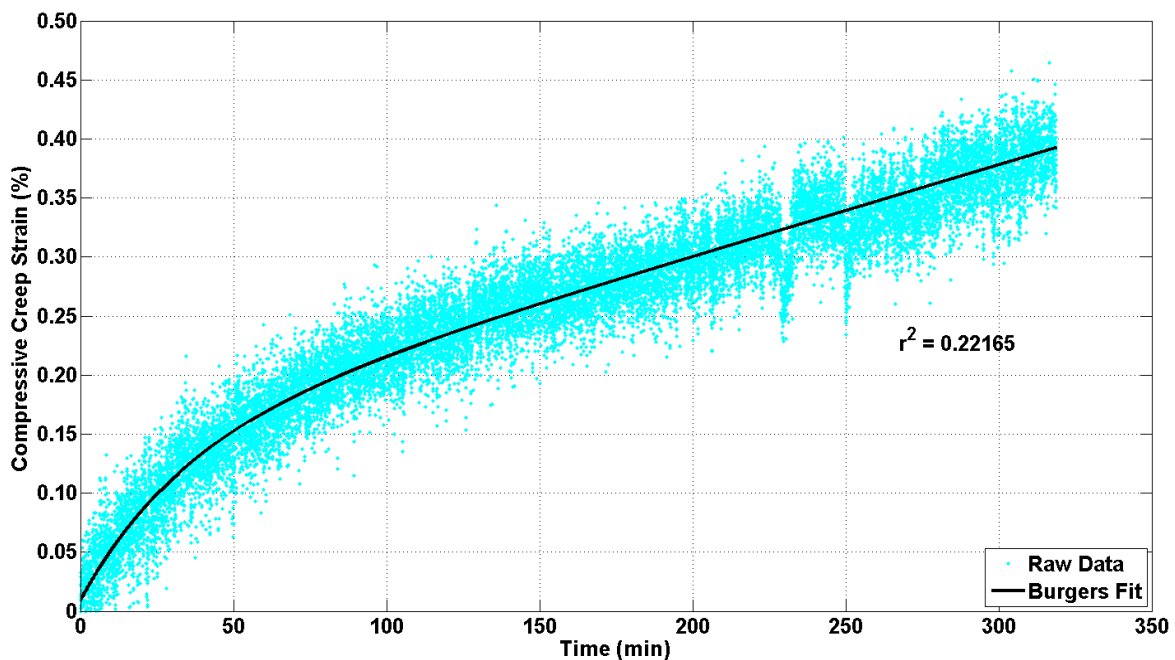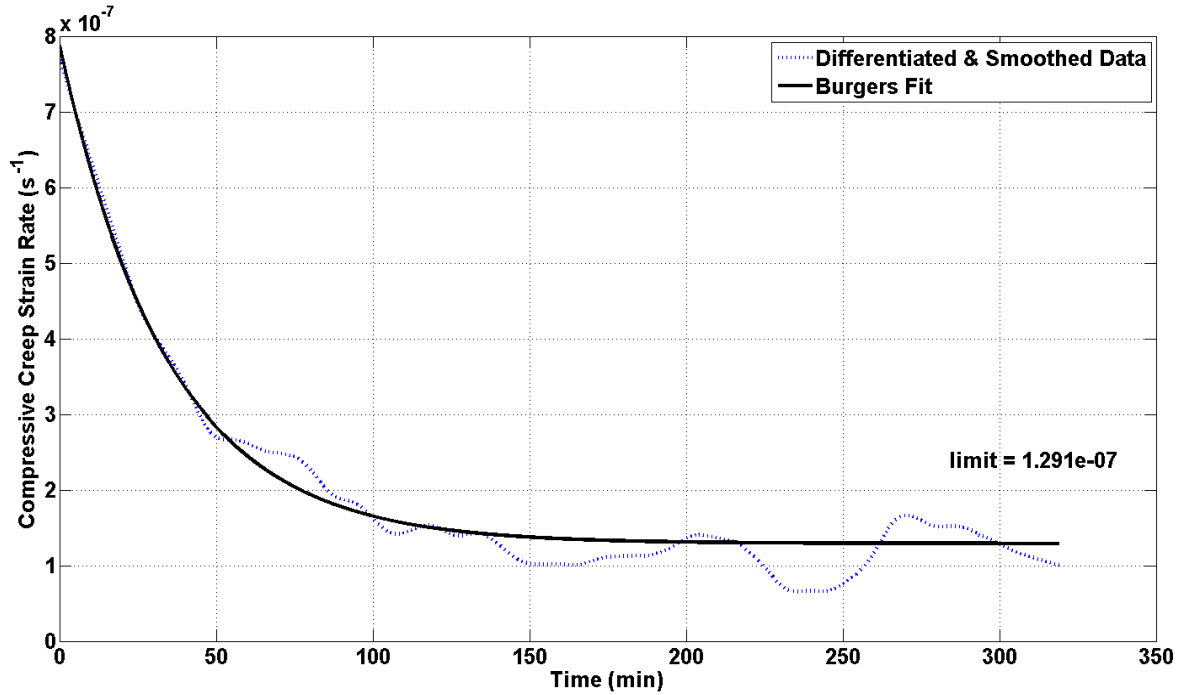

**Figure 52: Creep Strain vs Time with Burger's Fit
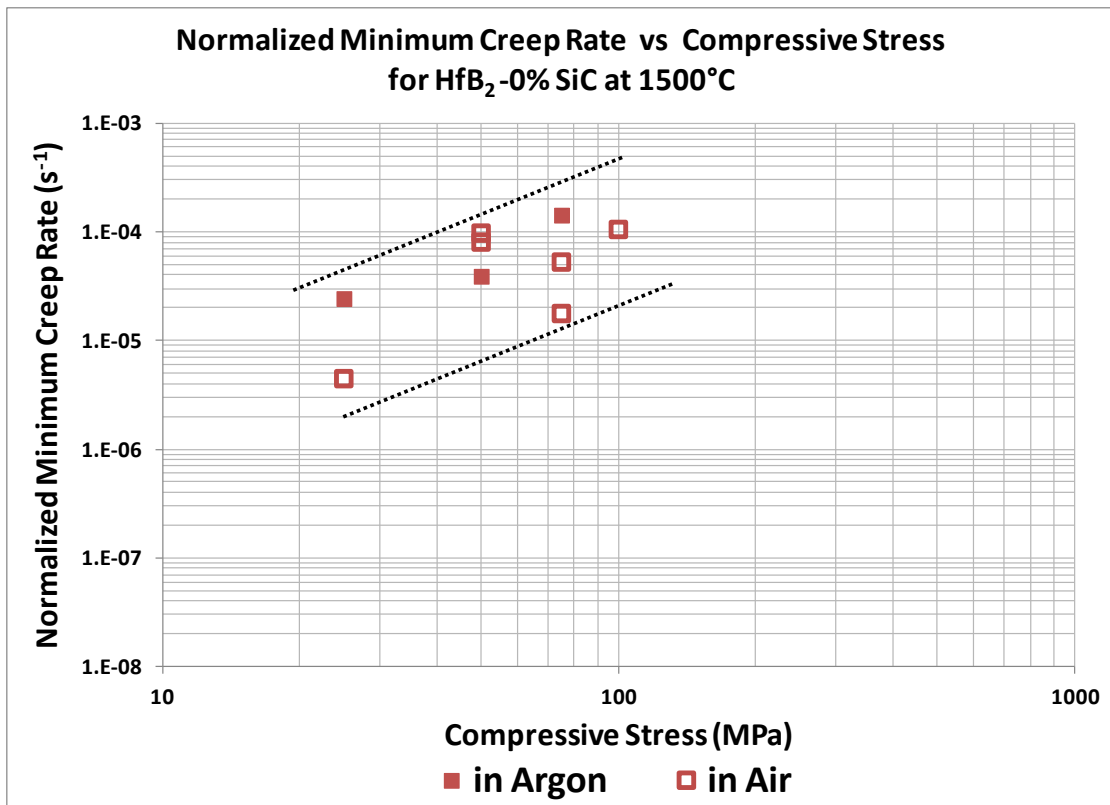for HfB_2-20% SiC at 50 MPa and 1500°C in Argon**

**Figure 53: Creep Rate vs Time with Burger's Fit
for HfB$_2$-20% SiC at 50 MPa and 1500°C in Argon**

Compared to the HfB$_2$-10% SiC material, the creep rate curves for the HfB$_2$-20% SiC

material paint a different picture. With these curves, it seems apparent that the creep rate

in Figure 53 had bottomed out near a minimum value for at least the last couple hours of

testing. Additionally, the limit of Equation 33 as time goes to infinity suggests that the

minimum creep rate probably would not have changed by more than 2x10^{-8} s^{-1}, even if

the creep test was continued for a very long time. As previously mentioned, there is no

guarantee that the creep rate would have continued to fit the model after the data

collection stopped, but this process has proven to be a very useful tool in terms of

confidently showing whether a secondary creep rate had been reached, or a value close

enough for the research's purposes, or if creep testing should have continued.

160

Appendix G: A Comparison of Minimum Creep Rates in Argon and Air

Figure 54 and Figure 55 provide a breakdown of the analysis presented in Figure 30 on page 109 in section 4.5, pertaining to the effects of oxidation on creep. Figure 30 plotted minimum creep rates versus stress for HfB_2-0% and -20% SiC at 1500°C in argon and air. The minimum creep rates in argon and air came from this research and Winder's work, respectively, and were normalized to a grain size of 1 μm. However, trendlines were only provided for the two materials. Figure 54 and Figure 55 provide separate charts for the creep experiments in argon and air. These figures were considered and relevant discussions included in section 4.5 starting on page 107.

First, Figure 54 presents the results for HfB_2-0% SiC in argon and air, normalized to a 1 μm grain size. The dashed lines are provided as visual references and are based on the results in air (i.e. they bound the results using lines with the same slope as a power law fit of the data). The results in argon are within those bounds. Any calculations that show a difference in the results based on environment would not carry much statistical significance. For example, a power law fit of these results would show slightly lower stress exponents in argon and slightly higher creep rates than in air. However, these differences are small compared to the scatter in the experimental data. Thus, any conclusions regarding the results, attributed to differences in environment, would be suspect, given the scatter in the experimental data.

**Figure 54: Normalized Minimum Creep Rate vs Compressive Stress
for HfB₂-0% SiC at 1500°C in Argon and Air
Data in Air from Winder [13]**

162

Second, Figure 55 presents the results for HfB$_2$-20% SiC in argon and air, normalized to a 1 μm grain size. The dashed lines are provided as in the previous figure. The results in argon are again within those bounds, and any calculations that show a difference in the results based on environment would not carry much statistical significance. Thus, any conclusions regarding the results, attributed to differences in environment, would be suspect, given the scatter in the experimental data.

**Figure 55: Normalized Minimum Creep Rate vs Compressive Stress
for HfB$_2$-20% SiC at 1500°C in Argon and Air
Data in Air from Winder** [13]

Appendix H: Experimental Investigation of HfB$_2$-SiC Oxidation Behavior in Air

This appendix provides important information regarding the oxidation behavior of the research materials at 1500°C in a controlled, air environment, independent from the experimental setup used to conduct the stressed oxidation tests.   The results enable an assessment of whether the experimental setup and/or the heating cycles of the stressed oxidation test affect the analysis of oxidation behavior. Additionally, the results provide an unprecedented look at the oxide scale thicknesses of the research materials at several time intervals in a continuous experiment. Up to this point, the experimental data in the literature only provides snapshots at specific durations. A continuous picture thus requires the compilation of data from several experiments, thereby introducing other factors, such as variations in experimental setups, methods, temperatures, material compositions, and microstructure. Finally, the results of this investigation provide a baseline for oxidation behavior, which enable clear comparisons to experimental and modeled results found in the literature and in this research effort. The remainder of this appendix focuses on the experimental setup, method, materials, and results of the baseline oxidation tests, as well as additional analysis not included in the main body of this work.

Material: Baseline oxidation tests were conducted separately using two specimens each of HfB$_2$-0% and -20% SiC. The specimens were produced as described in the *Methodology*, but came from different pucks than those used in the creep and stressed oxidation tests. A precision diamond saw cut each specimen into six sections,

164

and the cut ends were polished in accordance with the *Methodology*, so that all sides were of the same finish. Thus, 12 coupons of each material were fashioned with similar geometries from the same lot of material and placed into a box furnace, with each coupon resting on an alumina spacer, consistent with the creep and stressed oxidation tests conducted in this research (reference Figure 56). One coupon was retained in the prepared condition and not heat treated.
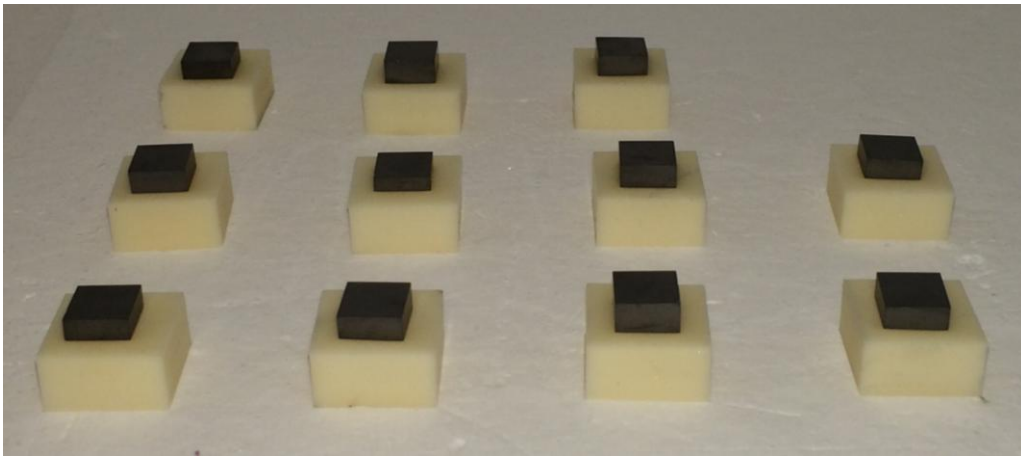

Figure 56: HfB$_2$-20% SiC Coupons prior to Baseline Oxidation Test

Experiment: The box furnace, pictured in Figure 57 and manufactured by Blue M, included a temperature controller and was burned out for 1 hour at 1600°C prior to the tests. Laboratory air was allowed to naturally circulate in and out of the furnace through several small openings, which was nominally 70°F and 53% relative humidity.

Figure 57: Blue M Box Furnace Used in Baseline Oxidation Tests

The baseline oxidation tests began by placing all 11 coupons in the box furnace at room temperature. The temperature then ramped up to 1500°C at 20°C per minute and was held for 90 hours. During the 90 hours, at the desired time intervals, the box furnace door was quickly opened, a coupon removed, and the door closed. Coupon extractions took less than 15 seconds and resulted in momentary temperature drops of 200°C for the remaining specimens, which recovered to 1500°C in less than 3 minutes. Temperatures were monitored and recorded by two B-type thermocouples, inserted into the top of the box furnace and positioned above the coupons in the open space of the box furnace. In the before and after photographs of the HfB_2-20% SiC coupons in Figure 58, the specimen numbers 1 through 12 correspond, respectively, to the durations held at temperature of 0.5, 1, 2, 3, 6, 9, 12, 15, 30, 45, 90, and 0 hours.
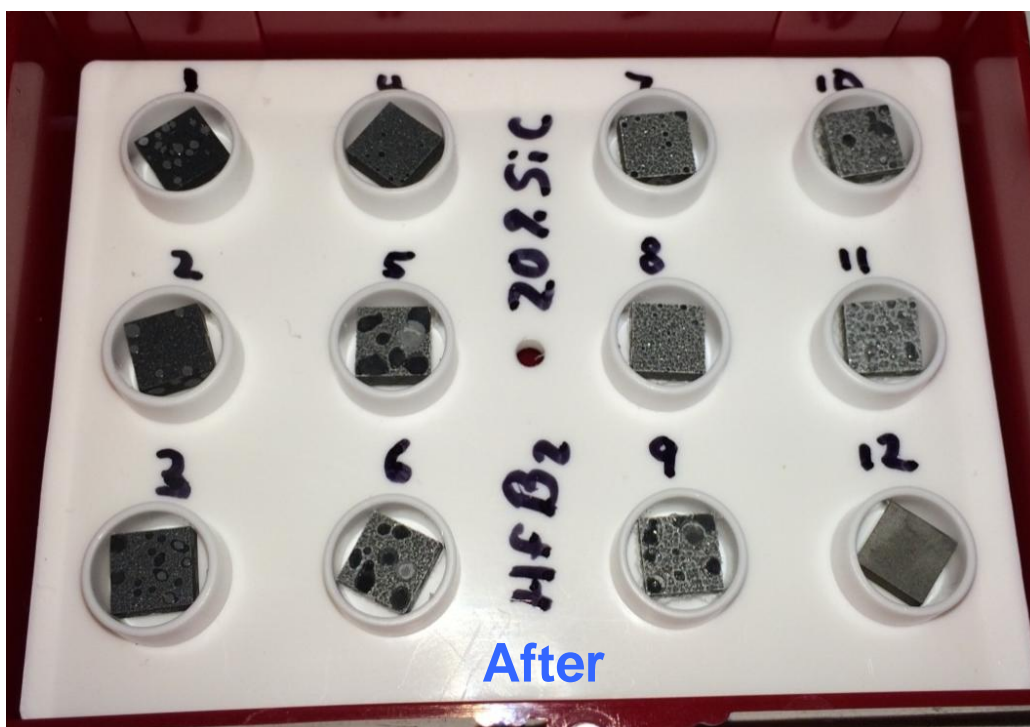
Figure 58: HfB₂-20% SiC Coupons before and after the Baseline Oxidation Test

After rapid cooling to room temperature, the coupons were mounted, and a diamond grinding disc removed the top layers to expose the cross sections as in Figure 59. Diamond slurries polished the cross sections down to 1 μm, which were then carbon coated and analyzed with SEM and EDS techniques described in the *Methodology*.
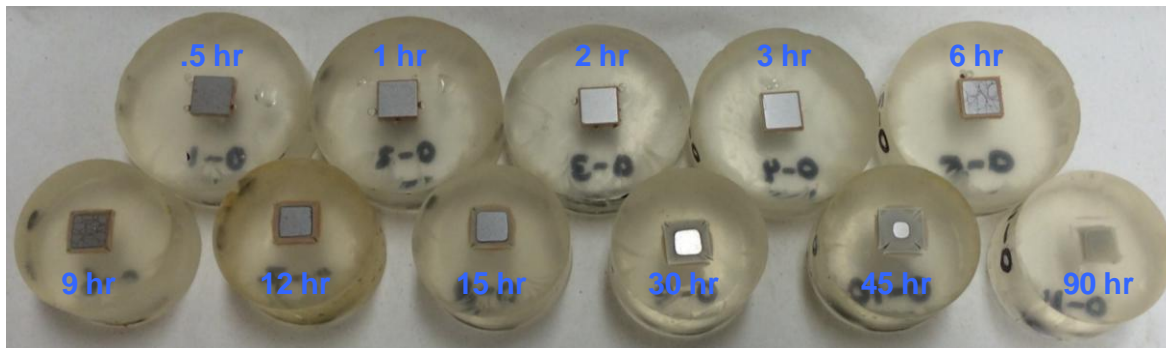

Figure 59: HfB$_2$-0% SiC Coupons after Heat Treating, Mounting, and Polishing

Results: The baseline oxidation tests of the HfB$_2$-0% and -20% SiC coupons proceeded successfully as outlined in the previous section. However, Figure 59 clearly shows that the amount of oxidation in the HfB$_2$-0% SiC coupons became so great, relative to the coupon size, that other effects might have been introduced beyond 6 hours, as evidenced by corner cracks in the oxide layer after 6 hours and complete oxidation of the coupon by 90 hours. Cracks in the parent material of the 6-, 9-, and 12-hour coupons stopped at the oxide layer and did not exhibit oxidation, suggesting the cracks occurred during the rapid cool down from 1500°C to room temperature. More discussion on this topic is presented in the next section. Table 19 provides results of the baseline oxidation tests for the HfB$_2$-0% and -20% SiC materials, and Figure 60 shows example SEM images of the oxide scales of the HfB$_2$-20% SiC coupons at 1,500X magnification.

168

Table 19: Results of the Baseline Oxidation Tests

Coupon (HfB₂-0% SiC)	Time at Temp (h)	Pre Weight (g)	Post Weight (g)	Number of Oxide Scale Thickness Measurements	Average (μm)	Standard Deviation (μm)	Minimum (μm)	Maximum (μm)
1	0.5	1.3468	1.3528	59	88	9	65	108
2	1	1.6344	1.6440	60	148	10	133	175
3	2	1.4602	1.4779	60	250	12	225	285
4	3	1.1060	1.1217	52	310	42	215	460
5	6	1.3098	1.3378	44	504	71	408	698
6	9	0.9924	1.0227	48	739	129	543	930
7	12	1.3307	1.3727	48	793	51	725	935
8	15	1.2689	1.3137	45	788	76	704	933
9	30	1.3973	1.4601	52	1410	133	1230	1691
10	45	1.3522	1.4206	22	2306	68	2195	2433
11	90	1.6010	1.6850	-	-	-	-	-
12	0	-	-	-	0	0	0	0

Coupon (HfB₂-20% SiC)	Time at Temp (h)	Pre Weight (g)	Post Weight (g)	Number of Oxide Scale Thickness Measurements	Average (μm)	Standard Deviation (μm)	Minimum (μm)	Maximum (μm)
1	0.5	1.1031	1.1043	118	17	4	8	29
2	1	1.2487	1.2507	100	25	5	13	38
3	2	1.4683	1.4712	96	33	8	11	54
4	3	1.2354	1.2389	92	44	12	29	85
5	6	1.2721	1.2765	84	51	16	18	82
6	9	0.8000	0.8048	84	53	20	22	94
7	12	1.2564	1.2643	83	75	22	30	119
8	15	1.1206	1.1309	80	101	15	72	156
9	30	1.1107	1.1248	82	113	26	37	165
10	45	1.4225	1.4431	90	131	42	32	271
11	90	1.2367	1.2580	94	160	57	23	301
12	0	-	-	-	0	0	0	0

0.5 h

1 h

2 h

3 h

6 h

9 h
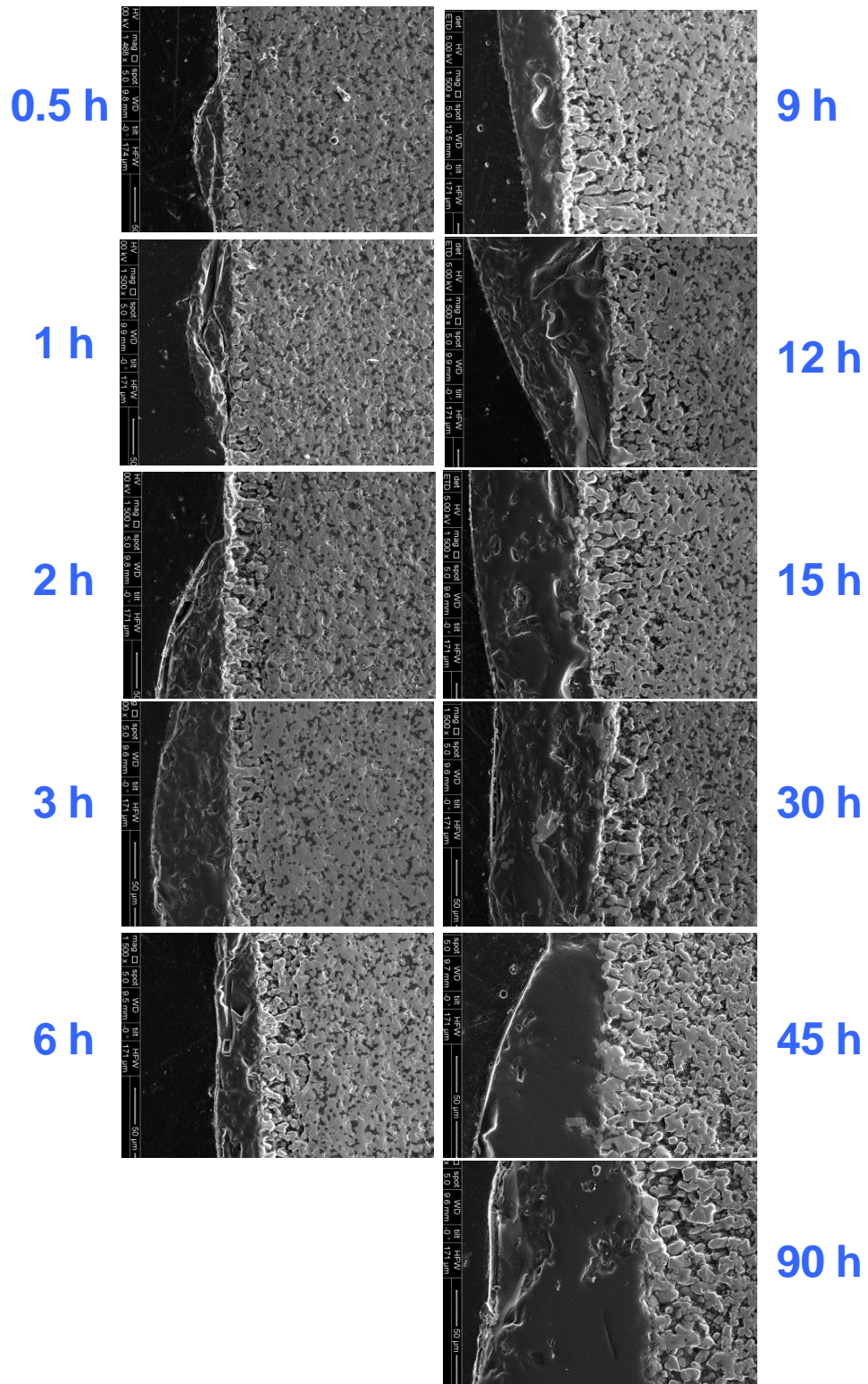
12 h

15 h

30 h

45 h

90 h

Figure 60: SEM Images of HfB$_2$-20% SiC Oxide Scales after Various Amounts of Time at 1500°C in Air

Analysis: Figure 61 provides a graphical representation of oxide scale thickness versus time for the HfB_2-20% SiC coupons. Results compare favorably to Parthasarathy's model for the oxidation of SiC-containing refractory diborides [98], which is based on mechanistic models and experimental data from several sources. This indicates, along with comparisons to micrographs of oxide scales found in the literature, that the oxidation behavior of the research materials is consistent with the literature. Also, comparisons to the results of the stressed oxidation tests, as reported in section 4.6 starting on page 112 and specifically Figure 36 on page 120, indicate that the experimental facility used in the stressed oxidation tests did not affect the analysis of oxidation behavior.
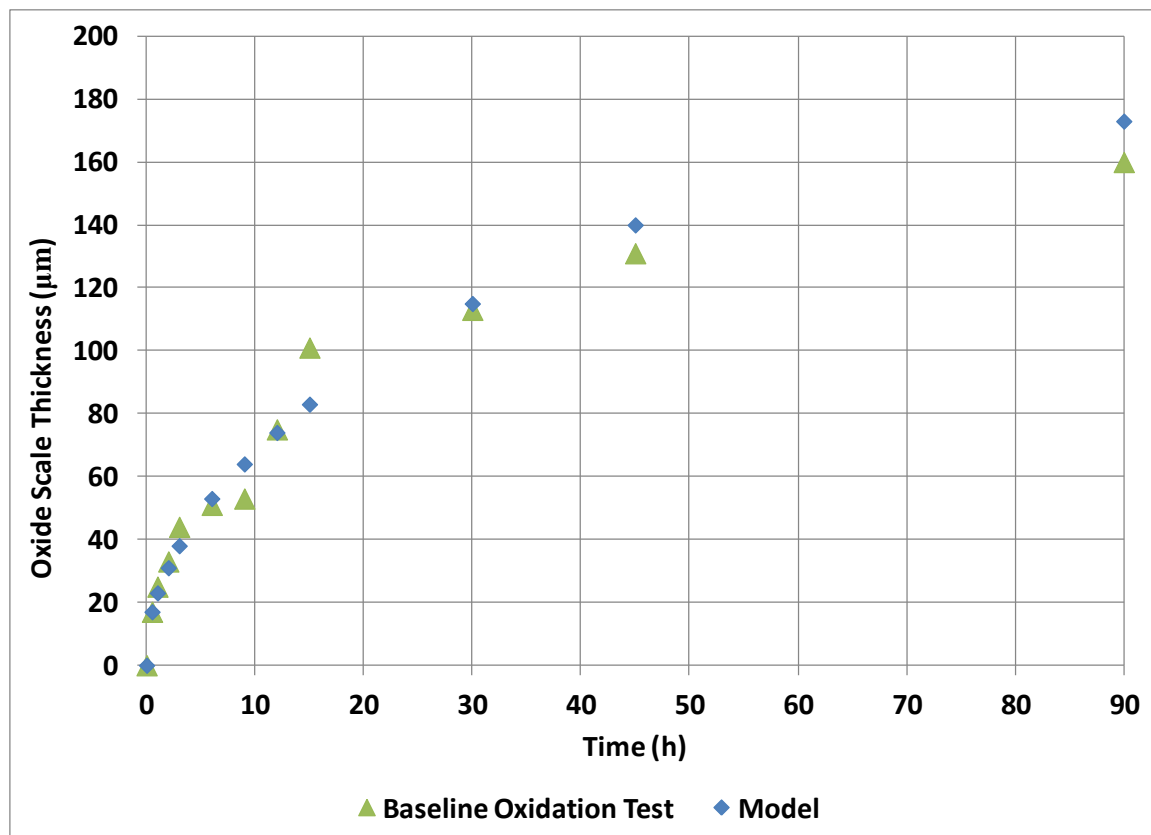

Figure 61: Oxide Scale Thickness vs Time for HfB$_2$-20% SiC at 1500°C in Air Model Data from Parthasarathy et al. [98]

The results of the HfB$_2$-0% SiC baseline oxidation test (reference Figure 62) do not compare as well to Parthasarathy's model for the oxidation of diborides with no SiC [26], but are nonetheless admirable considering the variety of materials, parameters, unknowns, and orders of magnitude handled by the model. Micrographs and oxide scale thicknesses compare favorably to Winder's experiments [13], with Table 8 on page 85 and Figure 34 on page 117 serving as examples. The data points at 30 and 45 hours appear distinctive in terms of trend. The 90-hour data point is not included in the figure, because a specific thickness could not be assigned, due to complete oxidation of the coupon.
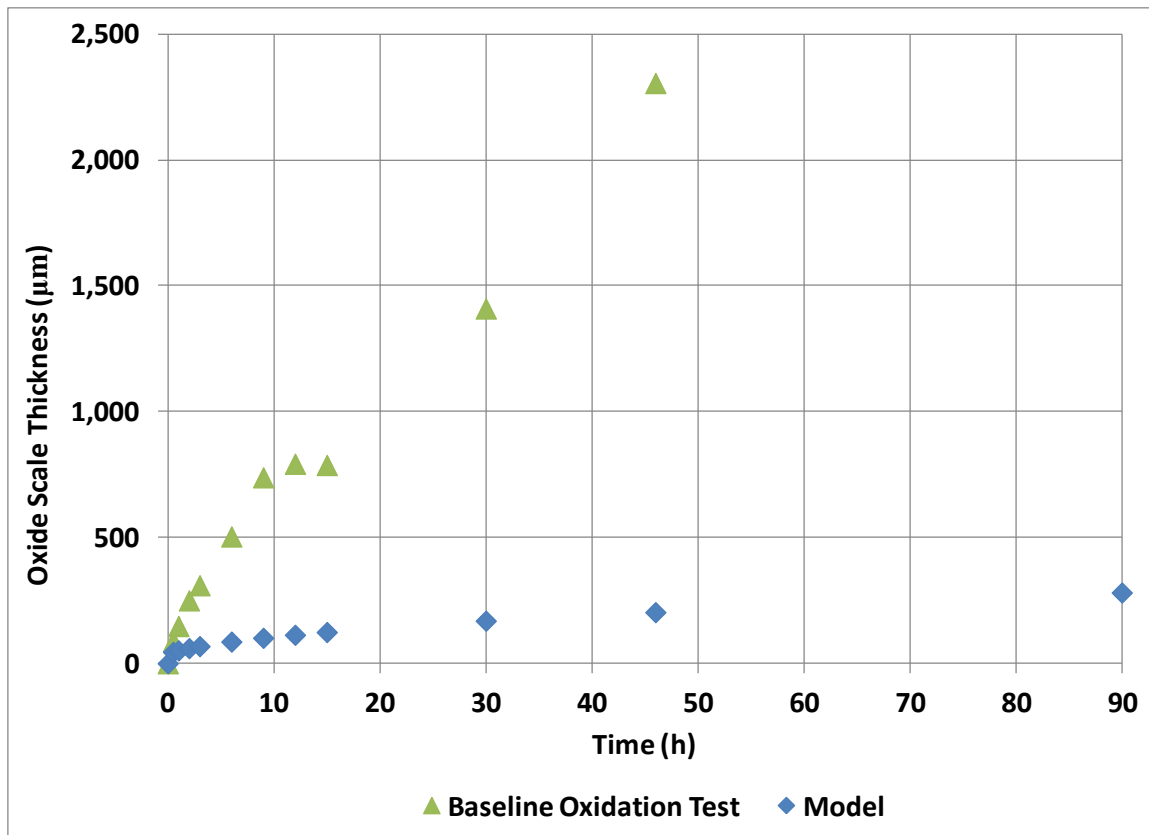

Figure 62: Oxide Scale Thickness vs Time for HfB$_2$-0% SiC at 1500°C in Air Model Data from Parthasarathy et al. [98]

While the early HfB$_2$-0% SiC data appear to follow the expected parabolic trend, the later data clearly deviate to higher oxidation rates, which ultimately consume all of the parent material. This is concerning for aerospace applications and warrants further discussion, even if it might be considered an experimental anomaly. At first glance, a comparison of Figure 59 and Figure 62 suggests that geometric effects are responsible. At 9 hours and later, the oxide is no longer small compared to the parent material, and edge cracks can be observed in the coupons. Some edge cracks penetrate all the way through the oxide layer in the 6th and subsequent coupons, such as shown in Figure 63.
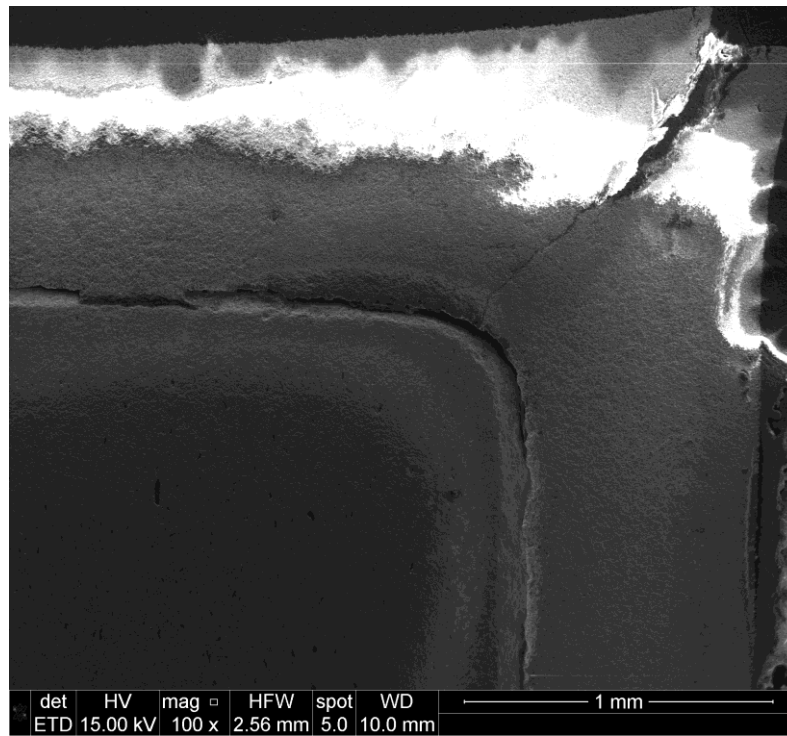
**Figure 63: SEM Image of an Edge Crack in a HfB$_2$-0% SiC Coupon
Heat Treated at 1500°C in Air for 12 hours**

Additionally, it is noted that some non-symmetric behavior must have occurred in the oxidation of the coupons as a function of vertical position, since the bottom faces rested on alumina spacers, which seemed to somewhat insulate those faces from oxidation. This was intentional, as one of the purposes of these tests was to imitate the configuration for the stressed oxidation tests, thus providing a baseline for comparisons. A preliminary test of HfB_2-0% SiC at 1500°C for 10 hours showed that oxide thicknesses did not vary by more than 10% as a function of vertical position, where the variations close to 10% only occurred near the alumina spacers. Thus, oxide scale thicknesses were measured from the cross sections after grinding off the oxide layers from the top faces of the coupons (i.e. the large faces exposed to air). As the HfB_2-0% SiC coupons approached complete oxidation, measurements of the oxide scale thicknesses necessarily moved closer to the alumina spacers. This effect would have been small in the early HfB_2-0% SiC coupons and was not an issue with the HfB_2-20% SiC coupons, because a consistent and shallow grinding depth was effective for all of the HfB_2-20% SiC coupons. Thus, there is more than one geometric effect to consider when analyzing the later coupons and data from the HfB_2-0% SiC baseline oxidation test.

Although this research effort is not focused on suspected geometric effects, whether occurring during heat treatment or cool down, it is important to recognize that geometry and stress concentrations can have profound impacts on the application and performance of material systems, and the material systems discussed in this paper are no exception. However, it is promising to note that edge cracks in the oxide scale and deviations from parabolic oxidation behavior were not observed in the HfB_2-20% SiC material even after 90 hours at 1500°C. The addition of SiC decreased oxidation rates

more than an order of magnitude and kept the oxide scale small compared to the parent material. Additionally, the oxide scale remained attached to the parent material despite being quickly removed from the 1500°C furnace to room temperature. Figure 64 provides an illustration of the ability of the HfB_2-20% SiC material system to insulate itself from oxidation even after 90 hours at 1500°C in air.
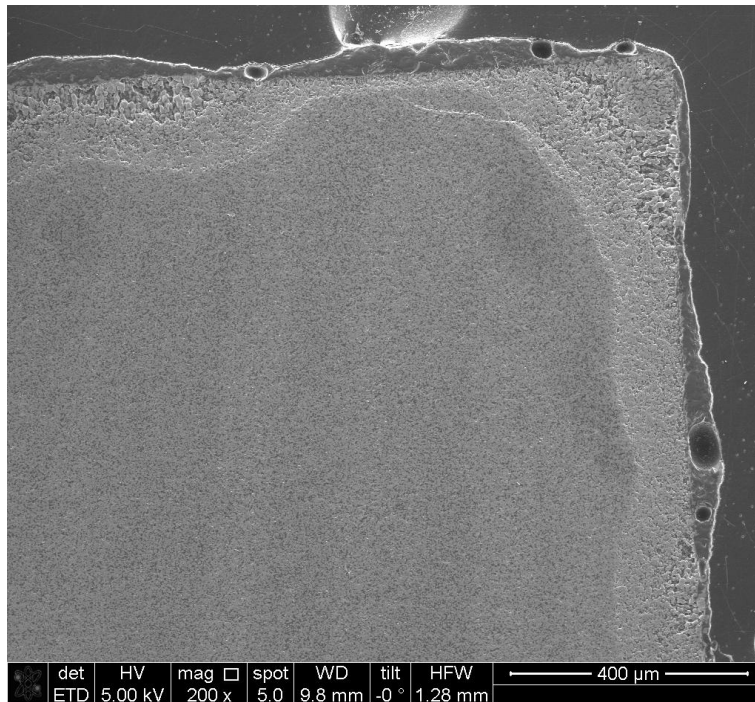

**Figure 64: SEM Image of the Edge of a HfB_2-20% SiC Coupon
Heat Treated at 1500°C in Air for 90 hours**

Setting aside the later HfB_2-0% SiC oxide thicknesses that deviated from parabolic behavior, substantive questions still remain as to why the early data is so much higher in magnitude compared to the model. For example, at the 9-hour mark, the baseline oxidation test reports 739 μm of oxidation, while the model shows only 105 μm. While there are many experimental and modeling factors to consider, it seems reasonable

175

to validate whether the assumptions used in the development of the model are consistent with the experiment, whether the experimental and modeled materials are similar, whether there might be reasonable variations in certain parameters that would cause the observed difference in oxidation rates, and whether the current experiment has any significant differences compared to the experiments from which the model obtained its supporting data. Even a cursory review of these validation efforts would require several pages, so only the highlights will be listed in the following paragraph.

All of the assumptions discussed by Parthasarathy et al. [26] seem reasonable when applied to the present research. Potentially significant variations in the HfB_2-0% SiC research materials include about 5% porosity and 2% Zr. These factors could have second order effects, assuming they affect the pore fraction and pore radius of the resulting oxide scale, which significantly affect oxidation rates according to the model. The effect of pore radius is large above 1500°C and when pore radius is smaller than 1 μm. For example, when applied to ZrB_2, the model shows that an order of magnitude increase in the pore radius results in a near doubling of the oxide layer thickness after 1 hour at 1500°C. Similarly, an order of magnitude increase in pore fraction results in an order of magnitude increase in oxide layer thickness. The model appears to be less sensitive to oxygen partial pressure at higher temperatures, such as those experienced in this research. Reasonable variations of the parameters of the model, performed with a computerized version provided by Parthasarathy, did not provide any substantial increases in oxide layer thickness that would explain the large differences compared to the experimental results. The varied parameters included time, temperature, velocity, and O_2, H_2O, SiC, and impurity fractions. However, the porosity and Zr content of the parent

material, as well as the pore fraction and pore radius of the oxide, could not be varied

from the values assumed by the computerized model. A review of experiments from

which the model obtained its supporting data did not provide any additional ideas as to

why the modeled and experimental data differ, other than those possibilities already

discussed. The work of Severen provided the closest comparison to the present research,

which included the oxidation of HfB_2-0% SiC at 1600°C in air for up to 5 hours [120].

Severen's work only reported weight gains, which compare favorably with the model. A

micrograph of the parent material appears to show some porosity, but it is not discussed

in the report. Thus, in the absence of any clear cause for the difference in oxide scale

thicknesses, this research must reaffirm Parthasarathy's call for future experimenters to

report information related to pore fraction, pore radius, velocity, and water content. The

porosity of the parent material could also be an important factor in oxidation rates.

Figure 65 provides an interesting look at the baseline oxidation tests in terms of

weight gain per unit surface area of the coupons. For these calculations, it was assumed

that no oxidation occurred on the bottom faces, so the areas of only 5 faces on each

coupon were totaled. Once again, HfB_2-20% SiC data compares well to the model and

only appears about 25% lower. Interestingly, HfB_2-0% SiC data also seems to compare

well to the model in terms of weight gain, despite the difference in oxide scale

thicknesses. The geometric effects, discussed earlier in regard to the later data, appear

less severe, but nonetheless present as the experimental weight gains appear to diverge

from the modeled data as time goes on. Less emphasis is placed on the weight gain

results in this research for the HfB_2-0% SiC material, because this research did not

control for or provide a consistent means of capturing or not capturing the liquid boria

that flowed from parent material during heat treatment. Thus, even though the weight

gains provide a favorable comparison between the experimental and modeled data, they

do not lessen the importance of future efforts paying close attention to the difference in

experimental and modeled oxide scale thicknesses, which were observed in this research.
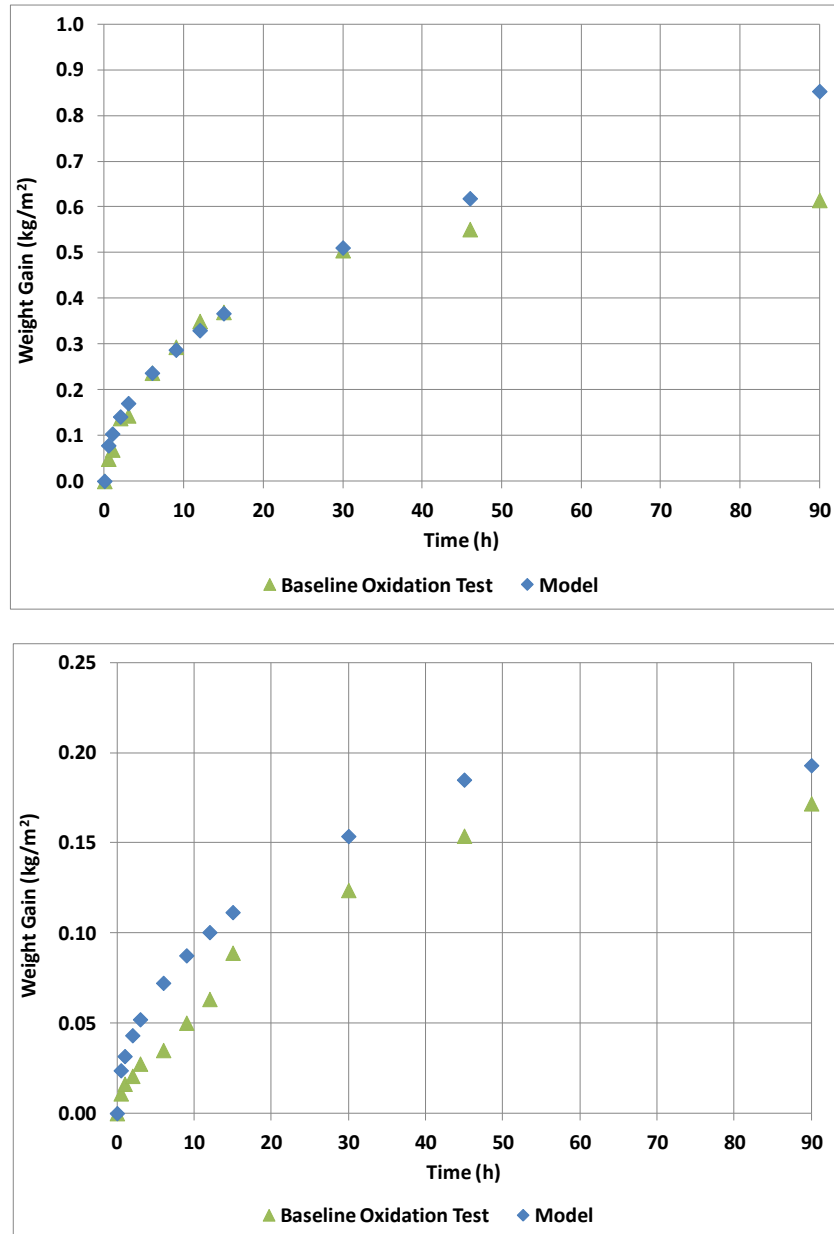
**Figure 65: Weight Gain vs Time
for HfB$_2$-0% SiC (Top) and -20% SiC (Bottom) at 1500°C in Air
Model Data from Parthasarathy et al.** [98]

Some final points relate to the long-term oxidation of SiC-containing diborides. Shugart studied variations in ZrB_2-30% SiC oxidation kinetics and looked at short- and long-term oxide scale development [121]. Shugart showed correlations between glass and oxide thicknesses, relationships between burst bubbles and scallops, and standard deviations between 30 and 80% of average oxide layer thickness. The same observations were found in the present research, although standard deviations seem less, ranging from 15 to 37% in Table 19 for the HfB_2-20% SiC coupons. The measured thicknesses include the glass and metal oxide. The standard deviations appear related to time, following the parabolic behavior of the average thickness, illustrated in Figure 66. The outlier is the 8th coupon at 15 hours, which was prepared similar to the other coupons and had no noticeable differences prior to the test.
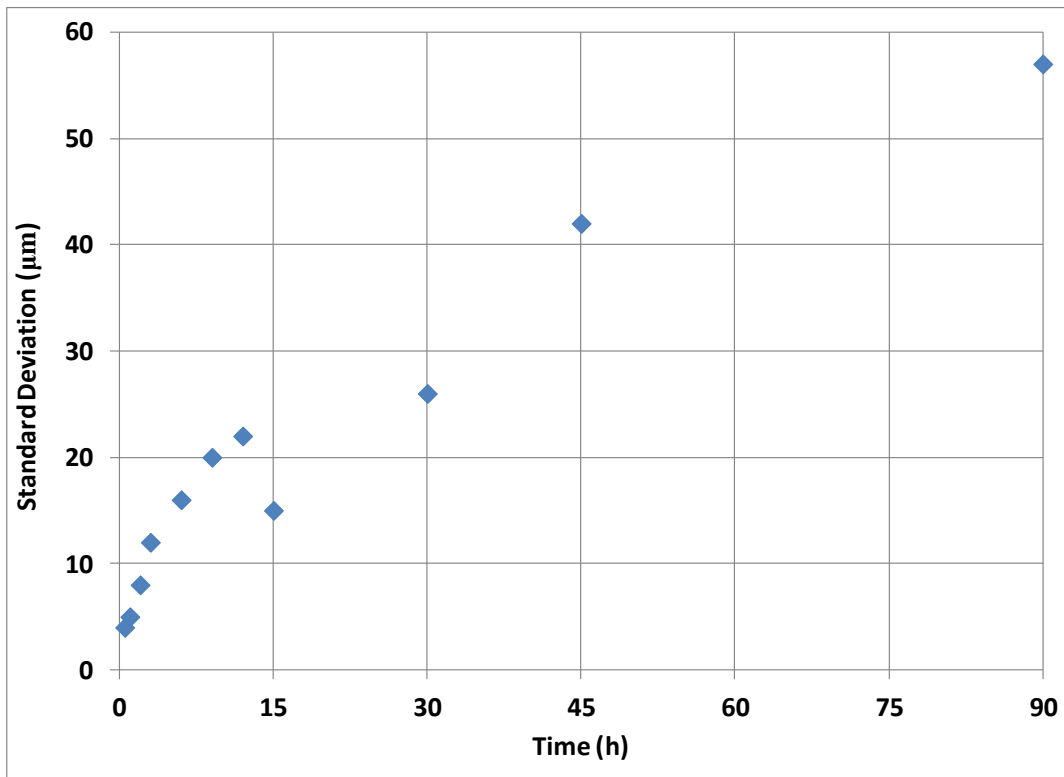

Figure 66: Standard Deviation of Oxide Scale Thickness vs Time for HfB_2-20% SiC at 1500°C in Air

Furthermore, Shugart calls for better life prediction methods as short-term tests appear insufficient at predicting long-term oxidation behavior. To this end, and in hopes of future improvements to the oxidation resistance of these materials, the following observations are also provided. The minimum and maximum oxidation depths are of profound interest in aerospace research and development. While the maximum depths drive limitations in the application of the material, the minimum depths provide hope that opportunities exist for further improvements in oxidation resistance. Thus, Figure 61 is re-presented as Figure 67 with bars for the minimum and maximum observed oxide layer thicknesses, which include the total thickness of both the glass and metal oxide layers.
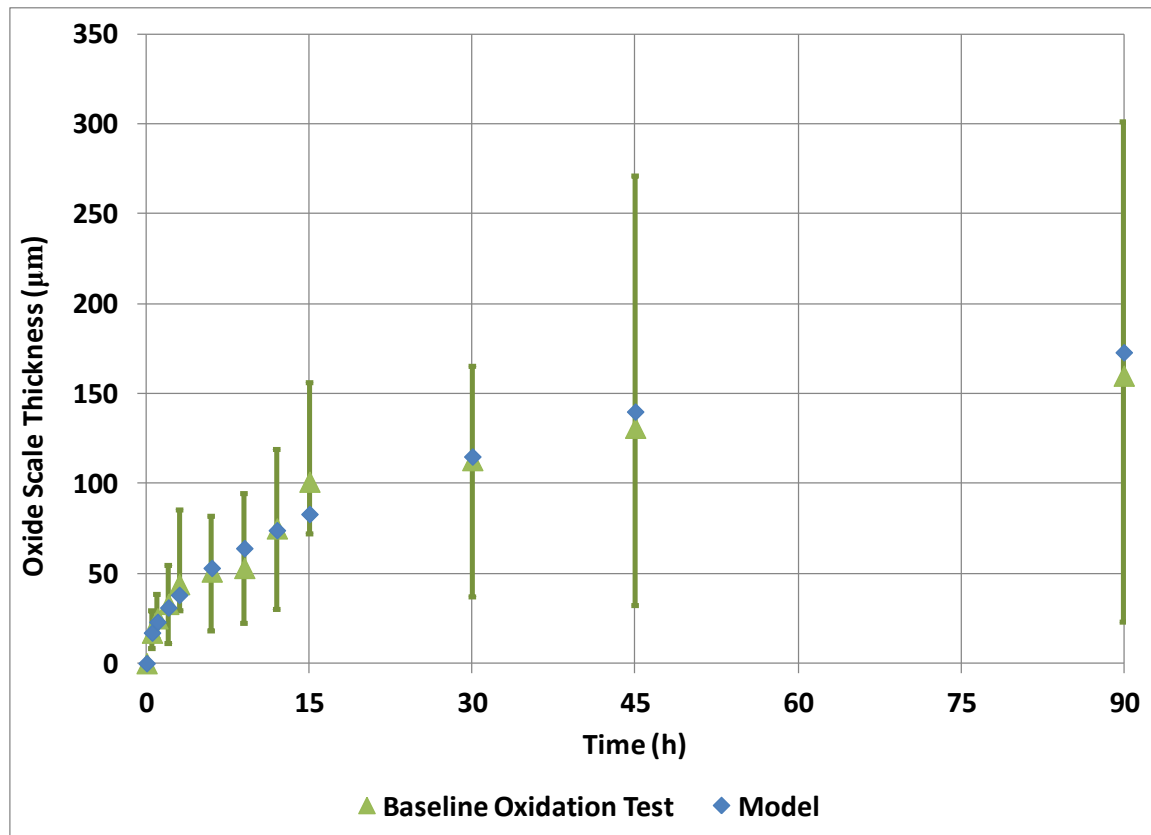

Figure 67: Minimum, Maximum, and Average Oxide Scale Thicknesses vs Time for HfB$_2$-20% SiC at 1500°C in Air Model Data from Parthasarathy et al. [98]

180

Interestingly, while the average and maximum observed thicknesses still appear to be growing after 90 hours, the minimums appear to have leveled off around 20 to 40 μm, once again with the exception of the outlying data point at 15 hours. The minimums do not appear to be correlated to position on the coupons or facing direction within the furnace. However, some additional insights might come from looking at SEM images of some of the thinnest and thickest regions of oxide scale, presented in Figure 68.
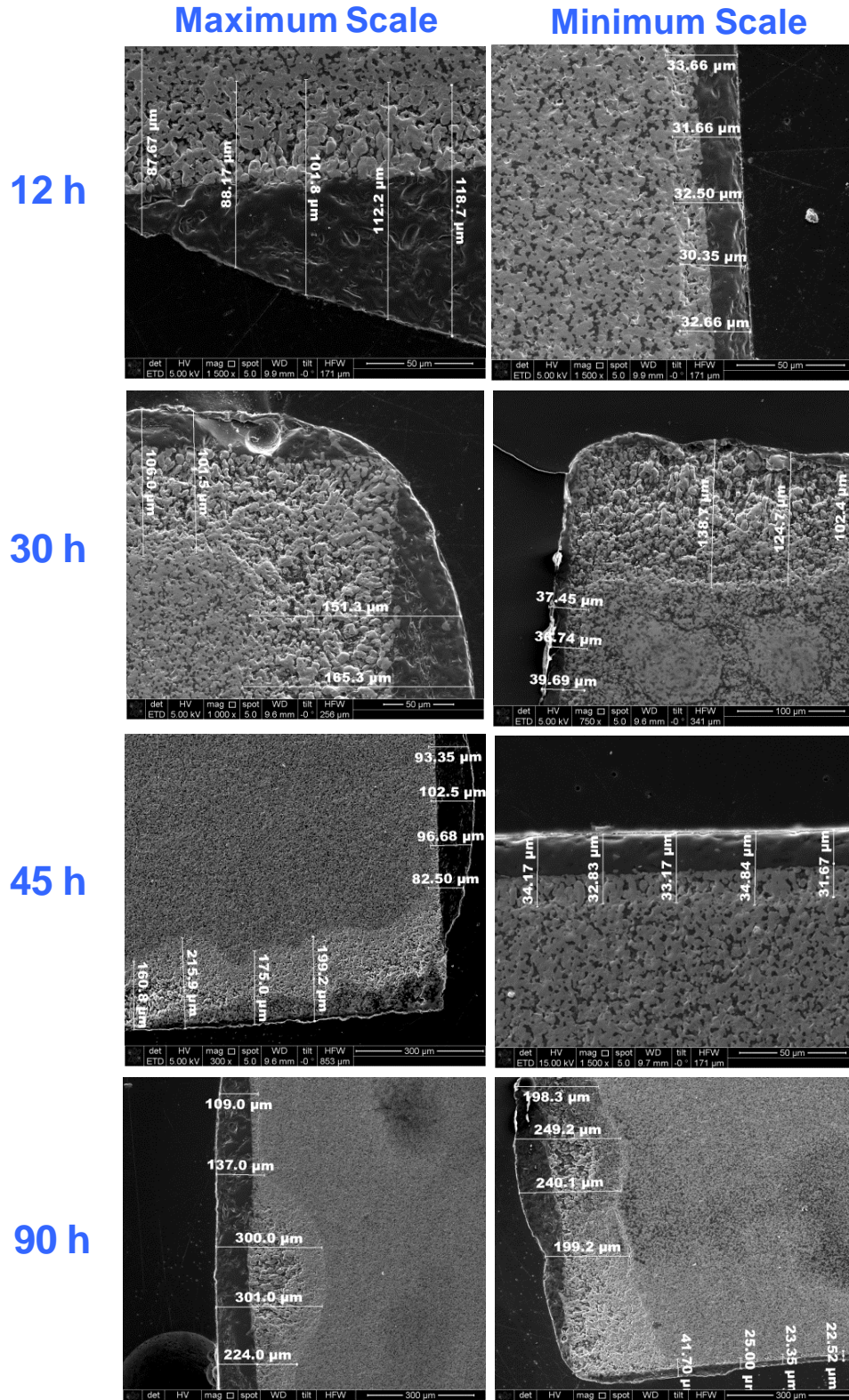
Figure 68: SEM Images of Minimum and Maximum Oxide Scale Thicknesses for HfB₂-20% SiC at 1500°C in Air

182

The first observation from Figure 68 is that all of the thinnest regions of oxide scale are covered by a very consistent layer of glass. No bubbles or scallops are observed in these areas. On the other hand, the thickest regions all seem to involve bubbles or scallops. Some of the thickest regions, however, do have a very consistent layer of glass covering them, suggesting that bubble bursts occurred and then glass layers recovered over the regions. For example, the thickest regions of the coupons at 45 and 90 hours in Figure 68 occurred in scallops covered by glass. Two distinctly different pore sizes are observed in the scallop at 90 hours, suggesting that bubble bursts might cause larger pore fractions and pore radii in the metal oxide. Oxygen might be transported at a faster rate to the substrate in these regions, even after glass recovery, and provide burst bubbles a longer-term effect. Thus, one might consider that maybe the glass layer does not provide much of a direct barrier to oxygen transport, but more importantly is related to reduction in the pore sizes found in the metal oxide. Oxidation immediately after a bubble burst, when little or no glass covers the region, cannot account for the full magnitude of longer-term scallops, because scallops observed at shorter times are generally smaller than at longer times. Thus, there must be other factors to consider in long term development of the oxide scale, related to burst bubbles, such as presented in the following paragraph.

The second observation is that a distinction should be made between very large burst bubbles that seem to only occur early in the development of the oxide scale and burst bubbles that supposedly create the observable scallops found throughout the time at temperature. The stressed oxidation test in this research provided an opportunity to view the same specimen at different time intervals. The very large burst bubbles were only observed early on in the test and are therefore referred to as initial burst bubbles,

183

henceforth. The same, identical, initial burst bubbles were still observable at later time intervals, even after being reheated and cooled several times up to 12 hours. New initial burst bubbles were not observed subsequent to the initial observation (reference Figure 38, page 124). Artifacts from the initial burst bubbles of the baseline oxidation test can also be seen in Figure 58 on page 167. The coupons are all about 6 mm across, and the initial burst bubbles measure on the order of 200 to 2000 μm. However, the alternating buildups of glass and neighboring scallops in the early coupons are clearly smaller than the initial burst bubbles. The alternating buildups of glass and scallops, which are typically reported in the literature and also observed throughout this research, should not be confused with the gas bubbles themselves. At longer times, some gas bubbles were found trapped in the glass layer and appear to grow larger as the time at temperature increases. Examples of these features can be found in Figure 69.
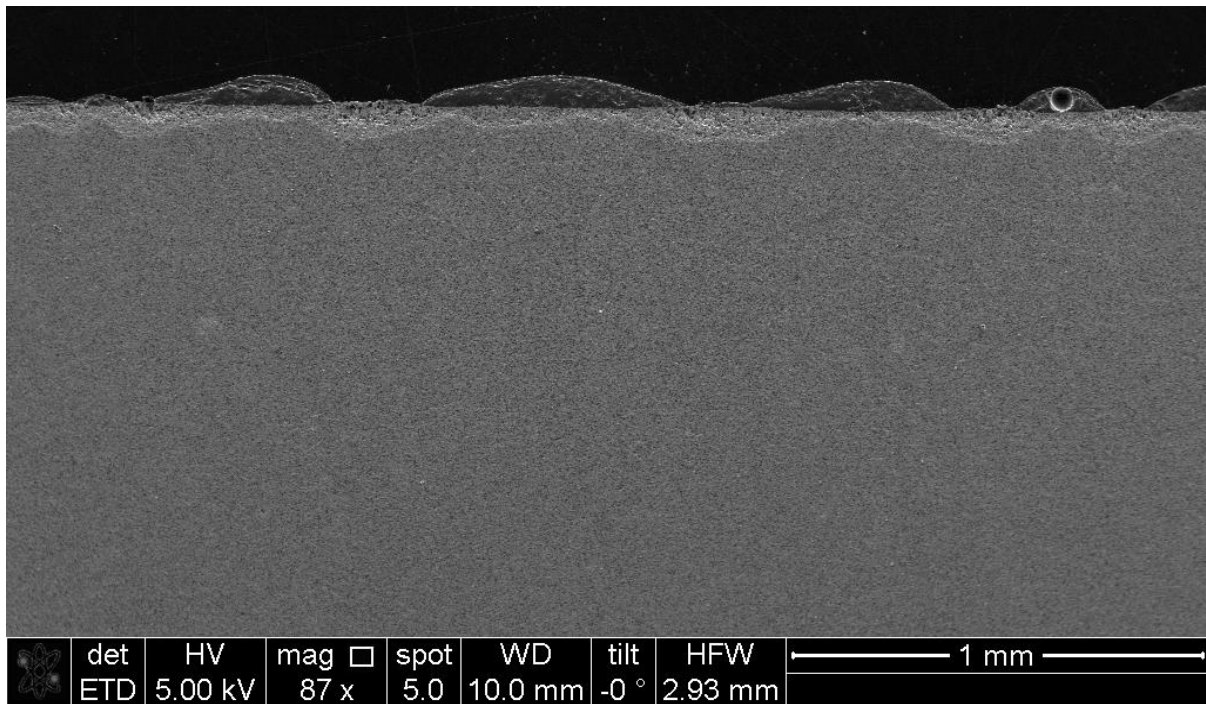
Figure 69: SEM Image of Oxide Scale Features
Observed in HfB$_2$-20% SiC after 12 hours at 1500°C in Air

Although scallops in the later coupons seem to approach the magnitude of the initial burst bubbles, they still seem distinct. Photos of the coupon surfaces from the baseline oxidation test (i.e. Figure 58 on page 167) do not show initial burst bubbles increasing in size with time at temperature, although we know that the size of the scallops did increase. Together, these observations suggest that the gasses only result in initial burst bubbles early in the development of the oxide layer.

The third and final observation relates to Figure 68 on page 182, which shows the thinnest and thickest regions of oxide scale. Four of the micrographs depict locations near the corners of the coupons and, in three of those micrographs, the oxidation behavior appears completely different on the adjacent sides. Oxide thicknesses were tabulated by side for each coupon, and the overall oxidation behavior of one particular side did not stand out for any given coupon. This seems to suggest that facing direction within the furnace and surface preparation are not factors. Although, polishing inconsistencies are often observed at corners. Thus, this research is left with an interesting motivation. What causes this difference in oxidation behavior, and can we make improvements such that the oxidation resistance of the entire surface is improved? Can the improvement of oxidation resistance be related to the reduction or elimination of bubble bursts and the ability to form a consistent glass layer over the entire surface? Interestingly, the 8th coupon does not show large bubble features on the surface in Figure 58 on page 167, and yet its oxide scale thicknesses lie above the trendline. Alternatively, the baseline oxidation test has clearly shown that it is possible for HfB_2-20% SiC material, at least in isolated locations, to maintain oxide scales on the order of 20 to 30 µm even after 90 hours at 1500°C. Whether improvements in oxidation resistance are related to initial

185

burst bubbles, it is the opinion of this author that improvements can still be made to

overall oxidation resistance for conditions where the glass phase remains viable.

References

[1] P. J. Ouzts, "The Joint Technology Office on Hypersonics," *15th AIAA International Space Planes and Hypersonic Systems and Technologies Conference*. Jan-2008.

[2] S. H. Walker, "AF Science and Technology Game Changing Investments," in *13th Annual Science and Technology Conference/Defense Tech Exposition*, 2012.

[3] "Hypersonic Technology and Development: Imperatives Critical to U.S. National Security and Aerospace Superiority." Aerospace Industries Association, p. 2.

[4] "NHSC - Materials and Structures." National Hypersonic Science Center, p. 2, 2011.

[5] D. R. Jenkins, *X-15: Extending the Frontiers of Flight*. Washington, D.C.: National Aeronautics and Space Administration, 2007.

[6] "Review and Evaluation of the Air Force Hypersonic Technology Program," The National Academies Press, Washington, D.C., 1998.

[7] G. Warwick, "Darpa Refocuses Hypersonics Research on Tactical Missions," *Aviat. Week Space Technol.*, 2013.

[8] G. Norris, "Skunk Works Reveals SR-71 Successor Plan," *Aviat. Week Space Technol.*, 2013.

[9] W. G. Fahrenholtz, G. E. Hilmas, I. G. Talmy, and J. A. Zaykoski, "Refractory Diborides of Zirconium and Hafnium," *J. Am. Ceram. Soc.*, vol. 90, no. 5, pp. 1347–1364, May 2007.

[10] W.-M. Guo, G.-J. Zhang, and H.-T. Lin, "High-temperature flexural creep of ZrB2-SiC ceramics in argon atmosphere," *Ceram. Int.*, vol. 38, no. 1, pp. 831–835, 2012.

[11] S. M. Kats, S. S. Ordan'yan, and V. I. Unrod, "Compressive creep of alloys of the ZrC-ZrB2 and TiC-TiB2 systems," *Sov. Powder Metall. Met. Ceram.*, vol. 20, no. 12, pp. 886–890, 1981.

[12] I. I. Spivak, R. A. Andrievskii, V. V Klimenko, and V. D. Lazarenko, "Creep in the binary systems TiB2-TiC and ZrB2-ZrN," *Sov. Powder Metall. Met. Ceram.*, vol. 13, no. 8, pp. 617–620, 1974.

[13] S. L. Winder, "Mechanical testing of ultra-high temperature ceramics at 1500°C in air - Development of an experimental facility and test method," 2015.

[14] J. J. Meléndez-Martínez, A. Domínguez-Rodríguez, F. Monteverde, C. Melandri, and G. De Portu, "Characterisation and high temperature mechanical properties of zirconium boride-based materials," *J. Eur. Ceram. Soc.*, vol. 22, no. 14, pp. 2543–2549, 2002.

[15] S. Gangireddy, J. W. Halloran, and Z. N. Wing, "Flexural creep of zirconium diboride-silicon carbide up to 2200°C in minutes with non-contact electromagnetic testing," *Journal of the European Ceramic Society*, vol. 33, no. 15. pp. 2901–2908, Jan-2013.

[16] M. W. Bird, R. P. Aune, F. Yu, P. F. Becher, and K. W. White, "Creep behavior of a zirconium diboride-silicon carbide composite," *Journal of the European Ceramic Society*, vol. 33, no. 13. pp. 2407–2420, Jan-2013.

[17] I. G. Talmy, J. A. Zaykoski, and C. A. Martin, "Flexural Creep Deformation of ZrB2/SiC Ceramics in Oxidizing Atmosphere," *J. Am. Ceram. Soc.*, vol. 91, no. 5, pp. 1441–1447, 2008.

[18] W. H. Rhodes, E. V Clougherty, and D. Kalish, "Research and Development of Refractory Oxidation-Resistant Diborides," vol. Volume IV, no. Part II: Mechanical Properties, 1970.

[19] S. Musikant, *What Every Engineer Should Know About Ceramics*. New York: Marcel Dekker, Inc., 1991.

[20] R. W. Davidge, *Mechanical Behaviour of Ceramics*. Cambridge: Cambridge University Press, 1979.

[21] M. Ashby, H. Shercliff, and D. Cebon, *Materials Engineering, Science, Processing and Design*. Oxford, UK: Elsevier, Ltd., 2007.

[22] D. W. Klingery, H. K. Bowen, and D. R. Uhlmann, *Introduction to Ceramics*. John Wiley & Sons, Inc., 1976.

[23] W. R. Cannon and T. G. Langdon, "Creep of ceramics - Part 1 - Mechanical characteristics," *Journal of Materials Science*, vol. 18, no. 1. pp. 1–50, Jan-1983.

[24] M. M. Schwartz, *Handbook of Structural Ceramics*. New York: McGraw-Hill, Inc., 1992.

[25] W. G. Fahrenholtz and G. E. Hilmas, "Oxidation of ultra-high temperature transition metal diboride ceramics," *Int. Mater. Rev.*, vol. 57, no. 1, pp. 61–72, 2012.

[26] T. A. Parthasarathy, R. A. Rapp, M. Opeka, and R. J. Kerans, "A model for the oxidation of ZrB2, HfB2 and TiB2," *Acta Materialia*, vol. 55, no. 17. p. 5999, Jan-2007.

[27] I. G. Talmy, J. A. Zaykoski, and M. M. Opeka, "High-Temperature Chemistry and Oxidation of ZrB2 Ceramics Containing SiC, Si3N4, Ta5Si3, and TaSi2," *Journal of the American Ceramic Society*, vol. 91, no. 7. p. 2250, Jan-2008.

[28] J. E. Hove and W. C. Riley, *Ceramics for Advanced Tchnologies*. New York: John Wiley & Sons, Inc., 1966.

[29] A. Bellosi and F. Monteverde, "Ultra-high temperature ceramics: Microstructure control and properties improvement related to materials design and processing procedures," *European Space Agency, (Special Publication) ESA SP*, no. 631. Jan-2006.

[30] L. Kaufman and E. V. Clougherty, "Investigation of boride compounds for very high temperature applications (Technical Documentary Report No. RTD-TDR-63-4096)," Wright-Patterson AFB, Ohio, 1963.

[31] A. L. Chamberlain, W. G. Fahrenholtz, and G. E. Hilmas, "Reactive hot pressing of zirconium diboride," *J. Eur. Ceram. Soc.*, vol. 29, no. 16, pp. 3401–3408, Dec. 2009.

[32] A. L. Chamberlain, W. G. Fahrenholtz, and G. E. Hilmas, "Pressureless Sintering of Zirconium Diboride," *J. Am. Ceram. Soc.*, vol. 89, no. 2, pp. 450–456, Feb. 2006.

[33] L. Chen, Y. Gu, L. Shi, Z. Yang, J. Ma, and Y. Qian, "Synthesis and oxidation of nanocrystalline HfB2," *J. Alloys Compd.*, vol. 368, pp. 353–356, Jan. 2004.

[34] S. J. Lee, E. S. Kang, S. S. Baek, and D. K. Kim, "Reactive Hot Pressing and Oxidation Behavior of Hf-Based Ultra-High-Temperature Ceramics," *Surf. Rev. Lett.*, vol. 17, no. 02, pp. 215–221, 2010.

[35] D.-W. Ni, G.-J. Zhang, Y.-M. Kan, and P.-L. Wang, "Hot Pressed HfB2 and HfB2-20 vol%SiC Ceramics Based on HfB2 Powder Synthesized by Borothermal Reduction of HfO2," *Int. J. Appl. Ceram. Technol.*, vol. 7, no. 6, pp. 830–836, Nov. 2010.

[36] D.-W. Ni, J.-X. Liu, and G.-J. Zhang, "Microstructure refinement and mechanical properties improvement of HfB2-SiC composites with the incorporation of HfC," *Journal of the European Ceramic Society*, vol. 32, no. 10. pp. 2557–2563, Jan-2012.

[37] S. Venugopal, A. Paul, B. Vaidhyanathan, J. G. P. Binner, A. Heaton, and P. M. Brown, "Synthesis and spark plasma sintering of sub-micron HfB2: Effect of various carbon sources," *J. Eur. Ceram. Soc.*, vol. 34, no. 6, pp. 1471–1479, 2014.

[38] S. Venugopal, E. E. Boakye, A. Paul, K. Keller, P. Mogilevsky, B. Vaidhyanathan, J. G. P. Binner, A. Katz, and P. M. Brown, "Sol-Gel Synthesis and Formation Mechanism of Ultrahigh Temperature Ceramic: HfB 2," *J. Am. Ceram. Soc.*, vol. 97, no. 1, pp. 92–99, Jan. 2014.

[39] S. C. Zhang, G. E. Hilmas, and W. G. Fahrenholtz, "Pressureless Densification of Zirconium Diboride with Boron Carbide Additions," *J. Am. Ceram. Soc.*, vol. 89, no. 5, pp. 1544–1550, May 2006.

[40] B. E. Douglas, D. H. McDaniel, and J. J. Alexander, "Concepts and Models of Inorganic Chemistry," vol. 3rd ed. John Wiley & Sons, Inc., New York, 1994.

[41] M. M. Opeka, I. G. Talmy, and J. A. Zaykoski, "Oxidation-based materials selection for 2000°C+ hypersonic aerosurfaces: Theoretical considerations and historical experience," *Journal of Materials Science*. Jan-2004.

[42] C. M. Carney, "Oxidation resistance of hafnium diboride-silicon carbide from 1400 to 2000°C," *Journal of Materials Science*, vol. 44, no. 20. p. 5673, Jan-2009.

[43] D. Sciti, A. Balbo, and A. Bellosi, "Oxidation behaviour of a pressureless sintered HfB2-MoSi2 composite," *J. Eur. Ceram. Soc.*, vol. 29, no. 9, pp. 1809–1815, 2009.

[44] T. A. Parthasarathy, R. A. Rapp, M. Opeka, and R. J. Kerans, "Effects of phase change and oxygen permeability in oxide scales on oxidation kinetics of ZrB2 and HfB2," *J. Am. Ceram. Soc.*, vol. 92, no. 5, pp. 1079–1086, 2009.

[45] A. Bellosi, F. Monteverde, and D. Sciti, "Fast Densification of Ultra-High-Temperature Ceramics by Spark Plasma Sintering," *Int. J. Appl. Ceram. Technol.*, vol. 3, no. 1, pp. 32–40, Jan. 2006.

[46] F. Monteverde, "Ultra-high temperature HfB2-SiC ceramics consolidated by hot-pressing and spark plasma sintering," *Journal of Alloys and Compounds*, vol. 428, no. 1–2. pp. 197–205, 2007.

[47]   R. Orrù and G. Cao, "Comparison of Reactive and Non-Reactive Spark Plasma Sintering Routes for the Fabrication of Monolithic and Composite Ultra High Temperature Ceramics (UHTC) Materials," *Materials (Basel).*, vol. 6, no. 5, pp. 1566–1583, Apr. 2013.

[48]   E. Zapata-Solvas, D. D. Jayaseelan, H. T. Lin, P. Brown, and W. E. Lee, "Mechanical properties of ZrB2- and HfB2-based ultra-high temperature ceramics fabricated by spark plasma sintering," *J. Eur. Ceram. Soc.*, vol. 33, no. 7, pp. 1373–1386, Jul. 2013.

[49]   *Engineering Materials Handbook - Crystallography and Engineering Properties of Ceramics*. ASM International, 1995.

[50]   P. Vajeeston, P. Ravindran, C. Ravi, and R. Asokamani, "Electronic structure, bonding, and ground-state properties of AlB 2-type transition-metal diborides," *Phys. Rev. B*, 2001.

[51]   M. Gasch, D. Ellerby, E. Irby, S. Beckman, M. Gusman, and S. Johnson, "Processing, properties and arc jet oxidation of hafnium diboride/silicon carbide ultra high temperature ceramics," *J. Mater. Sci.*, vol. 39, no. 19, pp. 5925–5937, Oct. 2004.

[52]   J. F. Lynch, C. G. Ruderer, and W. H. Duckworth, *Engineering Properties of Ceramics - Borides*. American Ceramic Society, 1966.

[53]   M. Opeka, I. Talmy, and E. Wuchina, "Mechanical, thermal, and oxidation properties of refractory hafnium and zirconium compounds," *J. Eur. …*, 1999.

[54]   E. Wuchina, M. Opeka, S. Causey, K. Buesking, J. Spain, A. Cull, J. Routbort, and F. Guitierrez-Mora, "Designing for ultrahigh-temperature applications: The mechanical and thermal properties of HfB2 , HfCx , HfNx and αHf(N)," *J. Mater. Sci.*, vol. 39, no. 19, pp. 5939–5949, Oct. 2004.

[55]   A. McHale, *Phase Equilibria Diagrams: Phase Diagrams for Ceramists: Volume X, Borides, Carbides, and Nitrides*. The American Ceramic Society, 1994.

[56]   J. Lawson, "Lattice thermal conductivity of ultra high temperature ceramics ZrB2 and HfB2 from atomistic simulations," *J. Appl. …*, 2011.

[57]   M. Gasch, S. Johnson, and J. Marschall, "Thermal Conductivity Characterization of Hafnium Diboride-Based Ultra-High-Temperature Ceramics," *J. Am. Ceram. Soc.*, vol. 91, no. 5, pp. 1423–1432, May 2008.

[58] A. Rezaie, W. G. Fahrenholtz, and G. E. Hilmas, "Evolution of structure during the oxidation of zirconium diboride-silicon carbide in air up to 1500°C," *J. Eur. Ceram. Soc.*, vol. 27, no. 6, pp. 2495–2501, 2007.

[59] F. Monteverde, A. Bellosi, and L. Scatteia, "Processing and properties of ultra-high temperature ceramics for space applications," *Materials Science and Engineering: A*, vol. 485, no. 1. pp. 415–421, 2008.

[60] J. Ramírez-Rico, M. A. Bautista, J. Martínez-Fernández, and M. Singh, "Compressive strength degradation in ZrB2-based ultra-high temperature ceramic composites," *J. Eur. Ceram. Soc.*, vol. 31, no. 7, pp. 1345–1352, Jun. 2011.

[61] I. H. Shames and F. A. Cozzarelli, *Elastic and Inelastic Stress Analysis*. Englewood Cliffs, NJ: Prentice-Hall, Inc., 1992.

[62] D. J. Green, "An introduction to the mechanical properties of ceramics." Cambridge University Press, Cambridge ; New York, 1998.

[63] N. E. Dowling, *Mechanical behavior of materials: engineering methods for deformation, fracture, and fatigue*. Prentice Hall, 1993.

[64] W. R. Cannon and T. G. Langdon, "Creep of ceramics - Part 2 - An examination of flow mechanisms," *Journal of Materials Science*, vol. 23, no. 1. pp. 1–20, Jan-1988.

[65] C. B. Carter and M. G. Norton, *Ceramic Materials: Science and Engineering*, vol. 2nd ed. Springer, 2013.

[66] K. V Ravi, "Observation of Bardeen-Herring Sources in Silicon," *Metallurgical Transactions*, vol. 3, no. 5. p. 1311–&, Jan-1972.

[67] B. Burton and D. T. Knight, "Prediction of the configuration of a `Bardeen-Herring' dislocation climb source under dynamic conditions," *Philosophical Magazine Letters*, vol. 65, no. 6. pp. 321–329, Jan-1992.

[68] F. R. N. Nabarro, "Steady-state diffusional creep," *Philos. Mag.*, vol. 16, no. 140, pp. 231–237, 1967.

[69] A. H. Chokshi, "Diffusion creep in oxide ceramics," *J. Eur. Ceram. Soc.*, vol. 22, no. 14, pp. 2469–2478, 2002.

[70] E. Arzt, M. F. Ashby, and R. A. Verrall, "Interface controlled diffusional creep," *Acta Metall.*, vol. 31, no. 12, pp. 1977–1989, 1983.

[71] F. R. N. Nabarro and H. L. de Villiers, *The Physics of Creep*. Bristol, PA: Taylor and Francis, Ltd., 1995.

[72] C.-H. Yu, C.-W. Huang, C.-S. Chen, Y. Gao, and C.-H. Hsueh, "A micromechanics study of competing mechanisms for creep fracture of zirconium diboride polycrystals," *Journal of the European Ceramic Society*, vol. 33, no. 10. pp. 1625–1637, Jan-2013.

[73] B. J. Dalgleish, E. B. Slamovich, and A. G. Evans, "Duality in the creep rupture of a polycrystalline alumina," *J. Am. Ceram. Soc.*, vol. 68, no. 11, pp. 575–581, 1985.

[74] J. B. Wachtman, "Mechanical properties of ceramics." Wiley, Hoboken, N.J., 2009.

[75] G. Bernard-Granger, C. Guizard, and R. Duclos, "Compressive creep behavior in air of a slightly porous as-sintered polycrystalline α-alumina material," *Journal of Materials Science*, vol. 42, no. 8. p. 2807, Jan-2007.

[76] A. H. Chokshi, "Critical Appraisal of Diffusivity Determinations from Experimental Creep Data," *J. Am. Ceram. Soc.*, vol. 71, no. 5, pp. C–241–C–243, May 1988.

[77] T. G. Langdon, "Dependence of creep rate on porosity," *J. Am. Ceram. Soc.*, vol. 55, no. 12, pp. 630–631, 1972.

[78] T. Langdon and R. Vastava, "An evaluation of deformation models for grain boundary sliding," *Mech. Test. Deform. …*, 1982.

[79] A. H. Heuer, R. M. Cannon, and N. J. Tighe, "Plastic deformation in fine-grain ceramics," in *Ultrafine-Grain Ceramics*, Springer, 1970, pp. 339–365.

[80] F. R. Larson and J. Miller, *A time-temperature relationship for rupture and creep stresses*. 1952.

[81] A. I. Avgustinik, S. M. Kats, and S. S. Ordan'yan, "Compressive creep of ZrC-NbC solid solutions in the temperature range 2600-3150 K," *Izv.Akad.Nauk SSSR, Neorg.Mater*, vol. 8, pp. 1417–1420, 1972.

[82] L. N. Dementev, P. V Zubarev, L. B. Nezhevenko, and V. I. Groshev, "Investigation of the Influence of Grain Size on High-Temperature Creep of ZrC," *Phys.Met.Metallogr.*, vol. 39, no. 3, pp. 117–123, 1975.

[83] B. D. Gurevich, L. B. Nezhevenko, P. V Zubarev, V. P. Bulychev, N. N. Bragin, V. N. Kruglov, and M. A. Fedotov, "Effect of small amounts of tungsten carbide

on the strength, creep, and brittle-to-ductile transition temperature of zirconium carbide," *Powder Metall. Met. Ceram.*, vol. 22, no. 1, pp. 35–38, 1983.

[84] S. M. Kats and S. S. Ordan'yan, "High temperature creep of ZrC-TaC solid solutions," *Izv. Akad. Nauk SSSR, Neorg. Mater.*, vol. 13, no. 10, pp. 1767–1770, 1977.

[85] S. M. Kats, "Influence of Tungsten Carbide on Creep of Zironium Carbide," *Inorg. Mater.*, vol. 15, no. 10, p. 1400, 1979.

[86] D. W. Lee and J. S. Haggerty, "Plasticity and Creep in Single Crystals of Zirconium Carbide," *J. Am. Ceram. Soc.*, vol. 52, no. 12, pp. 641–647, 1969.

[87] A. Luo, J. J. Park, D. L. Jacobson, B. H. Tsao, and M. L. Ramalingam, "Creep behavior of molybdenum and a molybdenum-hafnium carbide alloy from 1600 to 2100 K," *Mater. Sci. Eng. A*, vol. 177, pp. 89–94, Jan. 1994.

[88] Y. V Miloserdin, K. V Naboichenko, L. I. Laveikin, and A. G. Bortsov, "The high-temperature creep of zirconium carbide," *Strength Mater.*, vol. 4, no. 3, pp. 302–305, 1972.

[89] I. I. Spivak, R. A. Andrievskii, and V. V Klimenko, "Creep of two-phase titanium carbide alloys," *Sov. Powder Metall. Met. Ceram.*, vol. 13, no. 3, pp. 244–247, 1974.

[90] I. I. Spivak, R. A. Andrievskii, V. N. Rystsov, and V. V Klimenko, "Creep of titanium monocarbide in its homogeneity range," *Sov. Powder Metall. Met. Ceram.*, vol. 13, no. 7, pp. 574–578, 1974.

[91] T. Suzuki, N. Nomura, K. Yoshimi, and S. Hanada, "Microstructure and creep of Mo-ZrC in-situ composite," *Mater. Trans. JIM(Japan)*, vol. 41, no. 9, pp. 1164–1167, 2000.

[92] P. V Zubarev and L. N. Dement'ev, "Relation between the activation energies of high-temperature creep and diffusion in transition metal carbides," *Strength Mater.*, vol. 3, no. 9, pp. 1058–1061, 1971.

[93] P. V Zubarev and L. N. Dementev, "Effect of the Form of Loading on the High-Temperature Creep of ZrC," *Probl. Prochnosti*, no. 8, pp. 61–64, 1973.

[94] P. V Zubarev and L. N. Dementev, "Basic Laws Governing the High-Temperature Creep of ZrC and NbC," in *Dokl. Akad. Nauk SSSR*, 1977, vol. 232, no. 6, pp. 1373–1375.

[95]   P. V Zubarev and A. B. Kuraev, "Stress Relaxation in Zirconium Carbide. II. Mechanisms of Stress Relaxation Relationship Between the Processes of Creep and Relaxation," *Probl.Prochn.*, no. 2, pp. 55–60, 1994.

[96]   W. F. Smith and J. Hashemi, *Foundations of Materials Science and Engineering*. New York: Mcgraw-Hill Companies, Inc., 2004.

[97]   H. Li, L. Zhang, Q. Zeng, and L. Cheng, "Thermodynamic Calculation of HfB2 Volatility Diagram," *J. Phase Equilibria Diffus.*, vol. 32, no. 5, pp. 422–427, Jul. 2011.

[98]   T. A. Parthasarathy, R. A. Rapp, M. Opeka, M. K. Cinibulk, and N. Jacobson, "Modeling Oxidation Kinetics of SiC-Containing Refractory Diborides," *Journal of the American Ceramic Society*, vol. 95, no. 1. p. 338, Jan-2012.

[99]   C. Tian, D. Gao, Y. Zhang, C. Xu, Y. Song, and X. Shi, "Oxidation behaviour of zirconium diboride-silicon carbide ceramic composites under low oxygen partial pressure," *Corros. Sci.*, vol. 53, no. 11, pp. 3742–3746, 2011.

[100] Q. N. Nguyen, E. J. Opila, and R. C. Robinson, "Oxidation of Ultrahigh Temperature Ceramics in Water Vapor," *Journal of The Electrochemical Society*, vol. 151, no. 10. pp. B558–B562, 2004.

[101] S. R. Levine, E. J. Opila, R. C. Robinson, and J. A. Lorincz, "Characterization of an Ultra-High Temperature Ceramic Composite." Jan-2004.

[102] D. S. Wilkinson, "Creep mechanisms in multiphase ceramic materials," *Journal of the American Ceramic Society*, vol. 81, no. 2. pp. 275–299, Jan-1998.

[103] C. M. Carney, T. A. Parthasarathy, and M. K. Cinibulk, "Oxidation Resistance of Hafnium Diboride Ceramics with Additions of Silicon Carbide and Tungsten Boride or Tungsten Carbide," *Journal of the American Ceramic Society*, vol. 94, no. 8. p. 2600, Jan-2011.

[104] D. Sciti, V. Medri, and L. Silvestroni, "Oxidation behaviour of HfB2-15 vol.% TaSi2 at low, intermediate and high temperatures," *Scr. Mater.*, vol. 63, no. 6, pp. 601–604, 2010.

[105] A. Di Masol, R. Savino, M. S. Fumo, L. Silvestroni, and D. Sciti, "Arc-Jet Testing on HfB2-TaSi2 Models: Effect of the Geometry on the Aerothermal Behaviour," *Open Aerospace Engineering Journal*. Jan-2010.

[106] D. Sciti, G. Bonnefont, G. Fantozzi, and L. Silvestroni, "Spark plasma sintering of HfB2 with low additions of silicides of molybdenum and tantalum," *Journal of the European Ceramic Society*, vol. 30, no. 15. pp. 3253–3258, Jan-2010.

[107] D. Sciti, F. Monteverde, S. Guicciardi, G. Pezzotti, and A. Bellosi, "Microstructure and mechanical properties of ZrB2-MoSi2 ceramic composites produced by different sintering techniques," *Mater. Sci. Eng. A*, vol. 434, no. 1, pp. 303–309, 2006.

[108] F. Peng and R. F. Speyer, "Oxidation Resistance of Fully Dense ZrB2 with SiC, TaB2, and TaSi2 Additives," *J. Am. Ceram. Soc.*, vol. 91, no. 5, pp. 1489–1494, 2008.

[109] P. Hu, K. Gui, Y. Yang, S. Dong, and X. Zhang, "Effect of SiC Content on the Ablation and Oxidation Behavior of ZrB-Based Ultra High Temperature Ceramic Composites," *Materials*, vol. 6, no. 6. pp. 1730–1744, Jan-2013.

[110] S. C. Zhang, G. E. Hilmas, and W. G. Fahrenholtz, "Oxidation of zirconium diboride with tungsten carbide additions," *J. Am. Ceram. Soc.*, vol. 94, no. 4, pp. 1198–1205, 2011.

[111] L. Weng, X. Zhang, J. Han, and W. Han, "The effect of Si3N4 on microstructure, mechanical properties and oxidation resistance of HfB2-based composite," *Journal of Composite Materials*, vol. 43, no. 2. pp. 113–123, Jan-2009.

[112] W. G. Fahrenholtz, G. E. Hilmas, S. C. Zhang, and S. Zhu, "Pressureless Sintering of Zirconium Diboride: Particle Size and Additive Effects," *J. Am. Ceram. Soc.*, vol. 91, no. 5, pp. 1398–1404, 2008.

[113] B. F. Dyson, R. D. Lohr, and R. Morrell, *Mechanical Testing of Engineering Ceramics at High Temperatures*. Essex, England: Elsevier Science Publishers, Ltd., 1989.

[114] W.-P. Tai, T. Watanabe, and N. S. Jacobson, "High-Temperature Stability of Alumina in Argon and Argon/Water-Vapor Environments," *J. Am. Ceram. Soc.*, vol. 82, no. 1, pp. 245–248, Dec. 2004.

[115] C. B. Bargeron, R. C. Benson, R. W. Newman, A. N. Jette, and T. E. Phillips, "Oxidation mechanisms of hafnium carbide and hafnium diboride in the temperature range 1400 to 2100C," *Johns Hopkins APL Technical Digest (Applied Physics Laboratory)*, vol. 14, no. 1. pp. 29–36, Jan-1993.

[116] K. Shugart and E. Opila, "SiC Depletion in ZrB2-30 vol% SiC at Ultrahigh Temperatures," *J. Am. Ceram. Soc.*, vol. 98, no. 5, pp. 1673–1683, May 2015.

[117] D. M. Grannan, J. C. Garland, and D. B. Tanner, "Critical Behavior of the Dielectric Constant of a Random Composite near the Percolation Threshold," *Phys. Rev. Lett.*, vol. 46, no. 5, pp. 375–378, Feb. 1981.

[118] C. Armani, "Creep performance of oxide ceramic fiber materials at elevated temperature in air and in steam," 2011.

[119] F. L. King, J. Teng, and R. E. Steiner, "Special feature: Tutorial. Glow discharge mass spectrometry: Trace element determinations in solid samples," *J. Mass Spectrom.*, vol. 30, no. 8, pp. 1061–1075, Aug. 1995.

[120] K. Sevener, "Oxidation of HfB2-SiC Ultra-high Temperature Ceramics at 1500°C and 1600°C," Wright-Patterson AFB, Ohio, 2006.

[121] K. Shugart, B. Patterson, D. Lichtman, S. Liu, and E. Opila, "Mechanisms for Variability of ZrB2-30 vol% SiC Oxidation Kinetics," *J. Am. Ceram. Soc.*, vol. 97, no. 7, pp. 2279–2285, Jul. 2014.

REPORT DOCUMENTATION PAGE

Form Approved
OMB No. 074-0188

1. REPORT DATE *(DD-MM-YYYY)* 26-12-2015	2. REPORT TYPE Doctoral Dissertation	3. DATES COVERED *(From – To)* March 2014 – December 2015

TITLE AND SUBTITLE Creep and Oxidation of Hafnium Diboride-Based Ultra High Temperature Ceramics at 1500°C	5a. CONTRACT NUMBER
	5b. GRANT NUMBER
	5c. PROGRAM ELEMENT NUMBER
6. AUTHOR(S) DeGregoria, Anthony J., Lt Col, USAF	5d. PROJECT NUMBER
	5e. TASK NUMBER
	5f. WORK UNIT NUMBER

7. PERFORMING ORGANIZATION NAMES(S) AND ADDRESS(S) Air Force Institute of Technology Graduate School of Engineering and Management (AFIT/ENY) 2950 Hobson Way, Building 640 WPAFB OH 45433-8865	8. PERFORMING ORGANIZATION REPORT NUMBER AFIT-ENY-DS-15-D-040
9. SPONSORING/MONITORING AGENCY NAME(S) AND ADDRESS(ES) Air Force Office of Scientific Research Dr. Ali Sayir, Program Director 875 N. Randolph St, Ste 325, Rm 3112 Arlington, VA 22203-1768 ali.sayir@afosr.af.mil	10. SPONSOR/MONITOR'S ACRONYM(S) AFOSR
	11. SPONSOR/MONITOR'S REPORT NUMBER(S)

12. DISTRIBUTION/AVAILABILITY STATEMENT
DISTRUBTION STATEMENT A. APPROVED FOR PUBLIC RELEASE; DISTRIBUTION UNLIMITED.

13. SUPPLEMENTARY NOTES
This material is declared a work of the U.S. Government and is not subject to copyright protection in the United States.

14. ABSTRACT
Ultra high temperature ceramics (UHTCs) are leading candidates for aerospace structural applications in high temperature environments, including the leading edges of hypersonic aircraft and thermal protection systems for atmospheric re-entry vehicles. Creep, or the progressive, time-dependent deformation of material under constant load, is a critical criterion in these applications, but not much is known with regard to UHTCs or whether there are interactions with oxidation processes. Thus, a facility for high temperature, mechanical testing in air was augmented for testing in argon. Then, the compressive creep of a popular UHTC, HfB_2, was examined at 1500°C in argon and compared to results in air. HfB_2 specimens with 0, 10, 20, and 30% additions of SiC were tested, which enabled assessments of the effects of grain size and SiC content on creep behavior. Boundary mechanisms accommodated by diffusion through grains dominated the creep rates. The results also suggest that SiC formed a network of point-to-point contacts and increased creep resistance. A unique stressed oxidation test was devised in order to further investigate the interaction of creep and oxidation. The results indicate that up to 75 MPa of compressive stress, models of creep and oxidation in HfB_2-based UHTCs can be decoupled.

15. SUBJECT TERMS
Creep, Oxidation, HfB2, SiC, UHTC

16. SECURITY CLASSIFICATION OF:			17. LIMITATION OF ABSTRACT	18. NUMBER OF PAGES	19a. NAME OF RESPONSIBLE PERSON Dr. Marina B. Ruggles-Wrenn, AFIT/ENY
a. REPORT	b. ABSTRACT	c. THIS PAGE	UU	208	19b. TELEPHONE NUMBER *(Include area code)* (937) 255-3636, ext 4641 marina.ruggles-wrenn@afit.edu
U	U	U			

Standard Form 298 (Rev. 8-98)
Prescribed by ANSI Std. Z39-18

198